Analog epigenetic cell memory by graded DNA methylation

Sebastian Palacios[1,2,3†], Simone Bruno[1,4†], Ron Weiss[2,5], Elia Salibi[1], Andrew Kane[2], Katherine Ilia[2,3], and Domitilla Del Vecchio[1,2*]

[1] Department of Mechanical Engineering, Massachusetts Institute of Technology, Cambridge, MA, 02139, USA.

[2] Department of Biological Engineering, Massachusetts Institute of Technology, Cambridge, MA, 02139, USA.

[3] Institute for Medical Engineering and Science, Massachusetts Institute of Technology, Cambridge, MA, 02139, USA.

[4] Department of Data Science, Dana-Farber Cancer Institute, Boston, MA, 02115, USA.

[5] Department of Electrical Engineering and Computer Science, Massachusetts Institute of Technology, Cambridge, MA, 02139, USA.

[†] These authors contributed equally to this work

[*] Corresponding author: ddv@mit.edu

Summary. Long-term maintenance of gene expression states is required to conserve phenotypic differences among cell types and is often compromised in disease and aging. DNA methylation and histone modifications are believed to mediate this maintenance by enabling cells to keep memory of binary states where a gene is either silenced or active. Here, we used a chromosomally integrated reporter system and mathematical modeling to investigate whether these modifications can confer memory to any gene expression state, and thus equip cells with analog memory. We found that cells maintain any gene expression level by grades of DNA methylation that remain stable over time. According to our nucleosome modification model, this is possible only when H3K9me3 does not mediate the catalysis of DNA methylation. The observation that long-term memory is possible for any gene expression level deepens our understanding of epigenetic cell memory and broadens our view of what constitutes a cell type.

Introduction

Epigenetic cell memory allows the cells of multi-cellular organisms to maintain different phenotypes despite a common genetic code. These phenotypes are encoded in distinct gene expression patterns, which are maintained long-term by the concerted action of gene regulatory networks [1] and epigenetic modifications to DNA and histones [2–4]. In particular, DNA methylation and covalent modifications to histones have appeared

as key mediators of the long-term maintenance of gene expression states [5, 6]. Modifications such as histone 3 lysine tail (H3K9 and H3K4) and DNA (CpG) methylation control the extent to which DNA is compacted and accessible to transcriptional machinery [7, 8]. Specifically, H3K9 tri-methylation (H3K9me3) and DNA methylation are associated with a highly compact chromatin structure characterized by a lack of transcription [9, 10], while H3K4 thri-methylation (H3K4me3) at promoters is associated with actively transcribed genes [11]. Histone modifications H3K9me3 and H3K4me3 can propagate to nearby unmodified histones because they each recruit writers of the same modification [12, 13], and they also inhibit each other by recruiting each other's erasers [14]. This leads to a positive feedback mechanism that mediates the maintenance of each modification and can theoretically result in bistable gene expression where only active and silenced gene states are stably kept through cell division [15], as observed for example in the mating-type switching of *S. pombe* [16, 17].

DNA methylation has been regarded as the embodiment of inheritance since it can propagate through subsequent cell divisions by the action of maintenance enzymes that copy the methylation pattern of the parental DNA strand on the newly synthesized DNA strand upon DNA replication [7]. In recent years, however, DNA methylation is emerging as a more dynamic process than originally thought [18–20]. Evidence suggests that DNA methylation might be in a dynamic equilibrium under the continnuous and competitive action of writer and eraser enzymes, such as DNA methyltransferases (DNMTs) and ten-eleven translocation (TET) cytosine dioxygenases [21], while operating in orchestration with histone modifications, adding another layer of complexity [22]. Specifically, DNA methylation dynamically interacts with H3K4me3 through mutual inhibition [23, 24], and with H3K9me3 through mutual catalysis [25, 26]. When this cross-catalysis is sufficiently strong, it is theoretically possible that only fully methylated or completely unmethylated patterns are propagated stably through cell division, leading to long-term maintenance of silenced and active gene states exclusively [27]. This possibility is consistent with recent genome-wide studies indicating that DNA methylation pattern is not faithfully maintained, and that fully methylated and completely unmethylated sites have higher maintenance fidelity than intermediately methylated sites [28]. Moreover, early experiments already hinted at an all-or-none distribution of DNA methylation across the genome [29], and that although intermediate levels of DNA methylation are possible, they have lower frequency [30, 31].

Gene silencing and reactivation dynamics have been investigated following sequence-specific recruitment of chromatin regulators to DNA operators in chromosomally integrated semi-synthetic reporter systems [32–35] and at endogenous gene loci [36, 37]. In particular, single cell time-resolved analysis revealed that gene silencing and reactivation occurred in an all-or-none manner, wherein transient recruitment of a chromatin regulator to a gene modulated the fraction of cells that become permanently silenced rather than modulating the level of gene expression [32]. Independent studies performed on endogenous gene loci in plants had also found that memory occurred in "on" or "off" gene states, with the fraction of silenced cells dependent on the duration of stimulation

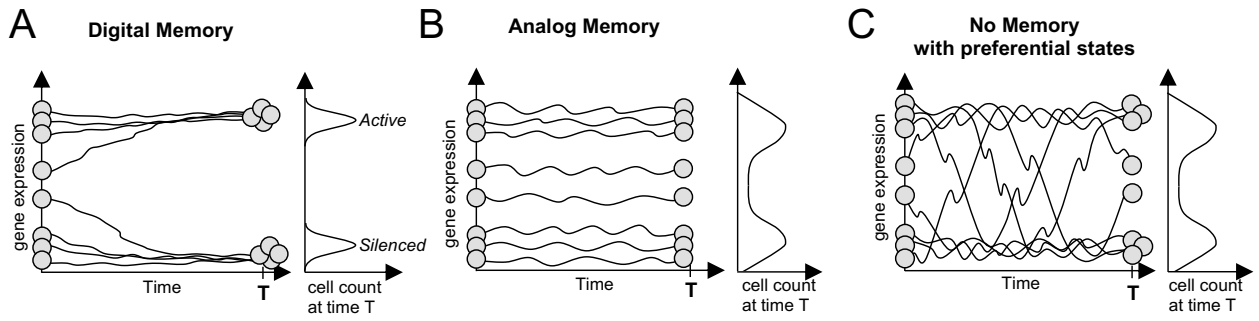

Fig. 1. Digital versus analog memory of gene expression. A Memory is digital when the cell can maintain in time either silenced or fully active gene expression states, but no other states. **B** Memory is analog when the cell can maintain any initial gene expression level. **C** Lack of memory with preferential states result in long-term gene expression trajectories that are independent of the initial state. However, preferential states are visited more often. The stationary distribution of gene expression across the cell population depicts the long-term behavior (here shown at time T) of the number of cells (x-axis) that express the gene at a given level (y-axis).

[38]. Experiments on knock-in reporters in *S. cerevisiae* at HML/HMR loci recapitulated this observation by showing that the dosage of the chromatin regulator controls the fraction of silenced cells but not gene expression level [39]. Taken together, these findings, along with previous evidence, support the hypothesis that epigenetic cell memory may be digital, that is, an exclusive attribute of active and silenced gene states. Only recently, continuous and graded variations of gene expression levels were identified across gradient-like distributions of cell types [40]. These cell types are also associated with spatial gradients of DNA methylation [41], suggesting that intermediate levels of DNA methylation could potentially cover a role in the maintenance of grades of gene expression. These data indicate that cells should have mechanisms that allow them to stably maintain continuous gene expression levels beyond the active and silenced states, and that DNA methylation could be a mediator of this analog memory capability.

Models of *digital* epigenetic cell memory posit that only active and silenced gene expression states, wherein a gene is either fully active or turned off, can be stably maintained. This two-state memory model therefore rules out the possibility that any other gene expression level, different from active or silenced, can be maintained (Fig. 1A). By contrast, models of *analog* epigenetic cell memory allow for the stable maintenance of any level of gene expression (Fig. 1B). The stationary distribution of gene expression levels across a population of cells with digital memory has two peaks, one in correspondence to the active state and the other in correspondence to the silenced state, with no cells between them (Fig. 1A, right-side). Therefore, the presence of cells with gene expression at intermediate levels, as observed with analog memory (Fig. 1B, right-side), is incompatible with digital memory. Nevertheless, this feature alone is insufficient to claim analog memory as it is also consistent with a case of no memory with preferential states (Fig. 1C). However, in the latter case but not in the former, cells only transiently express the gene at intermediate levels before reaching their preferred active or silent state.

Thus, time-resolved analysis of cell trajectories with intermediate gene expression levels is required to rule out a case of no memory with preferential states and conclude analog memory.

Here, we investigate whether analog memory is possible and how that may be mediated by DNA methylation and histone modifications. To this end, we utilize a genetic reporter system integrated into an endogenous mammalian locus coupled with targeted recruitment of epigenetic effectors. By time course analysis of the reporter with clonal resolution, we discovered that cells maintain any gene expression level and that this level inversely correlates with the grade of DNA methylation within the promoter and operator sites. In turn, the grade of DNA methylation, as determined by the mean number of CpGs methylated, remains approximately stable over time in the absence of any epigenetic effector input. Yet, we can permanently repress or activate a partially active gene that has an intermediate DNA methylation grade by transiently recruiting to the gene DNA methylation writer or "eraser" enzymes, respectively. These findings place DNA methylation grade as a causal determinant of analog memory of gene expression states. Our nucleosome modification model, which includes the interactions among DNA methylation, H3K4me3, and H3K9me3, recapitulates these results when H3K9me3 does not mediate the catalysis of DNA methylation and the basal establishment and erasure rates of DNA methylation are negligible.

Results

A chromosomal genetic reporter system to study gene expression dynamics following recruitment of epigenetic effectors

We first set out to develop an experimental system to systematically probe the role that histone and DNA methylation play in the establishment and maintenance of gene expression states. To this end, we constructed a genetic reporter in an endogenous mammalian locus (Fig. 2A; Methods; Table SE1) [42]. The genetic reporter comprises the constitutive mammalian elongation factor 1a promoter (EF1a) driving the expression of fluorescent protein EBFP2. We flanked the genetic reporter with cHS4 chromatin insulators [43] for isolation of the reporter from other genes. The reporter comprises five binding sites upstream of the promoter for each of the DNA-binding proteins PhlF and rTetR (Fig. SE.1A, B; Table SE2) [44], where the binding of PhlF and rTetR to DNA can be modulated using 2,4-diacetylphloroglucinol (DAPG) and doxycycline (dox), respectively. Moreover, the region upstream of the promoter comprises five guide RNA (gRNA) target sites, which enable the targeted recruitment of epigenetic effectors fused to dCas9 (Fig. 2A; Fig. SE.1C; Table SE2; Table SE3). The general experimental approach (Fig. 2B) consisted of expressing the epigenetic effectors fused to PhlF, rTetR, or dCas9 (Fig. SE.1A-

F and Table SE2) using transient transfection in cells bearing the genetic reporter. Cells were co-transfected with a fluorescent transfection marker, which enabled the use of fluorescence-activated cell sorting to obtain cell populations with varying levels of effector expression. Time-course flow cytometry measurements and analysis were subsequently performed. The resulting stationary distributions of gene expression from the genetic reporter across the cell populations were analyzed (Fig. 2C).

Cells with intermediate levels of gene expression exist in the DNMT3A-treated stationary cell population

We first investigated the gene expression dynamics following the recruitment of DNA methylation writer DNA methyltransferase 3 alpha (DNMT3A) to the genetic reporter. To this end, we expressed DNMT3A-dCas9 [45](Fig. SE.1 C; Table SE2), a fusion of dCas9 and the catalytic domain of DNMT3A, via transient transfection targeted to five target sites upstream of the promoter in the genetic reporter using a gRNA (Table SE3). Subsequently, we utilized fluorescence-activated cell sorting to obtain cell populations for various transfection levels of DNMT3A-dCas9 and proceeded with time-course flow cytometry measurements. We observed that gene expression was repressed, reaching maximal repression approximately 11 days after transfection (Fig. 2D-E and Fig. SE.2A). After reaching maximal repression, the cell distributions and percentage of cells in silenced, intermediate, and active gene expression states remained stationary for all levels of DNMT3A-dCas9 (Fig. 2D,E and Fig. SE.2A-C). This, along with no detection of the transfection marker of DNMT3A-dCas9 by day 9 (Fig. SE.2B), indicates that cells could remember the DNMT3A transient stimulation. No repression was observed for cells where a gRNA with a scrambled target sequence (gRNA NT) was utilized with DNMT3A-dCas9 or when dCas9 alone was targeted to the genetic reporter (Fig. SE.2D,E).

Remarkably, although the epigenetic effector dosage increased the percent of cells in the silenced state as in previous reports [39], all dosages of DNMT3A-dCas9 led to stationary distributions of fluorescence in which approximately 10% of the cells had intermediate levels of gene expression (Fig. 2D, E and Fig. SE.2C). Experiments where we transiently transfected the same DNMT3A catalytic domain fused to rTetR instead of dCas9 (rTetR-XTEN80-DNMT3A) (Fig. SE.1D; Fig.SE.3A-C; Table SE2) also led to stationary distributions in which up to approximately 16-19% of the cells exhibited intermediate levels of gene expression. These observations are compatible with analog memory and incompatible with digital memory (Fig. 1). Chromatin immunoprecipitation (ChIP) and Methylated DNA immunoprecipitation (MeDIP) followed by qPCR further showed an increase in DNA methylation and H3K9me3 levels, accompanied by a decrease in H3K4me3 level in the reporter compared to the untreated (active) cells (Fig. 2F; Methods; Table SE4). This is in accordance with

reports showing the ability of methylated DNA to recruit writers for H3K9me3 [26] and indicate that these two chromatin modifications play a role in the temporal maintenance of gene expression states.

In order to discriminate the roles of DNA methylation and H3K9me3 in the maintenance of gene expression states, we investigated the gene expression dynamics following recruitment of writers for H3K9me3 to the promoter. To this end, we fused DNA-binding protein PhlF to KRAB (Fig. SE.1E and Table SE2) [46], an epigenetic effector that promotes H3K9 tri-methylation [47, 48]. We thus expressed PhlF-KRAB via transient transfection in the cells bearing the genetic reporter, performed fluorescence-activated cell sorting to obtain cell populations across different transfection levels of PhlF-KRAB, and performed time-course flow cytometry measurements (Fig. 2G,H and Fig. SE.4A). We observed rapid repression of gene expression for cells transfected with PhlF-KRAB, while no repression for cells transfected with PhlF without fusion to KRAB. Irrespective of the dosages of PhlF-KRAB, gene expression reverted to the active gene state within 4 days after reaching maximal repression (Fig. 2G,H). This aligns with previous reports where KRAB-based epigenetic editing resulted in temporary repression while failing to enable long-term silencing [37, 45]. Further experiments with transient expression of PhlF-KRAB also resulted in temporary repression of the genetic reporter while no long-term silencing was observed (Fig. SE.4B-E). To determine what chromatin modifications emerged as a result of KRAB treatment, we performed ChIP and MeDIP followed by qPCR on cells repressed with PhlF-KRAB (Fig. 2I and Methods). We observed that H3K9me3 level, but not DNA methylation level, increased in the genetic reporter compared to the untreated cells (active), while the level of H3K4me3 decreased (Fig. 2I). Therefore, although it is possible for H3K9me3 to mediate the catalysis of DNA methylation [25, 49], the data of Fig. 2I show that this is not the case in our reporter system, consistent with what was found elsewhere [32]. Taken together, these data indicate that an increase in H3K9me3 in the absence of DNA methylation is unable to permanently downregulate gene expression in the cell population. Therefore, DNA methylation but not H3K9me3 emerges as key mediator of the temporal maintenance of gene expression states in cells treated with DNMT3A (Fig. 2D,E).

The above results are recapitulated by a nucleosome modification model that includes H3K9me3 and H3K4me3, their autocatalysis [3, 12, 13, 50] and mutual inhibition [51], DNA methylation, its mutual inhibition with H3K4me3 [4, 52, 53], and the recruitment of H3K9me3 writers by methylated DNA [26] but no recruitment of DNMTs by H3K9me3 (SI Sections S.1, S.2, S.3, and Fig. SM.4). Consistent with the data, this model produces a stationary distribution of fluorescence in the DNMT3A-treated cell population that includes cells with intermediate gene expression levels, which is incompatible with digital memory (Fig. 1A). This model differs from the one originally published in [27] due to the lack of recruitment of DNA methylation writer DNMT3A by H3K9me3. We therefore next investigated with this new model, lacking H3K9me3-mediated recruitment of DNMTs, whether intermediate gene expression states could be temporally maintained, a hallmark of analog memory (Fig. 1B).

The nucleosome modification model predicts analog memory in the absence of H3K9me3-mediated recruitment of DNA methylation writers

First, we performed a systematic parametric analysis of the original nucleosome modification model of [27] (SI Figs. SM.1A,C) to determine conditions under which the model could reproduce the observed DNMT3A-dCas9 dose-dependent stationary distributions of Fig. 2D. We found that in addition to requiring that the basal erasure of histone modifications is sufficiently slower than autocatalysis, needed to reproduce the data of Fig. 2G, the model could recapitulate the data of Fig. 2D (SI Fig. SM.4B,D) under the following additional conditions. First, DNA demethylation rate is negligible on the time scales of our experiments, which is consistent with the reported high efficiency of DNMT1-mediated maintenance of methylated CpGs [54]. Second, H3K9me3 does not mediate DNA methylation establishment, which is supported by the ChIP and MeDIP data of Fig. 2F,I. Third, mutual inhibition between repressive (H3K9me3 and DNA methylation) and activating (H3K4me3) modifications is sufficiently strong (ε' sufficiently large, SI Section S.4). With these assumptions, the original model of [27] simplifies to that illustrated in Fig. 2J, and recapitulates the data of both Fig. 2D and Fig. 2G (SI Fig. SM.4).

We next used this simplified model to investigate the temporal dynamics of fluorescence in cells with intermediate levels of gene expression. In the absence of epigenetic effectors, DNA methylation grade (CpGme), defined by the mean fraction of the number of CpGs methylated in the gene, remains approximately constant in time since DNA demethylation rate is negligible and DNA methylation establishment is absent (no epigenetic effector and no recruitment of it by H3K9me3). Because DNA methylation grade inversely modulates H3K4me3 level (Fig. 2K, top), and H3K4me3 is proportional to gene expression level (SI Section S.2), then also gene expression level should remain approximately constant in time. Stochastic simulations of the system confirmed that cells initially expressing the gene at any intermediate level corresponding to a given DNA methylation grade give rise to a population of cells that keep the intermediate level of gene expression and do not approach the repressed or silenced states (Fig. 2L). That is, the model rules out a case of no memory with preferential states (Fig. 1C) and hence asserts analog memory (Fig. 1B).

Interestingly, despite this graded dosage-dependence between DNA methylation grade and gene expression, the model predicts a bimodal gene expression distribution in the cell population after transient DNMT3A-dCas9 transfection (Fig. 2M), in agreement with the experimental data (Fig. 2D). According to the model, this two-peak distribution is caused by an ultrasensitive response of DNA methylation grade to the DNMT3A-dCas9 transient dosage (Fig. 2K, bottom). Further parameter investigation indicates that this dose response curve becomes graded when the mutual inhibition between activating (H3K4me3) and repressing (H3K9me3 and DNA

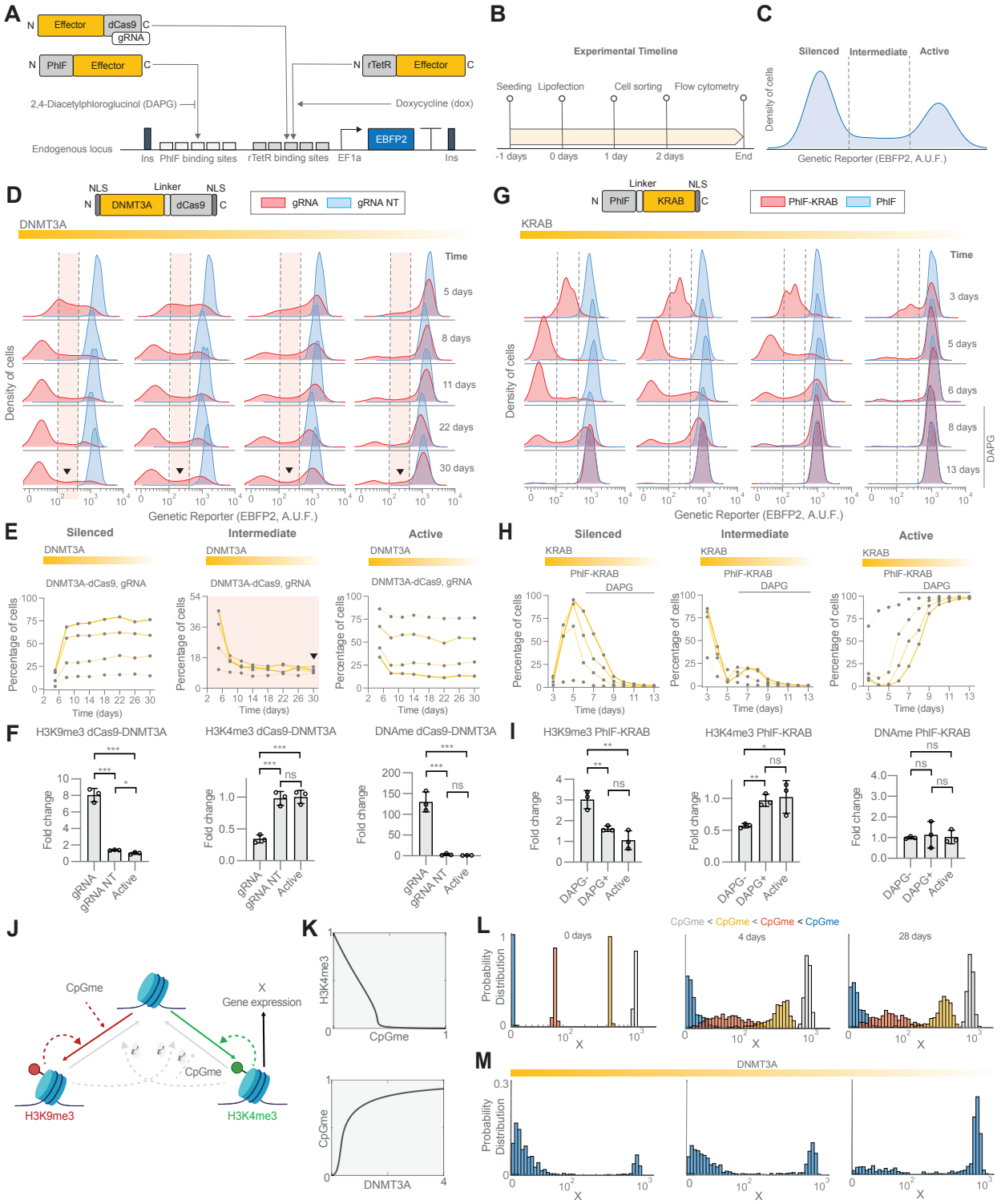

Fig. 2. Continued on the following page.

Fig. 2. Gene expression dynamics after targeted DNMT3A recruitment is consistent with analog cell memory and inconsistent with digital memory. A Schematic of the genetic reporter integrated into a mammalian locus using site-specific chromosomal integration. A mammalian constitutive promoter (EF1a) drives the expression of fluorescent protein EBFP2. Upstream binding sites enable the targeted recruitment of epigenetic effectors, which are fused to DNA-binding proteins rTetR, PhlF or dCas9. The genetic reporter is flanked by chromatin insulators for isolation from other genes. **B** Experimental overview describing transient transfection into cells bearing the genetic reporter, fluorescence-activated cell sorting based on transfection level, and time-course flow cytometry measurements. **C** Description of experimental analysis of flow cytometry measurements performing classification of cells in silenced, intermediate, and active levels of gene expression. **D** Gene expression dynamics after recruitment of DNMT3A-dCas9 to the reporter according to the experimental timeline shown in panel B and classification described on panel C. Shown are distributions from flow cytometry measurements of the genetic reporter (EBFP2) for four different levels of transfection. Dashed lines indicate the regions of silenced, intermediate, and active levels of gene expression. Two different gRNA target sequences were utilized: the first was designed to target 5 target sites upstream of the promoter (gRNA), while the other one comprises a scrambled target sequence (gRNA NT) (Table S3). The region of intermediate levels of gene expression is highlighted. Black arrows denote cells exhibiting intermediate levels of gene expression in stationary distributions 30 days after transfection. Data shown are from a representative replicate from 3 independent replicates. **E** Percentage of cells shown in panel D classified into silenced ($\leq$100 EBFP2 A.U.F.), intermediate (100.1$-$399.9 EBFP2 A.U.F.), and active ($\geq$400 EBFP2 A.U.F.) gene expression levels. Highlighted region and black arrows correspond to those in panel D. **F** ChIP-qPCR and MeDIP-qPCR analysis 14 days after transfection of the promoter after recruitment of DNMT3A-dCas9 and cell sorting for high levels of transfection. Data shown is from from three independent replicates. Reported are fold changes and their mean using the standard $\Delta\Delta C_t$ method with respect to the active state. Error bars are s.d. of the mean. **G** Gene expression dynamics after recruitment of PhlF-KRAB according to the experimental timeline shown in panel B and classification described on panel C. Shown are distributions from flow cytometry measurements of the genetic reporter (EBFP2) for four different levels of transfection. Dashed lines indicate the regions of silenced, intermediate, and active levels of gene expression. Data shown are from 3 independent replicates. **H** Percentage of cells shown in panel G classified into silenced ($\leq$100 EBFP2 A.U.F.), intermediate (range of 100.1$-$399.9 EBFP2 A.U.F.), and active ($\geq$400 EBFP2 A.U.F.) gene expression levels. **I** ChIP-qPCR and MeDIP-qPCR analysis 6 days after transfection of the promoter after recruitment of PhlF-KRAB and cell sorting for high levels of transfection. Data is from three independent replicates. Shown are fold changes and their mean as determined by the standard $\Delta\Delta C_t$ method with respect to the active state. Error bars are s.d. of the mean.**J** Simplified chromatin modification circuit diagram obtained when KRAB = 0, DNMT3A = 0, TET1 = 0, and H3K9me3 does not mediate the catalysis of *de novo* DNA methylation. See SI Fig.SM.1C. **K** Top plot: dose-response curve for the (CpGme,H3K4me3) pair. Bottom plot: dose-response curve for the (DNMT3A,CpGme) pair. See SI Figs. SM.1D and SM.3. **L** Probability distributions of the system represented by reactions listed in SI Tables SM.1 and SM.3. See SI Figs. SM.1B and SM.2. **M** Probability distributions of the system after t = 28 days, obtained as described in panel I. See SI Fig. SM.1E and SM.3. In panel K and M, the DNMT3A dynamics are modeled as a pulse that exponentially decreases over time. In our model, α' is the normalized rate of DNA methylation establishment through repressive histone modifications, μ' is ratio between the DNA methylation erasure rate and the activating histone modification erasure rate, and ε (ε') is the parameter that scales the ratio between the basal (recruited) erasure rate and the auto-catalysis rate of each modification.

methylation) modifications is weakened (ε' smaller). In turn, a graded dose response curve leads to a unimodal probability distribution (SI Fig. SM.1D, E). Overall, this indicates that a strong mutual inhibition between activating and repressing modifications is a cause of the bimodal distribution of gene expression in response to DNMT3A presentation. Therefore, this provides an explanation for the lower frequency of intermediate gene expression levels experimentally observed in the DNMT3A-dCas9-treated cell population compared to the higher frequency of cells found in the active or repressed states (Fig. 2E).

Intermediate gene expression levels are stably maintained and are associated with an intermediate DNA methylation grade

Following the model predictions, we hypothesized that epigenetic memory could be analog, thereby enabling cells to maintain any gene expression level. To test this hypothesis, we first sought to investigate whether the cells within DNMT3A-treated populations expressing intermediate gene expression levels exhibited long-term stability of gene expression. To this end, we performed fluorescence-activated cell sorting of the DNMT3A-treated cells from low, intermediate, and high gene expression levels (Fig. 3A, Methods). We then performed time-course flow cytometry measurements for 29 days to analyze the long-term gene expression dynamics. The cells with low and high levels of gene expression maintained an approximately stable distribution of gene expression levels after cell sorting, as expected by a digital memory model. Nonetheless, the cells with intermediate levels of expression, after an initial widening of the fluorescence distribution, also kept a stable gene expression distribution across the population for the entire time-course (Fig. 3B-D). This is incompatible with digital memory (Fig. 1A). This also rules out a case of no memory with preferential states (Fig. 1C) since it demonstrates that cells with intermediate gene expression levels are not *en route* to the silenced or active states, but rather are in a stable epigenetic configuration. To characterize the epigenetic state of these cells, we performed ChIP followed by qPCR of the low, intermediate, and active cell populations (Fig. 3E, Methods). We found an increase of H3K9me3 in the low population when compared to the intermediate and active cell populations. Accordingly, we observed a decrease of H3K4me3 in the low and intermediate expressing cells when compared to the active cells. These results are consistent with the known role of H3K9me3 as a chromatin modification associated with repression and H3K4me3 as a chromatin modification associated with active transcription at promoters [55].

Because we pinpointed DNA methylation as the critical mediator of the maintenance of gene expression states, we performed targeted bisulfite sequencing of the genetic reporter system for each of the three cell populations: low, intermediate, and active (Fig. 3F, Methods). While the active state is essentially devoid of methylated CpGs, the probability of finding any given CpG methylated in the promoter and rTetR binding sites in the intermediate state is distinctly smaller than in the low state and higher than in the active state. From these data, we computed the probability distributions of the fraction of methylated CpGs in the promoter and rTetR binding sites, for each of the low, intermediate, and active states (Fig. 3G, Methods - Section “Quantification and statistical analysis”). These distributions reinforce that the intermediately expressing cells have intermediate levels of DNA methylation. In particular, the mean value of the fraction of methylated CpGs, which we define here as the DNA methylation grade, is intermediate in cells with intermediate expression levels compared to that of the low and active cells and has a loglinear negative correlation (p-value <0.05) with the mean gene expression level (Fig. 3H). All

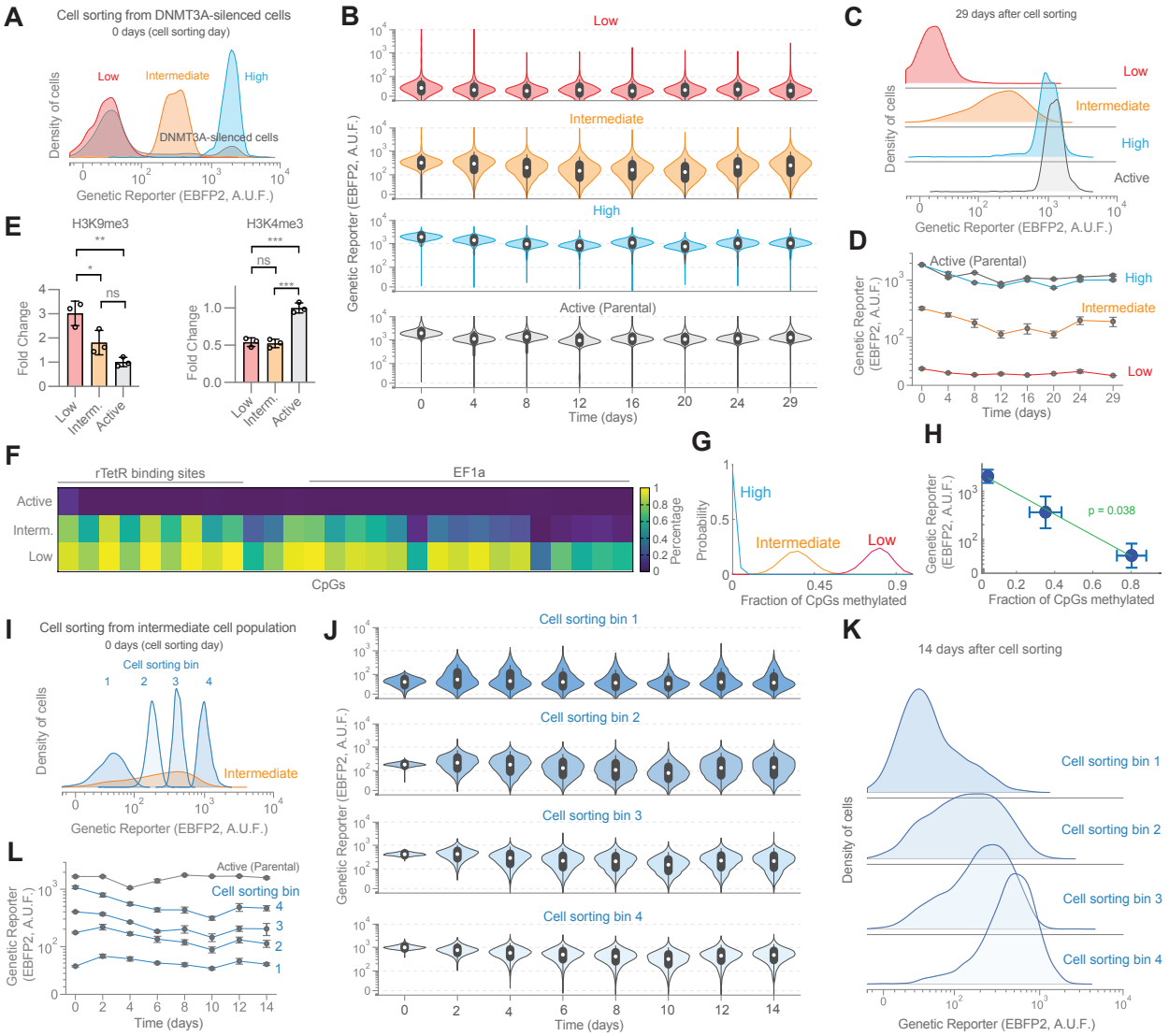

Fig. 3. Continued on the following page.

these findings are recapitulated by our model only when H3K9me3 does not mediate the recruitment of DNA methylation writers (SI Fig. SM.1B and Fig. SM.2).

We tested further the hypothesis that epigenetic memory could be analog by subdividing according to gene expression level a population of cells that had been previously sorted from intermediate gene expression. If epigenetic memory were analog, cells sorted from different gene expression levels should approximately maintain these distinct levels over time. We thus used fluorescence-activated cell sorting to obtain cells from a population with stable intermediate gene expression distribution according to four different bins of gene expression levels (Fig. 3I, Methods). Each of the four resulting cell populations maintained distinct distributions of gene expression levels according to the level on the day of sorting (Fig. 3J-L). We also performed fluorescence-activated cell

Fig. 3. Intermediate levels of gene expression are stably maintained and are associated with an intermediate DNA methylation grade. A Density of cells from flow cytometry measurements on the day of fluorescence-activated cell sorting of cells exhibiting low, intermediate, and high levels of gene expression obtained from a DNMT3A-treated cell population (DNMT3A-dCas9). Data shown are from a representative replicate from three independent replicates. **B** Time-course flow cytometry analysis of the dynamics of gene expression exhibited by cells obtained in panel A. Data are from one representative replicate from three independent replicates. **C** Density of cells from flow cytometry measurements obtained on the last time point in panel B (29 days after cell sorting). Data shown are from one representative replicate from three independent replicates. **D** Dynamics of gene expression exhibited by cells shown in panels A-C. Shown is the mean of geometric mean fluorescence from three independent replicates. Error bars are s.d. of the mean. **E** ChIP-qPCR for H3K9me3 and H3K4me3 of the promoter in the genetic reporter for cells with low and intermediate levels of gene expression as compared to cells in the active state. Shown are fold changes and corresponding mean from three independent replicates as determined by the $\Delta\Delta C_t$ method with respect to the active state. Error bars are s.d. **F** Heatmap of targeted bisulfite sequencing of the genetic reporter. Shown is the mean percentage of methylation for each CpG from three independent replicates. **G** Probability distribution of the fraction of CpGs methylated (See "Methods" section for details on deriving these plots from data in panel E). **H** Correlation plot between the mean fraction of CpGs methylated and mean gene expression level. The green line represents the best-fit line $y = -0.5059x + 0.5497$ obtained by linear regression. The p-value associated with the slope coefficient is p $= 0.038 < 0.05$ (See "Methods" section for details on the linear regression). **I** Density of cells (blue) as measured using flow cytometry on the day of cell sorting from a population of cells that has stably maintained intermediate levels of gene expression (orange). Data is from a representative replicate from three independent replicates. **J** Flow cytometry-based time-course analysis of the dynamics of gene expression exhibited by cells obtained in panel I. Data is from one representative replicate from three independent replicates. **K** Density of cells from flow cytometry measurements obtained on the last time point in panel J (14 days after cell sorting). Data shown are from one representative replicate from three independent replicates. **L** Dynamics of gene expression exhibited by cells shown in panels I-K. Shown is the mean of geometric mean fluorescence from three independent replicates. Error bars are s.d. of the mean.

sorting from cells that had been silenced with DNMT3A fused to rTetR (rTetR-XTEN80-DNMT3A) instead of dCas9 (Fig. SE.5A-D; Methods), and the same results were obtained. These observations support the hypothesis that epigenetic cell memory is analog (Fig. 1B) in agreement with the model (SI Fig. SM.5), and that DNA methylation grade is likely the critical mediator to the stable maintainance of intermediate gene expression levels.

Any gene expression level is stably maintained and inversely correlates with DNA methylation grade

To further test the hypothesis that epigenetic memory operates on an analog basis and that DNA methylation grade mediates the maintenance of gene expression level, we set out to characterize the long-term dynamics of gene expression with extensive sampling of single cells from DNMT3A-treated cell populations followed by monoclonal expansion and analysis. This approach provides a high-resolution evaluation of gene expression trajectories generated exclusively from one initial DNA methylation profile. We therefore performed fluorescence-activated single-cell sorting from the three distinct cell populations that had been previously sorted from a DNMT3A-treated population (Fig. 4A). Specifically, we selected eight different consecutive regions of gene expression levels spanning across the low (2 regions), intermediate (4 regions), and high (2 regions) gene expression levels (Methods). We sampled single cells from each of those regions and performed monoclonal expansion, which resulted in >10 monoclonal populations from each of the eight gene expression regions and

a total of 93 monoclonal populations. Flow cytometry was performed for each of the monoclonal populations 14 days after the initial single-cell sort (Fig. 4B). The monoclonal populations showed a continuum of gene expression levels ranging from background expression level to active gene expression level. (SI Section S.4, Figs. SM.2 and SM.3A). To test whether the gene expression levels from the monoclonal populations could be maintained in time, we selected 8 monoclonal populations (highlighted in Fig. reffig3B), spanning the EBFP2 expression range from the 93 clones, and performed time-course flow cytometry measurements up to 161 days (> 5months) (Fig. 4C) after the initial single-cell sort. In these measurements, we observed that the EBFP2 distributions remained approximately stable over time, validating the initial hypothesis that cells can maintain memory of any gene expression level, which defines analog memory (Fig. 1B).

We next investigated DNA methylation grade as a determinant of the maintenance of gene expression level. To this end, we performed targeted bisulfite sequencing of the genetic reporter in each of the eight populations at two different time points (Fig. 4D,E; Methods). These data indicate that clones (7 and 8) selected from cells in the high gene expression distribution (Fig. 3A) are largely devoid of methylated CpGs. By contrast, clones (1 and 2) selected from cells within the low distribution have the majority of CpGs methylayed. The remaining clones (3,4,5, and 6), selected from the intermediate distribution, display a decreasing number of GpGs that are methylated with high probability as we move from clone 3 to clone 6 (Fig. 4D). These trends inversely correlate with the gene expression levels in the clones (Fig. 4E). To acquire a quantitative understanding of the graded nature of this variation, we computed from the bisulfite sequencing data the probability distribution of the fraction of methylated CpGs in the gene's promoter and rTetR binding sites (See Methods - Section "Quantification and statistical analysis"). This confirmed a progressive and gradual shift of the distributions through the eight clonal populations (Fig. 4F), in accordance with model predictions (Fig. 4G). The correlation between the mean EBFP2 expression level of each clonal population and the mean number of methylated CpGs is loglinear (p $= 5.34 \cdot 10^{-5} < 0.05$, Fig. 4H,I), confirming a gradual increase of the DNA methylation grade through the clonal populations from high to low gene expression levels. Furthermore, the distribution of the fraction of methylated CpGs remained approximately unchanged between the two time points where bisulfite sequencing was performed (Fig. 4F, G. Compare solid and dashed lines), indicating that the DNA methylation grade is stably maintained.

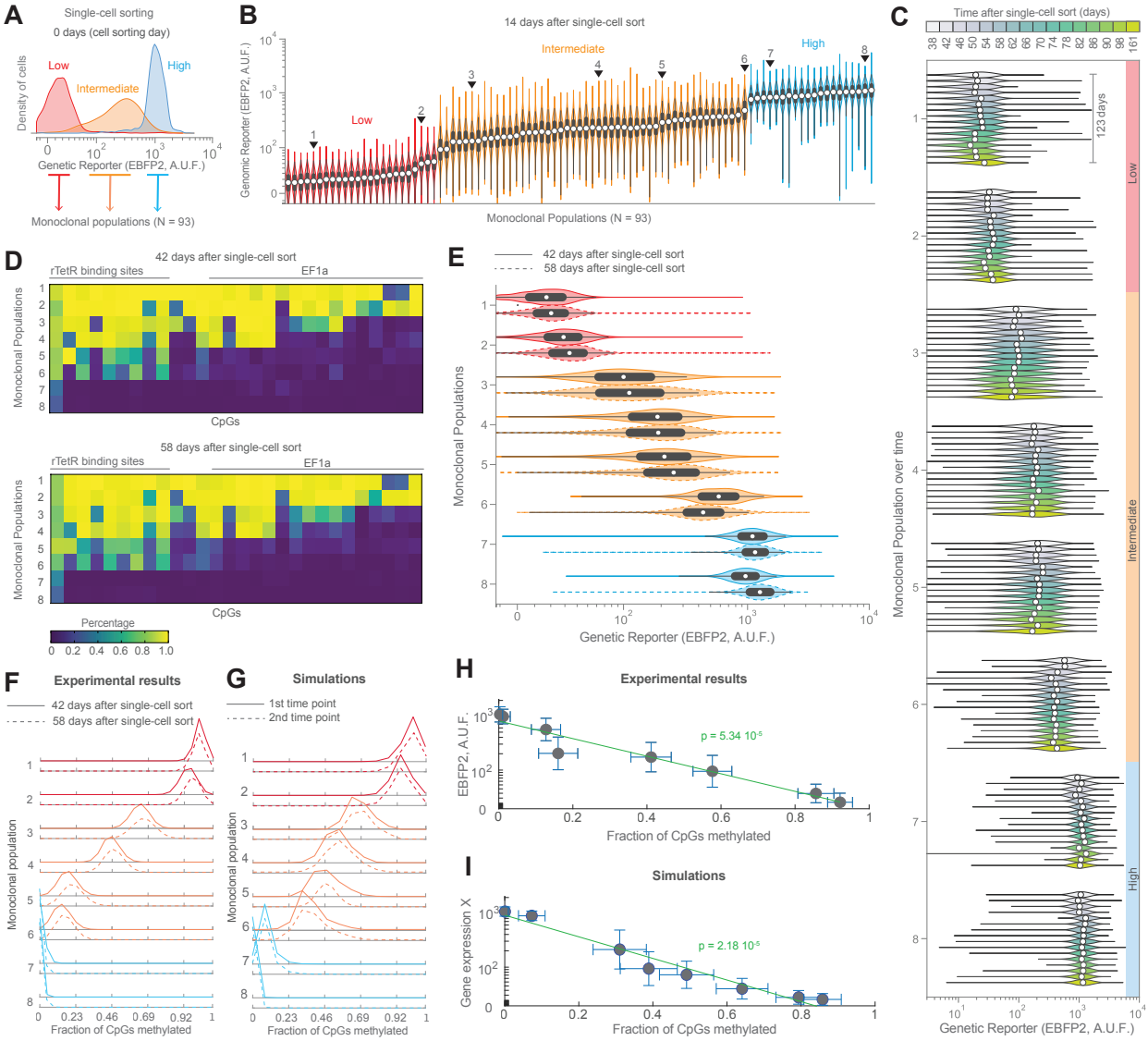

Fig. 4. Continued on the following page.

Fig. 4. Cell memory is analog and stable DNA methylation grades inversely correlate with gene expression level. A Density of cell populations from where monoclonal populations were obtained. The cell populations had stably maintained low, intermediate, and high levels of gene expression. Single cells were obtained from across the three different cell populations. After monoclonal expansion, the total number of monoclonal populations obtained was N = 93. **B** Violin plots of the monoclonal populations (N = 93) measured 14 days after single-cell sorting from the cell populations shown on panel A. Monoclonal populations were positioned on the x-axis according to geometric mean of EBFP2 fluorescence. Clones indicated with numbers 1-8 were selected for further analysis. Colors represent the cell population of origin as shown in panel A. **C** Flow cytometry-based time course analysis of gene expression dynamics of the eight monoclonal populations selected in panel B. **D** Bisulfite sequencing of the genetic reporter in the eight monoclonal population at two different time points. **E** Flow cytometry measurements of the genetic reporter in the eight monoclonal population at two different time points corresponding to those shown on panel D. **F** Probability distribution of the fraction of CpGs methylated (See "Methods" section for details on deriving these plots from data in panel E). The standard deviation for each clone is the following: 0.1752, 0.4707, 0.9492, 1.2714, 1.3101, 1.262, 1.1683, and 0.8095, ordered from clone 1 to clone 8. **G** Simulations of the probability distributions of the system represented by the reactions listed in SI Tables SM.5 and SM.3. The distributions are obtained computationally using SSA [56] and, on the x-axis we have the fraction of CpGs methylated. The standard deviation for each clone is: 0.1346, 0.5472, 1.2585, 1.1189, 1.0431, 1.1117, 0.8512, and 0.8259, ordered from clone 1 to clone 8. The parameter values used for these simulations are listed in SI Section S.9. **H** Correlation plot between the mean fraction of CpGs methylated and mean gene expression level at 42 days after single-cell sort. The green line represents the best linear fit $y = -0.3756x + 0.4358$. The p-value associated with the slope coefficient is p $= 5.34 \cdot 10^{-5} < 0.05$ (See "Methods" section for details on the linear regression). **I** Correlation plot between the mean fraction of CpGs methylated and mean gene expression level, X, obtained via simulations. The green line represents the best linear fit $y = -0.4673x + 0.4580$. The p-value associated with the slope coefficient is p $= 2.18 \cdot 10^{-5} < 0.05$ (See "Methods" section for details on the linear regression).

Further analysis of the clonal distributions of the fraction of methylated CpGs revealed that the variability of the number of methylated CpGs about their mean value, measured by the standard deviation, is larger for intermediate DNA methylation grades when compared to low and high methylation grades (Fig. 4F). The mathematical model recapitulates this property (Fig. 4G) when it includes the two following additional known molecular interactions: (a) H3K9me3 helps recruit DNA methylation maintenance enzyme (DNMT1) to the gene [57] and (b) DNMT1 can cause *de novo* DNA methylation, although at very low rate [58, 59] (see SI Section S.5 for model derivation). With these interactions, the errors made by DNMT1 in maintaining methylation are less probable for a fully methylated gene due to higher recruitment rate of DNMT1 via H3K9me3. Similarly, errors made by DNMT1 in *de novo* methylating additional CpGs are less probable for a gene with no methylation since DNMT1 recruitment is practically absent (see SI Section S.5 and Fig. SM.6 for model analysis.) Overall, these interactions explain the tighter distributions observed for highly and lowly methylated gene states (Fig. 4F).

The genome engineering system that we utilized in this study has been demonstrated to be highly precise [42]. Nevertheless, we still sought to verify that the different clones all had one genome copy of the reporter to rule out the possibility that the variation of gene expression observed across the clones could be due to variability in the genomic integration copy number. To this end, we performed copy number variation analysis using digital PCR (dPCR), which ruled out this possibility (SE.5E and Methods). Taken together, these data establish that the DNA methylation grade is maintained by the clonal populations and that this grade fine-tunes the gene expression level.

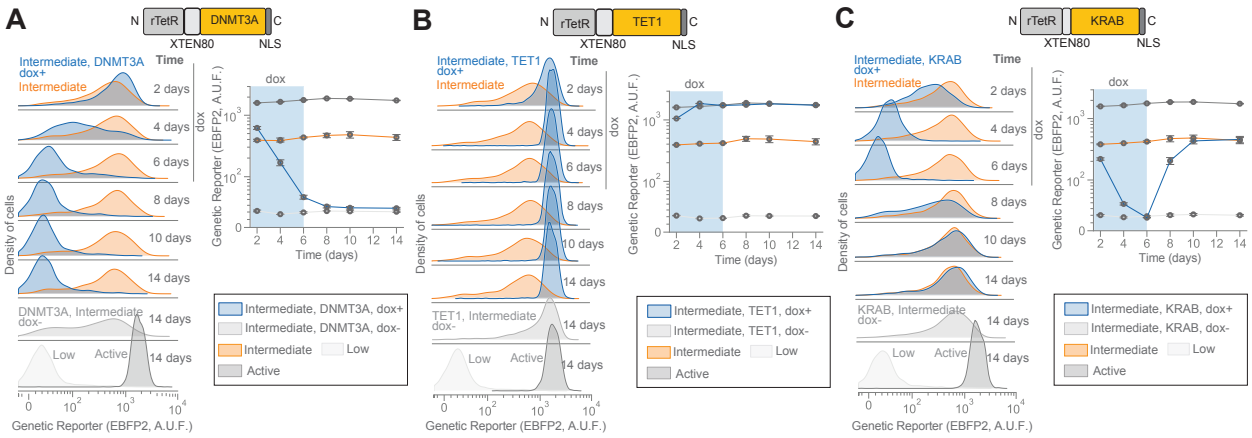

Fig. 5. DNA methylation writers and erasers impair maintenance of intermediate gene expression states. A Time-course of flow cytometry measurements after transient transfection of rTetR-XTEN80-DNMT3A in cells that have been stably maintaining intermediate levels of gene expression. **B** Time-course of flow cytometry measurements following transient transfection of rTetR-XTEN80-TET1 in cells that have been stably maintaining intermediate gene expression levels. **C** Time-course of flow cytometry measurements after transient transfection of rTetR-KRAB in cells that have been stably holding intermediate levels of gene expression. Densities of cells shown are from one representative replicate from three independent replicates. Shown is also the mean of geometric means from three independent replicates. Error bars are s.d. of the mean.

Writers and erasers of DNA methylation impair gene expression level maintenance

Next, we sought to establish a causal link between the DNA methylation grade and the level of gene expression. To this end, we investigated whether altering the DNA methylation grade in cells maintaining an intermediate level of gene expression would impair this maintenance. To enhance DNA methylation, we utilized rTetR-XTEN80-DNMT3A as we have shown before that DNMT3A adds DNA methylation to the genetic reporter (Fig. 2F) consistent with prior reports [45]. To remove DNA methylation, we engineered a fusion protein comprising rTetR fused to the catalytic domains of the ten eleven translocation protein 1 (TET1) [60, 61] to construct rTetR-XTEN80-TET1 (Fig. SE.1F and Table SE2). This catalytic domain has been shown to enable targeted DNA demethylation of mammalian genes [61]. Moreover, we fused rTeR to KRAB to construct rTetR-KRAB (SE.1G and Table SE2) in order to evaluate changes to gene expression when enhancing H3K9me3 without changing DNA methylation (Fig. 2I). We transiently transfected these epigenetic effectors in cells that had been previously sorted for intermediate levels of gene expression from the DNMT3A-treated cells and exhibited intermediate DNA methylation grades. As before, we utilized fluorescence-activated cell sorting to obtain transfected cells and performed time-course flow cytometry measurements (Fig. 5 and Fig. SE.5F-H). By 10 days after transient transfection with rTetR-XTEN80-DNMT3A, the EBFP2 distribution was repressed, remained silenced over time, and overlapped with the distribution of cells that had been previously sorted for low levels of gene expression post DNMT3A-treatment (Fig. 5A). Transient transfection with rTetR-XTEN80-TET1 resulted in nearly complete and permanent reactivation of gene expression (Fig. 5B). By contrast, transient transfection with rTetR-KRAB did not result in any permanent

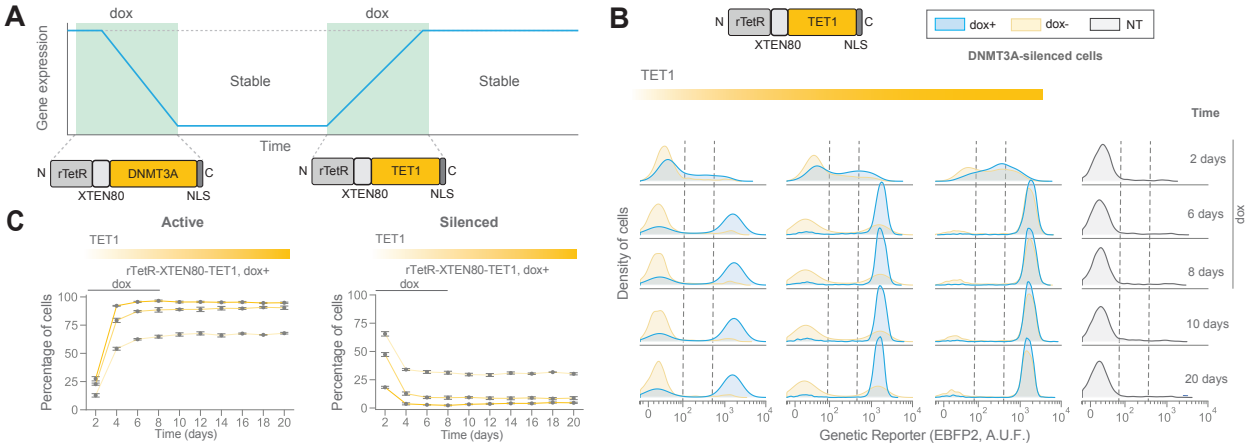

Fig. 6. TET1 permanently reactivates gene expression after complete DNMT3A-mediated silencing. A Experimental overview to study TET1-mediated reactivation of fully DNMT3A-silenced cells. **B** Gene expression dynamics after TET1-mediated reactivation using rTetR-XTEN80-TET1. Shown are distributions from flow cytometry measurements of the genetic reporter (EBFP2) for three different levels of transfection obtained using fluorescence-activated cell sorting. Dashed lines indicate the regions of silenced and active levels of gene expression. Data is from a representative replicate from 3 independent replicates. **C** Percentage of cells shown in panel B classified into silenced ($\leq$100 EBFP2 A.U.F.) and active ($\geq$500 EBFP2 A.U.F.) gene expression levels. Shown is the mean percentage from three independent replicates. Error bars are the s.d. of the mean. NT is untransfected negative control.

change of gene expression. Specifically, 6 days after transfection, we observed levels of repression comparable to those of the low levels in DNMT3A-treated cells, but then expression reverted to the initial intermediate level and remained stable afterwards (Fig. 5C). These data indicate that transient recruitment of a DNA methylation writer or eraser to an intermediadely methylated, and partially active gene, can permanently silence or reactivate the gene. By contrast, transient recruitment of an H3K9me3 writer does not exert a permanent change in gene expression (Fig. 2I). Taken together, these data show that DNA methylation grade is the causal determinant of the maintenance of gene expression levels in accordance with the model predictions (Fig. SM.7).

The ability to fully reactivate gene expression by transiently transfecting rTetR-XTEN80-TET1 in cells that were sorted for intermediate gene expression from DNMT3A-treated cells (Fig. 5B) prompted us to investigate whether we could reactivate cells that had been fully silenced by DNMT3A (Fig. 6A). To this end, we transiently transfected rTetR-XTEN80-TET1 in fully DNMT3A-repressed cell populations, sorted these cells for three levels of rTetR-XTEN80-TET1 transfection, and performed a flow cytometry-based time course analysis to assess reactivation dynamics (Fig. 6A-C and Fig. SE.6A-B). Maximal reactivation was observed by 6 days post-transfection, after which the fluorescence distribution remained unchanged even when dox was removed (Fig. 6B). For the highest level of transfection, in particular, reactivation was nearly complete and permanent (Fig. 6C and Fig. SE.6B). No reactivation occurred when rTetR was targeted to the same sites without TET1 (Fig. SE.6C-F). These data indicate that rTetR-XTEN10-TET1 can permanently restore the active gene expression state in DNMT3A-silenced cells, and can thereby be used as a general tool to permanently reactivate silenced genes in mammalian cells.

Discussion

The extent to which epigenetic cell memory is an exclusive attribute of silenced and active gene states or whether it is possible for any gene expression level is the question addressed by this paper. Unexpectedly, we found that cells can stably maintain any gene expression level (Fig. 3B and I and Fig. 4C) and that this level inversely correlates with grades of DNA methylation in the gene's promoter and upstream operator sites (Fig. 3E-G and Fig. 4E,I,M). Each DNA methylation grade, in turn, measured by the mean number of methylated CpGs, also persists in time (Fig. 4F). Transient recruitment of DNA methylation writer or eraser enzymes to a gene that maintains an intermediate methylation grade and expression level impairs expression level maintenance (Fig. 5). Taken together, these results indicate that analog epigenetic memory of gene expression is possible and that the persistence of DNA methylation grade enables it. Our nucloesome modification model, which includes DNA methylation and its interactions with histone modifications H3K9me3 and H3K4me3, recapitulates analog epigenetic cell memory under the critical conditions: (i) DNMT1-enabled DNA methylation maintenance error rate is very low, necessary for an approximately stable DNA methylation grade across cell divisions, and (ii) H3K9me3 does not mediate the catalysis of *de novo* DNA methylation (see SI Section S.3). Notably, failure of (ii), that is, a strong catalysis of DNA methylation mediated by H3K9me3, even when (i) holds, leads to digital memory (Figs. SM.1B and SM.2). Therefore, a model emerges that can explain the molecular interactions responsible for digital versus analog epigenetic cell memory (Fig. 7).

Although DNA methylation patterns can, in principle, propagate through cell division by the copy-paste action of DNA methylation maintenance enzyme DNMT1 [7], the extent to which DNA methylation patterns are actually maintained in cells has been recently questioned [19]. DNA methylation is a more dynamic epigenetic mark than originally thought, due to the continuous write-erase actions of DNMT3A and TET1 [21], and to interactions with histone modifications [22].These not only include mutual catalysis with H3K9me3 [25, 26] and inhibition with H3K4me3 [23, 24], but also the influence of these histone modifications on the maintenance activity mediated by DNMT1 [57]. These reciprocal actions, taken together, influence the fidelity at which DNA methylation can be inherited through cell division. In fact, the positive feedback loop where DNA methylation mediates the catalysis of H3K9me3 and this, in turn, mediates catalysis of *de novo* DNA methylation, can push an initially partially methylated gene to be fully methylated. The competitive interaction of DNA methylation with H3K4me3, in turn, can cause H3K4me3 to win over an initially low DNA methylation state and to revert this to unmethylated. When these interactions are sufficiently strong, then digital memory emerges (SI Section S.3, Fig. SM.2), and fully methylated and completely unmethylated states can achieve higher maintenance fidelity when compared to sites

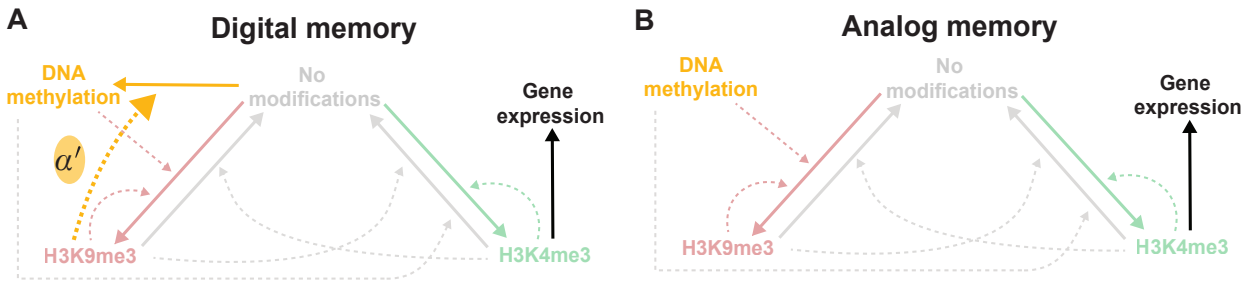

Fig. 7. The interactions between DNA methylation and histone modifications explain the difference between digital and analog epigenetic cell memory. A Digital memory. H3K9me3 recruits writer enzymes for DNA methylation (yellow dashed arrow). **B** Analog memory. H3K9me3 does not recruit writer enzymes for DNA methylation. In the diagrams, we have assumed that no external epigenetic effectors (such as KRAB, DNMT3A, and TET1) are present. The rate of DNA methylation catalysis mediated by H3K9me3 is represented by α'. Refer to Fig. SM.1A, C for the complete diagram and model.

where not all the CpGs are methylated [28]. The above cited facts raise doubt as to whether intermediate DNA methylation states can be propagated and maintained.

Notwithstanding, our MeDIP and ChIP data have shown that H3K9me3 does not catalyze DNA methylation in our system (Fig. 3E), which is also consistent with previous reports [32]. With this, our nucleosome modification model predicts that any intermediate DNA methylation grade can be stably maintained (SI Fig.SM.1), which is confirmed by our bisulfite sequencing data (Fig. 4F). These data further show that the variability of the number of methylated GpGs about its mean level is larger for intermediate DNA methylation grades (Fig. 4F). The nucleosome modification model would not be able to recapitulate this if we had regarded the DNA methylation process as isolated from H3K9me3 and H3K4me3 (SI Section S.5 and Fig. SM.6). Specifically, the model recapitulates this feature when it includes the known facts that DNMT1 is recruited by H3K9me3 [57] and that DNMT1 can make mistakes, although at a very low rate [58, 59] (Fig. 4G and SI Section S.5, Fig. SM.6).

While it is well established that DNA methylation has a repressive effect on gene expression [36], how the ratio of methylated to unmethylated CpGs is a modulator of gene expression level has not been thoroughly investigated. Prior studies, by pairing bisulfite sequencing with RNA quantification, found that gene expression level inversely correlates with DNA methylation at the promoter of a gene [62, 63]. Here, we have shown that the DNA methylation grade in the promoter and its immediate upstream operator sites inversely correlates with gene expression level via an approximately loglinear relationship (Fig. 4M). Further, we have demonstrated that recruitment of DNA methylation eraser or writer enzymes to an intermediately methylated, and partially active, gene fully activates or silences expression (Fig. 5). This indicates that DNA methylation grade is a causal modulator of gene expression level.

In this study, we have measured only protein but not mRNA level, so, in principle, it remains to be determined

whether the inverse loglinear correlation that we have found (Fig. 3G and Fig. 4H) also exists between mRNA level and DNA methylation grade. According to our stochastic model, which includes mRNA dynamics, mRNA and protein levels correlate because the fluorescent protein is stable and it is not post-transcriptionally regulated by other processes (SI Section S.2). However, during complex biological processes such as differentiation or reprogramming, these assumptions may not always hold true leading to uncorrelated expression levels of a particular mRNA and its cognate protein [64]. Hence, the extent of the correlation between DNA methylation grade and gene expression would need to be revisited and will likely depend on the context.

Although we have demonstrated analog cellular memory in CHO-K1 cells, the range of levels of stable gene expression that we report here (Fig. 4C) are reminiscent of the gene expression gradients that have been observed in the cell types of the hippocampus [40]. These cells also display a DNA methylation landscape that varies continuously along spatial gradients [41], suggesting that the molecular underpinnings of analog memory that we have unveiled apply to a variety of mammalian cell types and tissues. More research will be required to determine the extent to which these gradients of gene expression correlate with the DNA methylation grade at the gene's promoter and are temporally maintained at the single cell or clonal level. Single-cell nucleosome, methylome, and transcriptome sequencing (scNMT-seq) [65] can be applied to determine the correlation between the DNA methylation grade and the expression level of a gene, as employed to map developmental processes with single-cell resolution [66]. However, acquiring temporal dynamic data of specific genes in single cells (or in clonal populations) will be required to investigate maintenance, and hence epigenetic memory, of DNA methylation and gene expression levels through subsequent cell divisions.

More broadly, analog cell memory challenges the concept of cell type as a discrete entity emerging from a sequence of binary decisions that either silence or activate genes [67], as captured by the Waddington epigenetic landscape metaphore [68]. With analog memory, cell fate becomes a fluid entity that arises from a continuum spectrum of choices of gene expression levels. This view supports the possibility for the existence of uncharacterized graded cell types, with functions that have not been appreciated yet due to the lower frequency of these continuous types with respect to the majority of their discrete counterparts, which are more easily identified. An example of this is provided by cells that undergo the endothelial-mesenchymal transition (EMT), a gateway to tumor invasiveness and metastasis [69]. These cells are thought to be in a, yet to be defined, plastic phenotype [70], in which some EMT transcription factor (TF) genes are in a bivalent chromatin state characterized by co-existing activating and repressive histone marks [70, 71], which, in turn, can be mediated by DNA methylation [72]. In-line with our findings, DNA methylation grade at these genes may serve to keep cells in a state poised to transition towards mesenchymal cancer cells, and, in such a case, it may be used as an early predictor of tumor formation. On the other hand, the possibility of controlling the level at which a gene can be persistently

expressed, by modulating DNA methylation grade, could allow the engineering of gradients of cell types, thereby increasing the sophistication and functionality of tissues that can be created. To this end, additional research will be needed in order to re-engineer the chromatin modification circuit such that we can precisely control DNA methylation grade by user-defined inputs, such as small signaling molecules and drugs.

In summary, our findings show that cells have the ability to maintain long-term memory of any gene expression level, and that they can achieve this by stably maintained DNA methylation grades. This indicates that graded cell types are biologically plausible, thereby spurring the need to revisit the notion of cell fate alltogether and paving the way for future tissue engineering tools.

Methods

Cell culture conditions

Cells were maintained in tissue culture plates (Corning) with growth media comprised of Dulbecco's Modified Eagle Medium (DMEM) (Corning) supplemented with 10% FBS (Corning), 1X non-essential amino acids (Gibco), 100 U/ml penicillin (Sigma), and 100 μg/ml streptomycin (Sigma) at 37℃ in a 5% CO2 incubator. The growth media was changed every 2-4 days. For routine passaging, the growth media was removed, followed by the addition of 0.25% trypsin (Corning) and incubation at 37℃ in a 5% CO2 incubator for 7 minutes. Trypsin was then neutralized with growth media at room temperature. The cells were then centrifuged for 3 minutes at 200g, the supernatant was discarded, and the cell pellet was resuspended in fresh growth media. The cells were then diluted (ratio between 1 and 20) and reseeded into new tissue culture plates for subsequent cell culture.

Transfections

Cells were cultured in growth media at 37℃ in a 5% CO2 incubator. The cells were then treated with 0.25% trypsin (Corning) and incubated for 7 minutes at 37℃ in a 5% CO2 incubator. The cell suspension was subsequently neutralized with growth media at room temperature. Cells were centrifuged for 3 min at 200g followed by removal of the supernatant and cell resuspension in fresh growth media. Cells were then seeded in 12-well tissue culture plates (Corning) at 300,000 cells/well and cultured for 24 hours at 37℃ in a 5% CO2 incubator. Growth media was replaced with growth media without antibiotics. Transfection was then performed using Lipofectamine LTX (Invitrogen) according to the manufacturer's instructions. After 24 hours of incubation at 37℃ in a 5% CO2 incubator, replacement for routine growth media supplemented with penicillin and streptomycin was performed. All transfections with rTetR-XTEN80-DNMT3A, rTetR-XTEN80-DNMT3A, rTetR-

XTEN80-TET1 and rTetR-KRAB were performed using 500ng of the fusion protein and 300ng of trasfection marker (EYFP). Transfections with PhlF-KRAB that involved cell sorting were performed using 450ng of either PhlF-KRAB or PhlF, and 450ng of the transfection marker (450ng). Experiments of PhlF-KRAB without cell sorting were perfomed using 450ng of PhlF-KRAB and 450ng of the transfection marker (1:1 stochiometry), 45ng of PhlF-KRAB and 450ng of the transfection marker (0.1:1 stochiometry), or 4.5ng of PhlF-KRAB and 450ng of the transfection marker (0.01:1 stochiometry). An empty vector was used to maintain the DNA amounts constant for the various stoichiometries. Transfections of DNMT3A-dCas9 that involved cell sorting were performed using 500ng of DNMT3A-dCas9, 600ng of the gRNA expression vector, and 300ng of the trasfection marker (EYFP). In experiments using dCas9, 450ng of the gRNA expression vector, 300ng of either DNMT3A-dCas9 or dCas9, and 300ng of the transfection marker (EYFP) were used. All the experiments presented use 2μM of dox and 30μM of DAPG.

Chromosomal integration

The genetic reporter was integrated using site-specific chromosomal integration into an endogenous mammalian locus (Rosa26) in CHO-K1 cells bearing a landing pad (monoallelic) for efficient and precise integration [42]. This locus had been previously identified by a homology-based computational search (BLAST) using the murine Rosa26 locus as reference. EYFP is expressed from the landing pad exclusively before site-specific chromosomal integration into the Rosa26 locus. The landing pad confers puromycin resistance exclusively after site-specific chromosomal integration into the Rosa26 locus. For integration, 500ng of the chromosomal integration vector and 500ng of the Bxb1 recombinase expression vector were transfected into the cells. After 24 hours, routine cell culture was commenced with the supplementation of growth media with puromycin (8μg/ml) for 2 weeks. Subsequently, a fluorescence-activated cell sorter (BD Aria) was utilized to obtain cells that were positive for EBFP2 expression and negative for EYFP expression. Digital PCR was used to confirm 1 genetic reporter per genome (Fig. SE.5E; Methods). The cells were also assayed and confirmed to test negative for mycoplasma contamination (MIT's Koch Institute Preclinical Modeling Core).

DNA construction

DNA cloning was performed using a combination of Golden Gate Assembly, Gibson Assembly, restriction cloning, and PCR cloning. Expression vectors for the epigenetic effectors were cloned using Golden Gate Assembly. The cloning was performed in a single reaction with the plasmids comprising a destination vector, cHS4 chromatin insulator, EF1a promoter, 5' UTR, gene sequence, 3' UTR, and polyadenylation signal. Gene sequences for rTetR-TET1, rTetR-XTEN80-TET1, rTeTR-DNMT3A, rTeTR-XTEN80-DNMT3A, PhlF-KRAB, rTetR-KRAB, and PhlF were synthesized and cloned into a plasmid with compatible overhangs for Golden Gate Assembly

(Azenta Life Sciences). The expression vectors for TET1 and rTetR were cloned by performing PCR cloning using the rTetR-XTEN80-TET1 expression vector as a template. For the genetic reporter, the region comprising the PhlF and rTetR binding sites was synthesized (Azenta Life Sciences) and subsequently cloned upstream of a vector containing the EF1a promoter using restriction cloning. Golden Gate Assembly was then performed in a reaction comprising the EF1a promoter with upstream DNA-binding sites, destination vector, upstream cHS4 chromatin insulator, 5' UTR, EBFP2, 3' UTR, and polyadenylation signal. The resulting vector was cloned along with the downstream cHS4 chromatin insulator into the chromosomal integration vector using Gibson Assembly. All sequences were sequenced verified via Sanger sequencing (Azenta Life Sciences) or whole plasmid sequencing (Primordium).

Flow cytometry

Cells were trypsinized using 0.25% trypsin (Corning) and incubation at 37℃ in a 5% CO2 incubator for 7 minutes. Following this, trypsin was neutralized by adding growth media at room temperature. Afterwards, the cells were centrifuged at 200g for 3 minutes. The supernatant was removed, and the resulting cell pellet was then resuspended in fresh growth media. The cell suspension was filtered through a filter cap into flow cytometry tubes (Falcon). Flow cytometry data was then collected using a flow cytometer (BD LSRFortessa). EBFP2 was measured using a 405nm laser and a 450/50 filter with 259 V, EYFP was measured using a 488nm laser and 530/30 filter with 190 V, mKO2 was measured using a 561nm laser and 610/20 filter with 250 V, iRFP was measured using a 637nm laser and 670/30 filter with 326 V. Cytoflow (version 1.2) was used for analyzing all flow cytometry data and obtaining of cell densities, means, standard deviations, and percentages of flow cytometry measurements. For analysis, measurements were gated for single cells based on forward and side scatter, and only gated measurements were used for subsequent analysis. For EBFP2 percentage calculations, the absolute range for analysis utilized after gating was -100 to 10^5 A.U.F., which contained 100% of the cells. After processing the flow cytometry data using Cytoflow, the data was plotted using either Cytoflow, GraphPad Prism or Matplotlib. Graphpad Prism was used for generating bar plots. For the correlation plot between mean EBFP2 fluorescence and DNA methylation, Cytoflow's gated measurements were imported into MATLAB, where the correlation was performed using the polyfit function.

Time-course flow cytometry

A fluorescence-activated cell sorter (BD Aria) was used to obtain cells with specific levels of the transfection marker (EYFP) or the genetic reporter (EBFP2). For transfection experiments that involved cell sorting, cell sorting was performed between 42-48 hours after transfection. When flow cytometry was performed on the day of cell sorting, a fraction of the cells that were sorted was utilized for flow cytometry measurements (BD

LSRFortessa), and the rest of the cells were reseeded on tissue culture plates. For flow cytometry measurements, cells were trypsinized using 0.25% trypsin (Corning) followed by incubation at 37℃ in a 5% CO2 incubator. Trypsin neutralization was performed with growth media at room temperature. The cells were then centrifuged for 3 min at 200g. The supernatant was removed followed by resuspension of the cells in fresh in growth media. A fraction of the cells was utilized for the acquisition of flow cytometry measurements (BD LSRFortessa). The rest of the cells were diluted (ratio between 1 and 20) and reseeded into new tissue culture plates for subsequent measurements.

Cell sorting

Cells were trypsinized using 0.25% trypsin (Corning) followed by incubation at 37℃ in a 5% CO2 incubator for 7 minutes. Subsequently, trypsin was neutralized with growth media at room temperature. The cells were then centrifuged at 200g for 3 minutes. The supernatant was discarded and the cell pellet was resuspended in growth media supplemented with 2.5g/ml BSA and corresponding small molecules according to the experiment. The cell suspension was then filtered through a filter cap into flow cytometry tubes. Cell sorting was then performed using a fluorescence-activated cell sorter (BD Aria) approximately 42-48 hours after transfection, and cells were collected in growth media supplemented with 1X penicillin/streptomycin and corresponding small molecules according to the experiment. EBFP2 was measured using a 405nm laser and a 450/50 filter with 332 V. EYFP was measured using a 488nm laser and 515/20 filter with 200 V. Cell sorting to study the gene expression dynamics after epigenetic modulation using DNMT3A-dCas9 (Fig. 2D, E) used ranges 100-200, 222-445, 500-1000 and 1150-2300 EYFP A.U.F. Cell sorting to study the gene expression dynamics after epigenetic modulation using PhIF-KRAB (Fig. 2G, H) used ranges 25-100, 100-1000, 1000-10000, and 10000 - 100000 corresponding to EYFP A.U.F. Cell sorting to study histone and DNA methylation changes using MeDIP-qPCR and ChIP-qPCR (Fig. 2F, I) used ranges 3000-100000 EYFP A.U.F. Cell sorting to demonstrate the stability of DNMT3A-silenced (DNMT3A-dCas9) cells expressing intermediate levels of gene expression (Fig. 3A) was performed according to <100 A.U.F for low expression, 200-500 A.U.F for intermediate expression, and >1000 A.U.F for high expression. Cells had been silenced with transfection of DNMT3A-dCas9 targeted to the upstream binding sites of the promoter (Tables SE1 and SE3), cell sorting for 7000-100000 EYFP A.U.F. (transfection marker), and maintained silenced for a minimum of four weeks after transfection. Cell sorting to subdivide cell populations from stable intermediate levels of gene expression (Fig. 3I) was performed according to <100 A.U.F for bin 1, 179-224 for bin 2, 400-500 for bin 3, >1000 A.U.F for bin 4. Cells expressing intermediate levels of gene expression had been sorted from DNMT3A-silenced cells (DNMT3A-dCas9) from the range 300-400 EBFP A.U.F. and maintained in culture for a minimum of four weeks. Cells had been silenced with transfection of DNMT3A-dCas9 targeted to the upstream binding sites (Tables SE1 and SE3), cell sorting for 3000-100000 EYFP A.U.F.

(transfection marker), and maintained silenced for a minimum of four weeks after transfection. Cell sorting for rTetR-XTEN80-DNMT3A (Fig. 5A) and rTetR-KRAB (Fig. 5C) transfections in cells with stable intermediate levels of expression used 3000-100000 EYFP A.U.F. Cell sorting for rTetR-XTEN80-TET1 (Fig. 5B) transfections in cells with stable intermediate levels of expression used 410-2800 EYFP A.U.F. Cells expressing low and intermediate levels of gene expression had been sorted from DNMT3A-silenced cells (DNMT3A-dCas9) using <100 A.U.F for low expression and 200-500 A.U.F for intermediate expression and maintained in culture for a minimum of three weeks. Cells had been silenced with transfection of DNMT3A-dCas9 targeted to the upstream binding sites (Tables SE1 and SE3), cell sorting for 3000-100000 EYFP A.U.F. (transfection marker), and maintained silenced for a minimum of three weeks after transfection. Cell sorting to study the gene expression dynamics after epigenetic modulation using rTetR-XTEN80-DNMT3A (Fig. SE.3A) used ranges 60-445, 500-7000, and 7000-100000 EYFP A.U.F. Cell sorting to study reactivation using rTetR-XTEN80-TET1 (Fig. 6) used ranges 50-345, 410-2800, 3000-100000 EYFP A.U.F for rTetR-XTEN80-TET1 and 3000-100000 EYFP A.U.F for rTetR-XTEN80-DNMT3A. Cell sorting to demonstrate the stability of DNMT3A-silenced (rTetR-XTEN80-DNMT3A) cells expressing intermediate levels of gene expression (Fig. SE.5) was performed according to <80 EBFP2 A.U.F for low expression, and ranges 304-380, 400-500, and 530-662 EBFP2 A.U.F for intermediate expression. The cells had been silenced with transfection of rTetR-XTEN80-DNMT3A, supplementation of dox for 8 days, cell sorting for 60-445 EYFP A.U.F. (transfection marker), and maintained silenced for a minimum of four weeks.

Single-cell sampling and expansion

Single cell sorting was performed using a fluorescence-activated cell sorter (BD Aria) for various levels of EBFP2 fluorescence. For the cells exhibiting low levels of fluorescence, single cells were obtained from range 21-30 A.U.F. and range 50-60 A.U.F. For the cells exhibiting intermediate levels of fluorescence, single cells were obtained from range 200-240 A.U.F, range 254-305 A.U.F, range 320-384 A.U.F, and range 417-500 A.U.F. For the cells exhibiting high levels of fluorescence, single cells were obtained from range 1000-1200 A.U.F and range 1750-2100 A.U.F. From each range, 90 single cells well obtained for a total of 720 single cells, each seeded on a separate well of a 96-well tissue culture plate (Corning) with growth media supplemented with penicillin/streptomycin. Single cells were then cultured under standard cell culture conditions at 37℃ in a 5% CO2 incubator. Growth media was replaced independently for each well every four days. After 14 days of cell culture, 93 monoclonal populations were observed, representing $\geq$10 monoclonal populations for each of the 8 ranges sampled. The cells in Fig. 3 A-E were used for cell sorting at 29 days.

MeDIP-qPCR and ChIP-qPCR

MeDIP-qPCR was performed using the MagMeDIP-qPCR kit (Diagenode) according to the manufacturer's

instructions. ChIP-qPCR was performed using the True MicroChIP-seq kit (C01010132, Diagenode) according to the manufacturer's instructions. All sonication was performed using a Bioruptor Pico (Diagenode). We utilized the anti-5mC antibody in the MagMeDIP-qPCR kit (Diagenode) for DNA methylation. We utilized antibodies for H3K4me3 (C15410003, Diagenode) and H3K9me3 (C15410056, Diagenode) for histone methylation. The qPCRs were performed using Power SYBR Green PCR Master Mix (Applied Biosystems) and primers (Table SE4) in a LightCycler 96 (Roche). Melt curves were used to confirm a single amplification product and the LightCycler 96 Application Software (Roche) was used to obtain the C_t values. For the genetic reporter, the promoter region was amplified. β-Actin (H3K4me3) and IgF2 (H3K9me3 and DNA methylation) were used as reference endogenous genes [32]. Folds reported refer to the standard $\Delta\Delta C_t$ method.

Targeted bisulfite sequencing

Genomic DNA was extracted using the DNeasy Blood & Tissue Kit (Qiagen) according to the manufacture's instructions. Samples were then submitted to Zymo Research for conducting the rest of the assay. Assays targeting CpG sites along the chromosomal integration region comprising the continuous sequence covering all DNA binding sites, promoter and EBFP2 were developed using the Rosefinch tool from Zymo Research. Primers were used to amplify bisulfite-converted DNA from the samples, using the EZ DNA Methylation-Lightning Kit for conversion. Amplified products were pooled, barcoded, and prepared for sequencing on an Illumina MiSeq system with a V2 300bp kit, following paired-end sequencing. Sequencing reads were aligned to the chromosomal integration sequence using Bismark. The estimation of methylation levels for each sampled cytosine was calculated by dividing the count of reads identifying a cytosine (C) by the sum of reads identifying either a cytosine (C) or a thymine (T).

Digital PCR

Genomic DNA extraction was performed with the DNeasy Blood & Tissue Kit (Qiagen), according to the manufacturer's instructions. Samples were then submitted to Azenta Life Sciences for conducting the rest of the assay. A NanoDrop spectrophotometer was first used to assess sample concentration and confirm purity of the samples. The samples were then loaded in triplicate for analysis on a QIAcuity 8.5k 96-Well Nanoplate using the Qiagen QIAcuity digital PCR system, with probes targeting EBFP2 and COG1. Copy number calculation was conducted using the QIAcuity Software Suite (version 2.2.0.26). Each sample was compared to a no-template control to verify the absence of external contamination.

Desing of gRNA sequences

Sequences for gRNAs were designed in Benchiling using the chromosomal integration sequence and the

CHO-K1 genome sequence (National Library of Medicine (NCBI) RefSeq assembly GCF_000223135.1).

Protein structure predictions

Protein structure predictions were performed with AlphaFold2 [73] using MMseqs2 on the Google Colab Platform (ColabFold v1.5.5)[74] on GPUs. AlphaFold2 was used to perform structural predictions using 5 models for each protein. The top ranking predicted structure (according to plDDT score for single chains and pTM score for protein complexes) was then relaxed using Assisted Model Building with Energy Refinement (AMBER) relaxation. The protein structures of PhlF-KRAB, rTetR-KRAB, PhlF, and rTetR were predicted as multimers (homodimers). The protein structures of DNMT3A-dCas9, rTetR-XTEN80-DNMT3A, rTetR-XTEN80-TET1 were predicted as single chains. The structures of rTetR-XTEN80-TET1 and rTetR-XTEN80-DNMT3A were then aligned using the predicted homodimer of rTetR as a template in PyMOL (2.5.2). Minimal rotations ($\leq$1 per linker) were performed at the flexible linkers in PyMOL.

Quantification and statistical analysis

To determine the probability of a specific fraction of CpGs being methylated based on bisulfite sequencing data, which offers the probability of a specific CpG being methylated for the cell population, we employ the following method. This approach is applied to both bisulfite sequencing datasets presented in Figs. 3E and 4D, resulting in the corresponding plots in Figs. 3F and 4F, respectively.

Let us assume that the gene of interest has a total of N CpGs. Then, for any $0 \leq j \leq N$, having j CpGs methylated corresponds to the event where precisely j CpGs are methylated, and all other CpGs (i.e., $N - j$) are unmethylated. Noe, let us define the probability of the described event as P_j, where $0 \leq j \leq N$. Additionally, let the probability of CpG i being methylated be p_i, and the probability of CpG i being unmethylated be q_i, where $1 \leq i \leq N$. The bisulfite sequencing data provide us with p_i, and since the event "CpG unmethylated" is the complement of "CpG methylated", q_i is known and can be expressed as $q_i = 1 - p_i$. Then, the probability that exactly j CpGs are methylated out of a total of N CpGs, where each CpG has its own probability of being methylated (p_i) or not being methylated (q_i), can be calculated by using the following formula:

$$P(\text{Exactly } j \text{ CpGs are methylated}) = \sum_{\substack{S \subseteq \{1,2,\ldots,N\} \\ |S|=j}} \left(\prod_{i \in S} p_i \cdot \prod_{k \in \{1,2,\ldots,N\} \setminus S} q_k \right). \tag{1}$$

More precisely, the sum ($\sum$) is taken over all possible subsets S of events with exactly j elements. For each subset S, we calculate the product of the probabilities of the events in S occurring ($\prod_{i \in S} p_i$). We then calculate the product of the probabilities of the events not in S occurring ($\prod_{k \in \{1,2,\ldots,N\} \setminus S} q_k$). The overall probability is

the sum of these products for all subsets S. In simpler terms, the formula considers all possible combinations of j events occurring out of N events, multiplying the probabilities of those events occurring and the probabilities of the remaining events not occurring in each combination. The sum aggregates these probabilities for all valid combinations, providing the probability that exactly j events happen.

As illustrative example, let us consider the case in which the total number of CpG in the gene of interest are $N = 3$. Then, defining the probability of CpG i to be and not to be methylated as p_i and $q_i = 1 - p_i$, with $i = 1, 2, 3$, we then can calculate the probability of having j CpGs methylated, i.e., P_j, with $j = 0, 1, 2, 3$, using (1), obtaining $P_0 = q_1 q_2 q_3$, $P_1 = p_1 q_2 q_3 + q_1 p_2 q_3 + q_1 q_2 p_3$, $P_2 = p_1 p_2 q_3 + p_1 q_2 p_3 + q_1 p_2 p_3$, and $P_3 = p_1 p_2 p_3$. The probability distribution of the fraction of CpGs methyalated is then obtained by plotting (j, P_j) for $j = 0, 2, ..., N$.

Concerning the best-fit linear regression lines shown in Figs. 3G, 4H, and 4I, they were obtained using MATLAB polyfit function. Furthermore, the p-value associated with the slope coefficient was determined through the MATLAB fitlm function.

For statistical tests comparing percentages calculated from flow cytometry measurements or fold changes from MeDIP-qPCR and ChIP-qPCR, unpaired two sample t-tests were performed.

Computational analysis

All simulations conducted in this paper were done using Gillespie's Stochastic Simulation Algorithm (SSA) [56].

Acknowledgements

We thank Dr. James J. Collins for providing scientific comments and suggestions on the link between the model predictions and the experimental data, Kalon Overholt for providing useful references on DNA methylation and providing feedback on some of the figures, and the Biological Engineering Comm Lab for helping us refine some of the diagrams. We would like to thank the Koch Institute's Flow Cytometry Core at MIT where the cell sorting was performed. Furthermore, we would like to thank our funding: NSF-MODULUS, Award number 2027949.

Declaration of interests

The authors declare no competing interests.

References

1. Graf, T. & Enver, T. Forcing cells to change lineages. *Nature* **462,** 587–94. https://doi.org/10.1038/nature08533 (2009).
2. Kouzarides, T. Chromatin modifications and their function. *Cell* **128,** 693–705. https://doi.org/10.1016/j.cell.2007.02.005 (2007).
3. Allis, C. D., Caparros, M.-L., Jenuwein, T. & Reinberg, D. *Epigenetics* (Cold Spring Harbor Laboratory Press, Second Edition, 2015).
4. Huang, S., Litt, M. & Blakey, C. A. *Epigenetic Gene Expression and Regulation* (Academic Press, 2015).
5. Heard, E. & Martienssen, R. A. Transgenerational epigenetic inheritance: myths and mechanisms. *Cell* **157,** 95–109. https://doi.org/10.1016/j.cell.2014.02.045 (2014).
6. Allis, C. D. & Jenuwein, T. The molecular hallmarks of epigenetic control. *Nat Rev Genet* **17,** 487–500. https://doi.org/10.1038/nrg.2016.59 (2016).
7. Li, E. & Zhang, Y. DNA methylation in mammals. *Cold Spring Harb Perspect Biol* **6.** https://doi.org/10.1101/cshperspect.a019133 (2014).
8. Cheng, X. Structural and functional coordination of DNA and histone methylation. *Cold Spring Harb Perspect Biol.* **6,** 693–705. https://doi.org/10.1101/cshperspect.a018747 (2014).
9. Bannister, A. J. *et al.* Selective recognition of methylated lysine 9 on histone H3 by the HP1 chromo domain. *Nature* **410,** 120–4. https://doi.org/10.1038/35065138 (2001).
10. Jones, P. L. *et al.* Methylated DNA and MeCP2 recruit histone deacetylase to repress transcription. *Nat Genet* **19,** 187–191. https://doi.org/10.1038/561 (1998).
11. Schneider, R. *et al.* Histone H3 lysine 4 methylation patterns in higher eukaryotic genes. *Nat Cell Biol* **6,** 73–7. https://doi.org/10.1038/ncb1076 (2003).
12. Hathaway, N. A. *et al.* Dynamics and memory of heterochromatin in living cells. *Cell* **149,** 1447–1460. https://doi.org/10.1016/j.cell.2012.03.052 (2012).
13. Zhang, T., Cooper, S. & Brockdorff, N. The interplay of histone modifications - writers that read. *EMBO Rep* **16,** 1467–1481. https://doi.org/10.15252/embr.201540945 (2015).
14. Ulm, E. A., Sleiman, S. F. & Chamberlin, H. M. Developmental functions for the Caenorhabditis elegans Sp protein SPTF-3. *Mech Dev* **128,** 428–41. https://doi.org/10.1016/j.mod.2011.08.003 (2011).

15. Dodd, I. B., Micheelsen, M. A., Sneppen, K. & Thon, G. Theoretical Analysis of Epigenetic Cell Memory by Nucleosome Modification. *Cell* **129,** 813–822. https://doi.org/10.1016/j.cell.2007.02.053 (2007).

16. Yamada, T., Fischle, W., Sugiyama, T., Allis, C. D. & Grewal, S. I. S. The nucleation and maintenance of heterochromatin by a histone deacetylase in fission yeast. *Mol Cell* **20,** 173–85. https://doi.org/10.1016/j.molcel.2005.10.002 (2005).

17. Grewal, S. I. & Klar, A. J. Chromosomal inheritance of epigenetic states in fission yeast during mitosis and meiosis. *Cell* **86,** 95–101. https://doi.org/10.1016/s0092-8674(00)80080-x (1996).

18. Stelzer, Y., Shivalila, C. S., Soldner, F., Markoulaki, S. & Jaenisch, R. Tracing dynamic changes of DNA methylation at single-cell resolution. *Cell* **163,** 218–29. https://doi.org/10.1016/j.cell.2015.08.046 (2015).

19. Mattei, A. L., Bailly, N. & Meissner, A. DNA methylation: a historical perspective. *Trends Genet* **38,** 676–707. https://doi.org/10.1016/j.tig.2022.03.010 (2022).

20. Hong, T. *et al.* TET2 modulates spatial relocalization of heterochromatin in aged hematopoietic stem and progenitor cells. *Nat Aging* **3,** 1387–1400. https://doi.org/10.1038/s43587-023-00505-y (2023).

21. Charlton, J. *et al.* TETs compete with DNMT3 activity in pluripotent cells at thousands of methylated somatic enhancers. *Nature genetics* **52,** 819–827. https://doi.org/10.1038/s41588-020-0639-9 (2020).

22. Du, J., Johnson, L. M., Jacobsen, S. E. & Patel, D. J. DNA methylation pathways and their crosstalk with histone methylation. *Nat Rev Mol Cell Biol* **16,** 519–32. https://doi.org/10.1038/nrm4043 (2015).

23. Ooi, S. K. *et al.* DNMT3L connects unmethylated lysine 4 of histone H3 to de novo methylation of DNA. *Nature* **448,** 714–717. https://doi.org/10.1038/nature05987 (2007).

24. Nan, X. *et al.* Transcriptional repression by the methyl-CpG-binding protein MeCP2 involves a histone deacetylase complex. *Nature* **393,** 383–389. https://doi.org/10.1038/30764 (1998).

25. Lopez-Serra, L. & Esteller, M. Proteins that bind methylated DNA and human cancer: reading the wrong words. *Br J Cancer* **98,** 1881–1885. https://doi.org/10.1038/sj.bjc.6604374 (2008).

26. Fuks, F. *et al.* The methyl-CpG-binding protein MeCP2 links DNA methylation to histone methylation. *J Biol Chem* **278,** 4035–4040. https://doi.org/10.1074/jbc.M210256200 (2003).

27. Bruno, S., Williams, R. J. & Del Vecchio, D. Epigenetic cell memory: The gene's inner chromatin modification circuit. *PLOS Computational Biology* **18,** 1–27. https://doi.org/10.1371/journal.pcbi.1009961 (2022).

28. Hay, A. D. *et al.* Epigenetic inheritance is unfaithful at intermediately methylated CpG sites. *Nat Commun* **14,** 5336. https://doi.org/10.1038/nrm4043 (2023).

29. Bird, A. P. & Taggart, M. H. Variable patterns of total DNA and rDNA methylation in animals. *Nucleic Acids Res* **8,** 1485–1497. https://doi.org/10.1093/nar/8.7.1485 (1980).

30. Hodges, E. *et al.* DNA methylation changes and complex intermediate states accompany lineage specificity in the adult hematopoietic compartment. *Molecular cell* **44,** 17–28. https://doi.org/10.1016/j.molcel.2011.08.026 (2011).

31. Stadler, M. B. *et al.* DNA-binding factors shape the mouse methylome at distal regulatory regions. *Nature* **480,** 490–495. https://doi.org/10.1038/nature10716 (2011).

32. Bintu, L. *et al.* Dynamics of epigenetic regulation at the single-cell level. *Science.* https://doi.org/10.1126/science.aab2956 (2016).

33. Ma, Y., Budde, M. W., Zhu, J. & Elowitz, M. B. Tuning methylation-dependent silencing dynamics by synthetic modulation of CpG density. *ACS Synthetic Biology* **12,** 2536–2545 (2023).

34. Lensch, S. *et al.* Dynamic spreading of chromatin-mediated gene silencing and reactivation between neighboring genes in single cells. *Elife* **11,** e75115 (2022).

35. Van, M. V., Fujimori, T. & Bintu, L. Nanobody-mediated control of gene expression and epigenetic memory. *Nature Communications* **12.1,** 537 (2021).

36. Liu, X. S. *et al.* Rescue of fragile X syndrome neurons by DNA methylation editing of the FMR1 gene. *Cell* **172,** 979–992 (2018).

37. Nuñez, J. K. *et al.* Genome-wide programmable transcriptional memory by CRISPR-based epigenome editing. *Cell* **184,** 2503–2519 (2021).

38. Angel, A., Song, J., Dean, C. & Howard, M. A Polycomb-based switch underlying quantitative epigenetic memory. *Nature* **476,** 105–108. https://doi.org/10.1038/nature10241 (2011).

39. Saxton, D. S. & Rine, J. Distinct silencer states generate epigenetic states of heterochromatin. *Mol Cell* **82,** 3566–3579. https://doi.org/10.1016/j.molcel.2022.08.002 (2022).

40. Yao, Z. *et al.* A taxonomy of transcriptomic cell types across the isocortex and hippocampal formation. *Cell* **184,** 3222–3241. https://doi.org/10.1016/j.cell.2021.04.021 (2021).

41. Liu, H. *et al.* DNA methylation atlas of the mouse brain at single-cell resolution. *Nature* **598,** 120–128. https://doi.org/10.1038/s41586-020-03182-8 (2021).

42. Gaidukov, L. *et al.* A multi-landing pad DNA integration platform for mammalian cell engineering. *Nucleic Acids Res.* **46,** 4072–4086 (May 2018).

43. Recillas-Targa, F. *et al.* Position-effect protection and enhancer blocking by the chicken beta-globin insulator are separable activities. *Proc. Natl. Acad. Sci. U. S. A.* **99,** 6883–6888 (May 2002).

44. Stanton, B. C. *et al.* Systematic transfer of prokaryotic sensors and circuits to mammalian cells. *ACS Synth. Biol.* **3,** 880–891 (Dec. 2014).

45. O'Geen, H. *et al.* dCas9-based epigenome editing suggests acquisition of histone methylation is not sufficient for target gene repression. *Nucleic Acids Res.* **45,** 9901–9916 (Sept. 2017).

46. Margolin, J. F. *et al.* Krüppel-associated boxes are potent transcriptional repression domains. *Proc. Natl. Acad. Sci.* **91,** 4509–4513. 10.1073/pnas.91.10.4509 (1994).

47. Schultz, D. C., Ayyanathan, K., Negorev, D., Maul, G. G. & Rauscher, F. J. SETDB1: a novel KAP-1-associated histone H3, lysine 9-specific methyltransferase that contributes to HP1-mediated silencing of euchromatic genes by KRAB zinc-finger proteins. *Annual Review of Physical Chemistry* **16,** 919–32. https://doi.org/10.1101/gad.973302 (2002).

48. Ecco, G., Imbeault, M. & Trono, D. KRAB zinc finger proteins. *Development* **144,** 2719–2729. https://doi.org/10.1242/dev.132605 (2017).

49. Hervouet, E., Peixoto, P., Delage-Mourroux, R., Boyer-Guittaut, M. & Cartron, P.-F. Specific or not specific recruitment of DNMTs for DNA methylation, an epigenetic dilemma. *Clin Epigenetics,* 17. https://doi.org/10.1186/s13148-018-0450-y (2018).

50. Trerotola, M., Relli, V., Simeone, P. & Alberti, S. Epigenetic inheritance and the missing heritability. *Hum Genomics* **9,** 17. https://doi.org/10.1186/s40246-015-0041-3 (2015).

51. Upadhyay, A. K., Horton, J. R., Zhang, X. & Cheng, X. Coordinated methyl-lysine erasure: structural and functional linkage of a Jumonji demethylase domain and a reader domain. *Curr Opin Struct Biol* **21,** 750–60. https://doi.org/10.1016/j.sbi.2011.08.003 (2011).

52. Rasmussen, K. D. & Helin, K. Role of TET enzymes in DNA methylation, development, and cancer. *Genes Dev.* **30,** 733–50. https://doi.org/10.1101/gad.276568.115 (2016).

53. Brown, D. A. *et al.* The SET1 Complex Selects Actively Transcribed Target Genes via Multivalent Interaction with CpG Island Chromatin. *Cell Rep* **20,** 2313–2327. https://doi.org/10.1016/j.celrep.2017.08.030 (2017).

54. Jackson, M. *et al.* Severe global DNA hypomethylation blocks differentiation and induces histone hyperacetylation in embryonic stem cells. *Mol Cell Biol* **24.** https://doi.org/10.1128/MCB.24.20.8862-8871 (2004).

55. Bannister, A. J. & Kouzarides, T. Regulation of chromatin by histone modifications. *Cell Res.* **21,** 381–395.

56. Gillespie, D. T. Stochastic Simulation of Chemical Kinetics. *Annual Review of Physical Chemistry* **58,** 35–55. https://doi.org/10.1146/annurev.physchem.58.032806.104637 (2007).

57. Ren, W. *et al.* Direct readout of heterochromatic H3K9me3 regulates DNMT1-mediated maintenance DNA methylation. *Proceedings of the National Academy of Sciences of the United States of America* **117,** 18439–18447. https://doi.org/10.1073/pnas.2009316117 (2020).

58. Laird, C. D. *et al.* Hairpin-bisulfite PCR: assessing epigenetic methylation patterns on complementary strands of individual DNA molecules. *Proceedings of the National Academy of Sciences of the United States of America* **101,** 204–209. https://doi.org/10.1073/pnas.2536758100 (2004).

59. Riggs, A. & Xiong, Z. Methylation and epigenetic fidelity. *Proceedings of the National Academy of Sciences of the United States of America* **101,** 4–5. https://doi.org/10.1073/pnas.2536758100 (2004).

60. Ito, S. *et al.* Tet proteins can convert 5-methylcytosine to 5-formylcytosine and 5-carboxylcytosine. *Science* **333,** 1300–3. https://doi.org/10.1126/science.1210597 (2011).

61. Liu, X. S. *et al.* Editing DNA methylation in the mammalian genome. *Cell* **167,** 233–247 (Sept. 2016).

62. Lim, Y. *et al.* A complex association between DNA methylation and gene expression in human placenta at first and third trimesters. *Nat Aging* **12,** e0181155. https://doi.org/10.1371/journal.pone.0181155 (2017).

63. Kulis, M. *et al.* Epigenomic analysis detects widespread gene-body DNA hypomethylation in chronic lymphocytic leukemia. *Nat Genet* **44,** 1236–42. https://doi.org/10.1038/ng.2443 (2012).

64. Sui, D. *et al.* Fine-tuning of iPSC derivation by an inducible reprogramming system at the protein level. *Stem Cell Reports* **2,** 721–33. https://doi.org/10.1016/j.stemcr.2014.03.013 (2014).

65. Clark, S. J. *et al.* scNMT-seq enables joint profiling of chromatin accessibility DNA methylation and transcription in single cells. *Nat Commun* **9,** 781. https://doi.org/10.1038/s41467-018-03149-4 (2018).

66. Argelaguet, R. *et al.* Multi-omics profiling of mouse gastrulation at single-cell resolution. *Nature* **576,** 487–491. https://doi.org/10.1038/s41586-019-1825-8 (2019).

67. Zeng, H. What is a cell type and how to define it? *Cell* **185,** 2739–2755. https://doi.org/10.1016/j.cell.2022.06.031 (2022).

68. Waddington, C. H. *The strategy of the genes* (Routledge, 1957).

69. Kalluri, R. & Weinberg, R. A. The basics of epithelial-mesenchymal transition. *J Clin Invest* **119,** 1420–8. https://doi.org/10.1172/JCI39104 (2009).

70. Chaffer, C. L., San Juan, B. P., Lim, E. & Weinberg, R. A. EMT, cell plasticity and metastasis. *Cancer Metastasis Rev* **35,** 645–654. https://doi.org/10.1007/s10555-016-9648-7 (2016).

71. Lin, Y.-T. & Wu, K.-J. Epigenetic regulation of epithelial-mesenchymal transition: focusing on hypoxia and TGF- signaling. *J Biomed Sci* **27,** 39. https://doi.org/10.1186/s12929-020-00632-3 (2020).

72. Matsumura, Y. *et al.* H3K4/H3K9me3 Bivalent Chromatin Domains Targeted by Lineage-Specific DNA Methylation Pauses Adipocyte Differentiation. *Mol Cell* **60,** 584–96. https://doi.org/10.1016/j.molcel.2015.10.025 (2015).

73. Jumper, J. *et al.* Highly accurate protein structure prediction with AlphaFold. *Nature* **596,** 583–589. ISSN: 1476-4687. https://doi.org/10.1038/s41586-021-03819-2 (Aug. 2021).

74. Mirdita, M. *et al.* ColabFold: making protein folding accessible to all. *Nature Methods* **19,** 679–682. ISSN: 1548-7105. https://doi.org/10.1038/s41592-022-01488-1 (June 2022).

75. Jin, C. *et al.* TET1 is a maintenance DNA demethylase that prevents methylation spreading in differentiated cells. *Nucleic Acids Research* **42,** 6956–71. https://doi.org/10.1093/nar/gku372 (2014).

76. Huisinga, K. L., Brower-Toland, B. & Elgin, S. C. The contradictory definitions of heterochromatin: transcription and silencing. *Chromosoma* **115,** 110–22. https://doi.org/10.1007/s00412-006-0052-x (2006).

77. Del Vecchio, D. & Murray, R. M. *Biomolecular Feedback Systems* (Princeton University Press, 2014).

78. Bruno, S., Williams, R. J. & Del Vecchio, D. *Model reduction and stochastic analysis of the histone modification circuit* in *2022 European Control Conference (ECC)* (2022), 264–271.

79. Felsenfeld, G. & Groudine, M. Controlling the double helix. *Nature* **421,** 448–53. https://doi.org/10.1038/nature01411 (2003).

80. Friedman, N., Cai, L. & Xie, X. S. Linking Stochastic Dynamics to Population Distribution: An Analytical Framework of Gene Expression. *Phys. Rev. Lett* **97.** https://doi.org/10.1103/PhysRevLett.97.168302 (2006).

Supplementary Information (SI)

S.1 Model of chromatin modification circuit

The chromatin modification circuit reaction model considered in our study, shown in Fig. SM.1A, was constructed starting from the one in [27] and it is based on known molecular interactions from the literature. Here, we give a brief description of the reaction model (see [27] for additional details). The chromatin modifications considered in the circuit are H3K9 methylation (H3K9me3), H3K4 methylation (H3K4me3), and DNA methylation. The basic unit of the model is the nucleosome with DNA wrapped around it, D, that can be modified with H3K4me3, $\mathrm{D^A}$, DNA methylation, $\mathrm{D_1^R}$, H3K9me3, $\mathrm{D_2^R}$, or both H3K9me3 and DNA methylation, $\mathrm{D_{12}^R}$. The reaction model can be graphically represented by the circuit of Fig. SM.1A, whose associated reactions are given in SI Section S.6, Table SM.1. More precisely, writer enzymes have the ability to *de novo* establish chromatin marks. Additionally, histone modifications recruit writer enzymes for the same modification to nearby modifiable nucleosomes (*auto-catalysis*) [3, 12, 13, 50], and DNA methylation and repressive histone modification cooperate by recruiting each other's writer enzymes (*cross-catalysis*) [26]. Ultimately, these modifications can be passively removed through dilution during DNA replication or by the action of eraser enzymes (*basal erasure*). Both activating and repressive modifications are involved in the recruitment of each other's eraser enzymes (*recruited erasure*) [4, 51–53].

Now, defining the number of $\mathrm{D^A}, \mathrm{D_1^R}, \mathrm{D_2^R}, \mathrm{D_{12}^R}, \mathrm{D}$ as n^A, n_1^R, n_2^R, n_{12}^R, and n^D, let us derive the related ordinary differential equation (ODE) model in terms of the fractions $\bar{D}^A = n^A/\mathrm{D_{tot}}$, $\bar{D}_1^R = n_{D_1^R}/\mathrm{D_{tot}}$, $\bar{D}_2^R = n_{D_2^R}/\mathrm{D_{tot}}$, $\bar{D}_{12}^R = n_{D_{12}^R}/\mathrm{D_{tot}}$ and $\bar{D} = n_D/\mathrm{D_{tot}}$, with $\mathrm{D_{tot}}$ the total number of nucleosomes in a gene of interest. This can be done by assuming that $\mathrm{D_{tot}}$ is sufficiently large so that $\bar{D}^A$, $\bar{D}_1^R$, $\bar{D}_2^R$, $\bar{D}_{12}^R$ and $\bar{D}$ can be treated as real number. Now, let us introduce $D_{tot} = \mathrm{D_{tot}}/\Omega$ where Ω is the reaction volume, and define the normalized inputs: $u_{10}^R = k_{W0}^1/k_M^A D_{tot}$, $u_1^R = k_W^1/(k_M^A D_{tot})$, $u_{20}^R = k_{W0}^2/(k_M^A D_{tot})$, $u_2^R = k_W^2/(k_M^A D_{tot})$, $u_0^A = k_{W0}^A/(k_M^A D_{tot})$, and $u^A = k_W^A/(k_M^A D_{tot})$. Furthermore, let us introduce the following dimensionless parameters:

$$\alpha = \frac{k_M}{k_M^A} \quad \bar{\alpha} = \frac{\bar{k}_M}{k_M^A}, \quad \alpha' = \frac{k'_M}{k_M^A}, \tag{SM.1}$$

in which α ($\bar{\alpha}$, α') is the non-dimensional rate constant associated with auto-catalysis (cross-catalysis). Let

$$\varepsilon = \frac{\delta + \bar{k}_E^A}{k_M^A D_{tot}}, \quad \varepsilon' = \frac{k_E^A}{k_M^A}, \quad \mu = \frac{k_E^R}{k_E^A}, \quad \mu' = \frac{k_T'^*}{k_E^A}, \tag{SM.2}$$

with $b = O(1)$ such that $(\delta + \bar{k}_E^R)/(\delta + \bar{k}_E^A) = b\mu$ and $\beta = O(1)$ such that $(\delta' + k'_T)/(\delta + \bar{k}_E^A) = \beta\mu'$. Then,

μ (μ') encapsulates the asymmetry between the erasure rate of repressive histone modifications (the DNA demethylation rate) and the erasure rate of activating marks. Furthermore, given that $(\delta + \bar{k}_E^R)/(k_M^A D_{tot}) = b\varepsilon\mu$, $(\delta' + k_T')/(k_M^A D_{tot}) = \beta\varepsilon\mu'$, $k_E^R/k_M^A = \mu\varepsilon'$ and $k_T'^*/k_M^A = \mu'\varepsilon'$, ε (ε') is a parameter that scales the ratio between the basal (recruited) erasure rate and the auto-catalysis rate of each modification. Considering the normalized time $\tau = tk_M^A D_{tot}$, the ODEs associated with the chromatin modification circuit are

$$
\begin{aligned}
\frac{d\bar{D}_1^R}{d\tau} &= (u_{10}^R + u_1^R + \alpha'(\bar{D}_2^R + \bar{D}_{12}^R))\bar{D} + \mu(b\varepsilon + \varepsilon'\bar{D}^A)\bar{D}_{12}^R - (u_{20}^R + \alpha(\bar{D}_2^R + \bar{D}_{12}^R) + \bar{\alpha}(\bar{D}_1^R + \bar{D}_{12}^R))\bar{D}_1^R \\
&\quad - \mu'(\beta\varepsilon + \varepsilon'\bar{D}^A))\bar{D}_1^R \\
\frac{d\bar{D}_{12}^R}{d\tau} &= (u_{10}^R + \alpha'(\bar{D}_2^R + \bar{D}_{12}^R))\bar{D}_2^R + (u_{20}^R + \alpha(\bar{D}_2^R + \bar{D}_{12}^R) + \bar{\alpha}(\bar{D}_1^R + \bar{D}_{12}^R))\bar{D}_1^R \\
&\quad - (\mu'(\beta\varepsilon + \varepsilon'\bar{D}^A) + \mu(b\varepsilon + \varepsilon'\bar{D}^A))\bar{D}_{12}^R \qquad \text{(SM.3)} \\
\frac{d\bar{D}_2^R}{d\tau} &= (u_{20}^R + u_2^R + \alpha(\bar{D}_2^R + \bar{D}_{12}^R) + \bar{\alpha}(\bar{D}_1^R + \bar{D}_{12}^R))\bar{D} + \mu'(\beta\varepsilon + \varepsilon'\bar{D}^A)\bar{D}_{12}^R - (u_{10}^R + \alpha'(\bar{D}_2^R + \bar{D}_{12}^R))\bar{D}_2^R \\
&\quad - \mu(b\varepsilon + \varepsilon'\bar{D}^A))\bar{D}_2^R \\
\frac{d\bar{D}^A}{d\tau} &= (u_0^A + u^A + \bar{D}^A)\bar{D} - (\varepsilon + \varepsilon'(\bar{D}_2^R + \bar{D}_{12}^R) + \varepsilon'(\bar{D}_1^R + \bar{D}_{12}^R))\bar{D}^A,
\end{aligned}
$$

with $\bar{D} = 1 - \bar{D}_1^R - \bar{D}_{12}^R - \bar{D}_2^R - \bar{D}^A$ (see [27] for full derivation). It is important to note that in our genetic reporter, the expression of fluorescent protein EBFP2 is driven by a constitutive promoter. This means that the promoter remains active continuously under normal conditions, without the need for external activators. This is the reason why, for $\mathrm{D^A}$, we introduce a constant non-basal *de-novo* establishment term ($u^A > 0$). As for the other species, we will describe in the following section how external inputs, such as KRAB, DNMT3A, and TET1, modulate the parameters of the chromatin modification circuit model.

S.1.1 How KRAB, DNMT3A and TET1 modulate model parameters

In our study, we exploit KRAB, DNMT3A, and TET1 to modulate chromatin modification state and they affect the model parameters as follows. KRAB is a well-known epigenetic effector that mediates the recruitment of H3K9me3 writers [47]. As we introduce KRAB through transient transfection, its concentration will gradually decrease due to dilution until it eventually dies out. Furthermore, KRAB is fused to the DNA binding domain (DBD) PhlF. This fusion not only allows us to obtain sequence-specific recruitment, but also to regulate the binding and unbinding of KRAB through DAPG, as DAPG inhibits the ability of PhlF-KRAB to bind to DNA. To incorporate these aspects into our model, we write the expression for k_W^2, i.e., reaction rate constant for H3K9me3

establishment (see reactions in SI Table SM.1), as follows:

$$k_W^2 = \tilde{k}_W^2 \frac{1}{1 + \frac{DAPG}{K_2}} W_2 e^{-\delta t}, \tag{SM.4}$$

in which W_2 is the total amount of PhlF-KRAB, $\tilde{k}_W^2$ is a parameter independent of PhlF-KRAB, K_2 is the dissociation constant related to the binding - unbinding reactions between DAPG and PhlF-KRAB, and δ is the dilution rate constant. Then, the normalized input u_2^R in the ODE model (SM.3) can be written as

$$u_2^R = \frac{k_W^2}{k_M^A D_{tot}} = \frac{\tilde{k}_W^2}{k_M^A} \frac{1}{1 + \frac{DAPG}{K_2}} \frac{W_2}{D_{tot}} e^{-\frac{\delta}{k_M^A D_{tot}} t k_M^A D_{tot}} = \tilde{u}_2^R \frac{1}{1 + \frac{DAPG}{K_2}} \bar{W}_2 e^{-\varepsilon\tau}, \tag{SM.5}$$

in which we define $\tilde{u}_2^R = \tilde{k}_W^2 / k_M^A$ and $\bar{W}_2 = W_2 / D_{tot}$.

The enzyme DNMT3A is a DNA methyltransferase that catalyzes *de novo* DNA methylation ([3], Chapter 5) and, as a consequence, it modulates the rate of *de novo* DNA methylation establishment k_W^1 (see reactions in SI Table SM.1). As for KRAB, we introduce DNMT3 through transient transfection, and therefore its concentration will gradually decrease. To incorporate this aspect into our model, we can modify the expression for k_W^1 as follows:

$$k_W^1 = \tilde{k}_W^1 W_1 e^{-\delta t}, \tag{SM.6}$$

in which W_1 is the total amount of DNMT3A and $\tilde{k}_W^1$ is a parameter independent of DNMT3A. Then, the normalized input u_1^R in the ODE model (SM.3) can be written as

$$u_1^R = \frac{k_W^1}{k_M^A D_{tot}} = \frac{\tilde{k}_W^1}{k_M^A} \frac{W_1}{D_{tot}} e^{-\frac{\delta}{k_M^A D_{tot}} t k_M^A D_{tot}} = \tilde{u}_1^R \bar{W}_1 e^{-\varepsilon\tau}, \tag{SM.7}$$

in which we define $\tilde{u}_1^R = \tilde{k}_W^1 / k_M^A$ and $\bar{W}_1 = W_1 / D_{tot}$.

Finally, TET1 is an enzyme that catalyzes the conversion of DNA methylation into modifications that are not recognized by the maintenance enzyme DNMT1, and hence are passively removed through dilution [4, 52, 75]. This enzyme then modulates the constants k_T' and $k_T'^*$ in the reactions of SI Table SM.1. As for KRAB, we introduce TET1 through transient transfection and we fuse it to a DBD. More specifically, we employ rTetR, a DBD that binds DNA exclusively in the presence of Doxycycline (Dox). To incorporate these aspects into our model, we can modify the expressions for k_T' and $k_T'^*$ as follows:

$$k_T' = k_{T1}' + \tilde{k}_T' \frac{\frac{Dox}{K_1}}{1 + \frac{Dox}{K_1}} T e^{-\delta t}, \quad k_T'^* = k_{T1}'^* + \tilde{k}_T'^* \frac{\frac{Dox}{K_1}}{1 + \frac{Dox}{K_1}} T e^{-\delta t}, \tag{SM.8}$$

in which k'_{T1} (k'^{*}_{T1}) is the component of the rate coefficient that does not depend on the external rTetR-TET1 transiently transfected, T is the total amount of rTetR-TET1 transiently transfected, $\tilde{k}'_T$ and $\tilde{k}'^{*}_T$ are parameters independent of rTetR-TET1, and K_1 is the dissociation constant related to the binding - unbinding reactions between Dox and rTetR-TET1. Then, the non-dimensional parameter μ' in the ODE model (SM.3) can be written as

$$\mu' = \frac{k'^{*}_T}{k^A_E} = \frac{k'^{*}_{T1}}{k^A_E} + \frac{\tilde{k}'^{*}_T D_{tot}}{k^A_E} \frac{\frac{Dox}{K_1}}{1+\frac{Dox}{K_1}} \frac{T}{D_{tot}} e^{-\frac{\delta}{k^A_M D_{tot}} t k^A_M D_{tot}} = \mu'_1 + \tilde{\mu}' \frac{\frac{Dox}{K_1}}{1+\frac{Dox}{K_1}} \bar{T} e^{-\varepsilon\tau}, \tag{SM.9}$$

in which we define $\mu'_1 = \frac{k'^{*}_{T1}}{k^A_E}$, $\tilde{\mu}'$, and $\bar{T} = T/D_{tot}$. From (SM.9), it is possible to note that, without transfection of rTetR-TET1, $\mu' = \mu'_1$, indicating that μ' is non-zero. This is because of the presence of passive DNA demethylation. However, previous experimental studies suggest that passive DNA demethylation, although present, is a slow process [32, 54].

S.2 Model of transcriptional regulation

The gene expression process involves two main steps. The first step is transcription, during which the genetic information is transcribed from DNA into mRNA (m). The second step is translation, during which the mRNA is translated into the gene product (X). Chromatin state affects transcription by modulating nucleosome compaction and then gene expression [3, 76]. Thus, we assume that transcription is predominantly allowed by $\mathrm{D^A}$, while allowing a low level of transcription to D and to all the species characterized by repressive chromatin modifications. Furthermore, mRNA m is subject to dilution due to cell division and degradation, while the gene product X is subject to dilution only. This is because fluorescent reporters are highly stable and thus not degraded but only diluted [77]. The reactions associated with the gene expression model can be found in SI Table SM.3. Considering the normalized time $\tau = t k^A_M D_{tot}$ and introducing the non-dimensional parameters $\bar{\beta}^A_m = \beta^A_m / k^A_M D_{tot}$, $\bar{\beta}_m = \beta_m / k^A_M D_{tot}$, $\bar{\beta} = \beta / k^A_M D_{tot}$, $\bar{\gamma}_m = \gamma_m / k^A_M D_{tot}$, $\bar{\delta} = \delta / k^A_M D_{tot}$, the ODE model for X and m can be written as

$$\frac{d\bar{m}}{d\tau} = \bar{\beta}^A_m \bar{D}^A + \bar{\beta}_m (\bar{D} + \bar{D}^R_1 + \bar{D}^R_2 + \bar{D}^R_{12}) - \bar{\gamma}_m \bar{m}, \quad \frac{d\bar{X}}{d\tau} = \bar{\beta}\bar{m} - \bar{\delta}\bar{X}. \tag{SM.10}$$

In this paper, we will refer to the model that combines the complete chromatin modification circuit model (SI Section S.1, equations (SM.3)) along with the transcriptional regulation model outlined in this section as the "4D+X model".

S.3 Effect of α' and μ' on the behavior of the system

In this section, we analyze the stochastic behavior of the 4D+X model with a specific focus on understanding how the parameters α' (normalized rate of DNA methylation establishment through repressive histone modifications) and μ' (ratio between the DNA demethylation rate and the activating histone modification erasure rate) affect the probability distribution of gene expression levels and thus the type of memory that can be achieved.

When the rate of DNA demethylation is 0 ($\mu' = 0$), achieving analog memory is possible only when repressive histone modification (H3K9me3) does not catalyze the *de novo* establishment of DNA methylation ($\alpha' = 0$) (Fig. SM.1B). For $\alpha' > 0$, the gene expression level shifts either to a low or high level. Furthermore, the higher α', the more the distribution tends to shift towards a low gene expression level (Fig. SM.2 - top panel). When μ' is different from 0, only digital memory can be achieved (Fig. SM.2 - intermediate and bottom panels). Moreover, the higher μ' is, the more the gene expression level shifts towards a high level (Fig. SM.2 - bottom panel). Overall, these results suggest that analog memory can be achieved only when DNA demethylation rate is sufficiently small compared to histone modification erasure rate (that is, μ' can be approximated as zero on the time scales of interest) and DNA methylation is not catalyzed by repressive histone modifications ($\alpha' = 0$).

If these conditions are verified, and external inputs (KRAB, DNMT3A, and TET1) are not applied or are applied transiently (transient transfection), then the number of nucleosomes with methylated DNA stabilizes at a constant value. Introducing the variable $\bar{Y}_1 = \bar{D}_1^R + \bar{D}_{12}^R$, that is, the fraction of nucleosomes with methylated DNA in the gene, the behavior of the original model (SM.3) can be captured by a reduced 2D ordinary differential equation (ODE) model below:

$$\frac{d\bar{D}_2^R}{d\tau} = (\alpha\bar{D}_2^R + \bar{\alpha}\bar{Y}_1)\bar{D} - \mu(b\varepsilon + \varepsilon'\bar{D}^A)\bar{D}_2^R, \qquad \frac{d\bar{D}^A}{d\tau} = (u^A + \bar{D}^A)\bar{D} - (\varepsilon + \varepsilon'(\bar{D}_2^R + \bar{Y}_1))\bar{D}^A, \qquad \text{(SM.11)}$$

with $\bar{D} = 1 - \bar{D}^A - \bar{D}_2^R - \bar{Y}_1$ and $\bar{Y}_1 = constant$ (full derivation below). A representative diagram of the reduced system is depicted in Fig. SM.1C. It is important to point out that in the original model of chromatin modification circuit, it is assumed that the basic unit is a nucleosome with DNA wrapped around it and with only one modifiable CpG [27]. There are cases in which this assumption is not verified. However, it is possible to demonstrate that removing this assumption yields a similar reduced model. This indicates that the assumption does not impact the qualitative results regarding the influence of the parameters α' and μ' on the probability distribution of gene expression levels (see SI Section S.7).

Derivation of model (SM.11)

Let us first merge the rates linked to the enhancement of H3K9me3 establishment by $\bar{D}_{12}^R$ into a single rate. We will assume that this rate is identical to the one associated with the enhancement of H3K9me3 establishment by $\bar{D}_1^R$. Similarly, let us merge the rates linked to the recruited erasure of H3K4me3 by $\bar{D}_{12}^R$ into a single rate and assume that this rate is identical to the one associated with the recruited erasure of H3K4me3 by $\bar{D}_1^R$. These simplifying assumptions do not affect the qualitative results related to the effect of the cooperative and competitive interactions among chromatin modifications on epigenetic cell memory. The ODE system (SM.3) can then be rewritten as

$$\begin{aligned}
\frac{d\bar{D}_1^R}{d\tau} &= (u_{10}^R + u_1^R + \alpha'(\bar{D}_2^R + \bar{D}_{12}^R))\bar{D} + \mu(b\varepsilon + \varepsilon'\bar{D}^A)\bar{D}_{12}^R - (u_{20}^R + \alpha(\bar{D}_2^R + \bar{D}_{12}^R) + \bar{\alpha}(\bar{D}_1^R + \bar{D}_{12}^R))\bar{D}_1^R \\
&\quad - \mu'(\beta\varepsilon + \varepsilon'\bar{D}^A))\bar{D}_1^R \\
\frac{d\bar{D}_{12}^R}{d\tau} &= (u_{10}^R + \alpha'(\bar{D}_2^R + \bar{D}_{12}^R))\bar{D}_2^R + (u_{20}^R + \alpha\bar{D}_2^R + \bar{\alpha}(\bar{D}_1^R + \bar{D}_{12}^R))\bar{D}_1^R \\
&\quad - (\mu'(\beta\varepsilon + \varepsilon'\bar{D}^A) + \mu(b\varepsilon + \varepsilon'\bar{D}^A))\bar{D}_{12}^R \\
\frac{d\bar{D}_2^R}{d\tau} &= (u_{20}^R + u_2^R + \alpha\bar{D}_2^R + \bar{\alpha}(\bar{D}_1^R + \bar{D}_{12}^R))\bar{D} + \mu'(\beta\varepsilon + \varepsilon'\bar{D}^A)\bar{D}_{12}^R - (u_{10}^R + \alpha'(\bar{D}_2^R + \bar{D}_{12}^R))\bar{D}_2^R \\
&\quad - \mu(b\varepsilon + \varepsilon'\bar{D}^A))\bar{D}_2^R \\
\frac{d\bar{D}^A}{d\tau} &= (u_0^A + u^A + \bar{D}^A)\bar{D} - (\varepsilon + \varepsilon'(\bar{D}_2^R) + \varepsilon'(\bar{D}_1^R + \bar{D}_{12}^R))\bar{D}^A,
\end{aligned} \tag{SM.12}$$

Now, let us rewrite system (SM.12) by assuming negligible basal *de novo* establishment ($u_{10}^R = u_{20}^R = u_0^A = 0$) and introducing the variable $\bar{Y}_1 = \bar{D}_1^R + \bar{D}_{12}^R$, which corresponds to the fraction of nucleosomes with methylated DNA. We then obtain

$$\begin{aligned}
\frac{d\bar{Y}_1}{d\tau} &= (u_1^R)\bar{D} + (\alpha'(\bar{D}_2^R + \bar{D}_{12}^R))(\bar{D} + \bar{D}_2^R) - \mu'(\beta\varepsilon + \varepsilon'\bar{D}^A)\bar{Y}_1 \\
\frac{d\bar{D}_{12}^R}{d\tau} &= (\alpha'(\bar{D}_2^R + \bar{D}_{12}^R))\bar{D}_2^R + (\alpha\bar{D}_2^R + \bar{\alpha}\bar{Y}_1)\bar{D}_1^R - (\mu'(\beta\varepsilon + \varepsilon'\bar{D}^A) + \mu(b\varepsilon + \varepsilon'\bar{D}^A))\bar{D}_{12}^R \\
\frac{d\bar{D}_2^R}{d\tau} &= (u_2^R + \alpha\bar{D}_2^R + \bar{\alpha}\bar{Y}_1)\bar{D} + \mu'(\beta\varepsilon + \varepsilon'\bar{D}^A)\bar{D}_{12}^R - (\alpha'(\bar{D}_2^R + \bar{D}_{12}^R))\bar{D}_2^R - (\mu(b\varepsilon + \varepsilon'\bar{D}^A))\bar{D}_2^R \\
\frac{d\bar{D}^A}{d\tau} &= (u^A + \bar{D}^A)\bar{D} - (\varepsilon + \varepsilon'\bar{D}_2^R + \varepsilon'\bar{Y}_1)\bar{D}^A,
\end{aligned} \tag{SM.13}$$

with $\bar{D} = 1 - \bar{Y}_1 - \bar{D}_2^R - \bar{D}^A$. Based on previous experimental results [32] and our experimental findings (see Fig. 2I), we can further simplify our model by accounting for the fact that the enhancement of DNA methylation

establishment by H3K9me3 is negligible, i.e., $\alpha' = 0$. The ODE system (SM.13) can then be rewritten as

$$\begin{aligned}
\frac{d\bar{Y}_1}{d\tau} &= (u_1^R)\bar{D} - \mu'(\beta\varepsilon + \varepsilon'\bar{D}^A)\bar{Y}_1 \\
\frac{d\bar{D}_{12}^R}{d\tau} &= (\alpha\bar{D}_2^R + \bar{\alpha}\bar{Y}_1)\bar{D}_1^R - (\mu'(\beta\varepsilon + \varepsilon'\bar{D}^A) + \mu(b\varepsilon + \varepsilon'\bar{D}^A))\bar{D}_{12}^R \\
\frac{d\bar{D}_2^R}{d\tau} &= (u_2^R + \alpha\bar{D}_2^R + \bar{\alpha}\bar{Y}_1)\bar{D} + \mu'(\beta\varepsilon + \varepsilon'\bar{D}^A)\bar{D}_{12}^R - \mu(b\varepsilon + \varepsilon'\bar{D}^A)\bar{D}_2^R \\
\frac{d\bar{D}^A}{d\tau} &= (u^A + \bar{D}^A)\bar{D} - (\varepsilon + \varepsilon'\bar{D}_2^R + \varepsilon'\bar{Y}_1)\bar{D}^A,
\end{aligned} \tag{SM.14}$$

with $\bar{D} = 1 - \bar{Y}_1 - \bar{D}_2^R - \bar{D}^A$. Now, let us rewrite the ODE system (SM.14) introducing the expressions for u_2^R, u_1^R, and μ' derived in SI Section S.1.1 (Expressions (SM.5), (SM.7), and (SM.9)):

$$\begin{aligned}
\frac{d\bar{Y}_1}{d\tau} &= \tilde{u}_1^R\bar{W}_1 e^{-\varepsilon\tau}\bar{D} - (\mu_1' + \tilde{\mu}'\frac{\frac{Dox}{K_1}}{1+\frac{Dox}{K_1}}\bar{T}e^{-\varepsilon\tau})(\beta\varepsilon + \varepsilon'\bar{D}^A)\bar{Y}_1 \\
\frac{d\bar{D}_{12}^R}{d\tau} &= (\alpha\bar{D}_2^R + \bar{\alpha}\bar{Y}_1)\bar{D}_1^R - ((\mu_1' + \tilde{\mu}'\frac{\frac{Dox}{K_1}}{1+\frac{Dox}{K_1}}\bar{T}e^{-\varepsilon\tau})(\beta\varepsilon + \varepsilon'\bar{D}^A) + \mu(b\varepsilon + \varepsilon'\bar{D}^A))\bar{D}_{12}^R \\
\frac{d\bar{D}_2^R}{d\tau} &= (\tilde{u}_2^R\frac{1}{1+\frac{DAPG}{K_2}}\bar{W}_2 e^{-\varepsilon\tau} + \alpha\bar{D}_2^R + \bar{\alpha}\bar{Y}_1)\bar{D} + (\mu_1' + \tilde{\mu}'\frac{\frac{Dox}{K_1}}{1+\frac{Dox}{K_1}}\bar{T}e^{-\varepsilon\tau})(\beta\varepsilon + \varepsilon'\bar{D}^A)\bar{D}_{12}^R - \mu(b\varepsilon + \varepsilon'\bar{D}^A)\bar{D}_2^R \\
\frac{d\bar{D}^A}{d\tau} &= (u^A + \bar{D}^A)\bar{D} - (\varepsilon + \varepsilon'\bar{D}_2^R + \varepsilon'\bar{Y}_1)\bar{D}^A,
\end{aligned} \tag{SM.15}$$

with $\bar{D} = 1 - \bar{Y}_1 - \bar{D}_2^R - \bar{D}^A$ and $\bar{D}_1^R = \bar{Y}_1 - \bar{D}_{12}^R$. Let us now consider the parameter regime in which the rate of DNA demethylation, without transfection of rTetR-TET1, is sufficiently low compared to histone modification dynamics, i.e., $\mu_1' \approx 0$. This assumption is consistent with experimental data that suggest that the passive DNA demethylation is a slow process [32, 54]. The system (SM.15) can then be rewritten as follows:

$$\begin{aligned}
\frac{d\bar{Y}_1}{d\tau} &= \tilde{u}_1^R\bar{W}_1 e^{-\varepsilon\tau}\bar{D} - \tilde{\mu}'\frac{\frac{Dox}{K_1}}{1+\frac{Dox}{K_1}}\bar{T}e^{-\varepsilon\tau}(\beta\varepsilon + \varepsilon'\bar{D}^A)\bar{Y}_1 \\
\frac{d\bar{D}_{12}^R}{d\tau} &= (\alpha\bar{D}_2^R + \bar{\alpha}\bar{Y}_1)\bar{D}_1^R - (\tilde{\mu}'\frac{\frac{Dox}{K_1}}{1+\frac{Dox}{K_1}}\bar{T}e^{-\varepsilon\tau}(\beta\varepsilon + \varepsilon'\bar{D}^A) + \mu(b\varepsilon + \varepsilon'\bar{D}^A))\bar{D}_{12}^R \\
\frac{d\bar{D}_2^R}{d\tau} &= (\tilde{u}_2^R\frac{1}{1+\frac{DAPG}{K_2}}\bar{W}_2 e^{-\varepsilon\tau} + \alpha\bar{D}_2^R + \bar{\alpha}\bar{Y}_1)\bar{D} + \tilde{\mu}'\frac{\frac{Dox}{K_1}}{1+\frac{Dox}{K_1}}\bar{T}e^{-\varepsilon\tau}(\beta\varepsilon + \varepsilon'\bar{D}^A)\bar{D}_{12}^R - \mu(b\varepsilon + \varepsilon'\bar{D}^A)\bar{D}_2^R \\
\frac{d\bar{D}^A}{d\tau} &= (u^A + \bar{D}^A)\bar{D} - (\varepsilon + \varepsilon'\bar{D}_2^R + \varepsilon'\bar{Y}_1)\bar{D}^A,
\end{aligned} \tag{SM.16}$$

with $\bar{D} = 1 - \bar{Y}_1 - \bar{D}_2^R - \bar{D}^A$ and $\bar{D}_1^R = \bar{Y}_1 - \bar{D}_{12}^R$. From (SM.16), it follows that, after a temporary phase during which the externally transfected inputs decrease, $e^{-\varepsilon\tau} \approx 0$ and then $d\bar{Y}_1/d\tau \approx 0$, and the last two ODEs in (SM.16) depend only on $\bar{D}_2^R$, $\bar{D}^A$, and $\bar{Y}_1$. This implies that, after a transient change, $\bar{Y}_1$ stabilizes at a constant

value and the behavior of the original model can be captured by the reduced two-dimensional ODE model given by the last two equations in (SM.16), that corresponds to the ODE model in (SM.11).

S.4 Effect of ε and ε' on the behavior of the system

In this section, we analyze the deterministic and stochastic behavior of our system, with a specific focus on understanding the effect of parameters ε (parameter that scales the ratio between the basal erasure rate and the auto-catalysis rate of each modification) and ε' (parameter that scales the ratio between the recruited erasure rate and the auto-catalysis rate of each modification) on the probability distribution of gene expression levels.

We first conduct a deterministic analysis by studying the ODE model associated with the simplified chromatin modification circuit, i.e., equations (SM.11), and determine how ε and ε' affect the value of $\bar{D}^A$ at the equilibrium for different fractions of methylated CpGs in the gene, i.e., $\bar{Y}_1$ (Fig. SM.3A). When ε is large, the system consistently exhibits a unique stable steady state characterized by low $\bar{D}^A$ (Fig. SM.3A). The value of $\bar{D}^A$ is smaller for higher $\bar{Y}_1$. As ε decreases, the steady-state value of D^A increases, particularly for low values of $\bar{Y}_1$, where $\bar{D}^A \approx 1$ (Fig. SM.3A). Further reduction in ε results in the system becoming bistable for intermediate values of $\bar{Y}_1$ (Fig. SM.3A). Changes in ε' do not significantly impact these trends, except for when ε is small. In such cases, larger values of ε' reduce the range of $\bar{Y}_1$ for bistability and diminish the difference in the values of $\bar{D}^A$ between the two steady states (Fig. SM.3A). We next study the impact of ε and ε' on the number of methylated CpGs at equilibrium for various initial levels of DNMT3A, represented by $\bar{W}_1$ as defined in SI Eq. (SM.6) (Fig. SM.3B). In general, $\bar{Y}_1$ increases with higher $\bar{W}_1$. However, for large values of ε, $\bar{Y}_1$ remains low over an extended range of $\bar{W}_1$ values. As ε decreases, $\bar{Y}_1$ reaches higher values. In the case of small ε, an increase in ε' results in a more ultrasensitive curve.

Overall, this analysis suggests that high fractions of nucleosomes with H3K4me3, and then a high level of gene expression, is achievable only when ε is sufficiently small (Fig. SM.3A). In this parameter regime, when ε' is sufficiently high, $\bar{Y}_1$ has an ultrasensitive response to DNMT3A transient dosage and then different ranges of DNMT3A pulse height would lead to either high or low gene expression levels only (Fig. SM.1D and Fig. SM.3B). To validate these findings, we use the Stochastic Simulation Algorithm (SSA) [56] to perform a computational study on the 4D+X model, that is, the model that incorporates the full chromatin modification circuit, whose reactions are listed in SI Tables SM.1 and SM.3 (Fig. SM.1E and Fig. SM.3C). Here, we consider several ranges of the initial amount of DNMT3A transfected ($\bar{W}_1$), which are uniformly distributed.

For different ranges of initial DNMT3A transfection levels, a bimodal probability distribution of gene expression

levels emerges when ε' is sufficiently large (Fig. SM.3C, left-hand side plots). As ε' decreases, the stationary distribution becomes unimodal (Fig. SM.3C, left-hand side plots). When considering ranges that include higher values of $\bar{W}_1$, it becomes more evident how the unique peak of the distribution shifts towards lower gene expression levels for sufficiently high values of $\bar{W}_1$ (Fig. SM.1E, left-hand side plots and Fig. SM.3C, right-hand side plots).

We then conduct a similar computational analysis to assess the impact of ε and ε' on number of methylated CpGs and gene expression level across various initial levels of TET1 enzyme ($\bar{T}$) (Fig. SM.3D,E). The obtained results mirror those described in the previous analysis (Fig. SM.3B,C).

By looking at our experimental results involving transfection of KRAB (Fig. 2F), it is possible to note that the probability distribution of gene expression levels is bimodal. Previous computational study suggests that this behavior can be obtained only for sufficiently small values of ε [27, 78]. Furthermore, our experimental results involving transfection of DNMT3A (Fig. 2D) also show a bimodal probability distribution for gene expression levels. Based on our mathematical analysis (Fig. SM.3B,C), these outcomes can be observed only when ε is sufficiently small and ε' is sufficiently large. We validate these hypotheses by successfully replicating our experimental data via simulations considering this parameter regime, i.e, small ε, large ε' (Fig. SM.4).

S.5 Refined chromatin modification circuit model to replicate the bisulfite sequencing data from the monoclonal experiment (Fig. 4)

In the study conducted in the previous sections, we observed that, in the absence of external stimuli and when α' and μ' can be assumed equal to zero, the chromatin modification circuit model, whose associated reactions are listed in Table SM.1, predicts a "frozen" level of DNA methylation, i.e., $\dot{\bar{Y}}_1 = 0$ (SI Section S.3). However, this model does not perfectly align with the experimental results obtained from the bisulfite sequencing data of the synthetic reporter system in the eight different clones, each once associated with a distinct EBFP2 expression level (Fig. 4A, C, D, and E). In fact, for each clone, we do not observe a single value for methylated CpGs across the entire cell population. Instead, we observe a distribution with mean and standard deviation that remain approximately constant throughout the observed time points (Fig. 4F). Notably, the distribution of methylated CpGs appears more spread for clones associated with an intermediate level of methylated CpGs.

In order to recapitulate this observed behavior, we incorporated in the full model known molecular mechanisms involved in the DNA methylation maintenance process that were omitted before. Specifically, in the original full

model we have

$$\mathrm{D}_1^{\mathrm{R}} \xrightarrow{\delta'} \mathrm{D}, \tag{SM.17}$$

in which δ' represents the net passive demethylation rate constant obtained from the balance between the dilution and the DNMT1 maintenance process. In order to recapitulate the experimental results, we added the following reactions:

$$\mathrm{D} \xrightarrow{c_0} \mathrm{D}_1^{\mathrm{R}}, \quad \mathrm{D}_1^{\mathrm{R}} \xrightarrow{\tilde{\delta}' \cdot \left(\frac{1}{1+D_2^R/K}\right)} \mathrm{D}, \quad \mathrm{D} \xrightarrow{c \cdot D_2^R} \mathrm{D}_1^{\mathrm{R}}. \tag{SM.18}$$

It is important to point out that, for the sake of simplicity in the description of the DNA methylation maintenance model above, we used, with abuse of notation, $\mathrm{D}_1^{\mathrm{R}}$ to denote any species with DNA methylation and $\mathrm{D}_2^{\mathrm{R}}$ to denote any species with H3K9me3. The first reaction in (SM.18) represents the possibility that the DNA methylation maintenance enzyme DNMT1 can cause *de novo* DNA methylation, although at a very low rate (low c_0) [58, 59]. The second reaction represents the fact that H3K9me3 helps recruit DNMT1 to the gene and then reinforces DNMT1-mediated maintenance [57]. Finally, we introduce the third reaction since H3K9me3 helps recruit DNMT1 and DNMT1 can, by mistake, establish DNA methylation on previously unmethylated sites.

Considering the normalized time $\tau = tk_M^A D_{tot}$ and introducing the non-dimensional parameters $\bar{\delta}' = \delta'/k_M^A D_{tot}$, $\bar{\tilde{\delta}}' = \tilde{\delta}'/k_M^A D_{tot}$, $\bar{c}_0 = c_0/k_M^A D_{tot}$, $\bar{c} = c/k_M^A$, the ODE describing the dynamics of fraction of nucleosomes with methylated DNA, that is, $\bar{Y}_1$, can be then rewritten as

$$\frac{d\bar{Y}_1}{d\tau} = (\bar{c}_0 + \bar{c}\bar{D}_2^R)\bar{D} - (\bar{\delta}' + \bar{\tilde{\delta}}'\frac{1}{1+\bar{D}_2^R/\bar{K}})\bar{D}_1^R. \tag{SM.19}$$

Then, the average level of DNA methylation remains approximately constant in time when $d\bar{Y}_1/d\tau \approx 0$, that is, if all the reaction rate constants are sufficiently small ($\bar{c}_0, \bar{c}, \bar{\delta}', \bar{\tilde{\delta}}' \ll 1$).

This is confirmed by the computational study conducted by simulating the reactions of the refined chromatin modification circuit model that incorporates the DNA methylation maintenance model described above, whose reactions are listed in SI Table SM.5, using the SSA (SI Fig. SM.6A). Additionally, this analysis shows that the reactions encapsulating the recruitment mechanism of DNMT1 by H3K9me3 (the second and the third in (SM.18)) are crucial for obtaining broader distributions in correspondence of intermediate levels of methylated CpGs (SI Fig. SM.6B). In fact, as illustrated in the figure, when the rate constants associated with these reactions are low, all distributions have approximately the same height and width. However, higher values of these rates result in broader distributions at intermediate levels of methylated CpGs.

S.6 4D+X model: reactions

S.6.1 Chromatin modification circuit

In this reaction model, it is assumed that the rate constants of the establishment, auto and cross-catalytic, and erasure processes of H3K9me3 (DNA methylation) do not change if the other repressive mark is present on the same modifiable unit. The chromatin modification circuit reaction model can then be written as in SI Table SM.1.

R_j	Reaction	Prop.Func.(a_j)	Param.	R_j	Reaction	Prop.Func.(a_j)	Param.
1	$\mathrm{D} \xrightarrow{k^A_{W0}} \mathrm{D^A}$	$a_1 = k^A_{W0} n^D$	k^A_{W0}	21	$\mathrm{D} + \mathrm{D^R_2} \xrightarrow{k_M} \mathrm{D^R_2} + \mathrm{D^R_2}$	$a_{21} = \frac{k_M}{\Omega} n^D n^R_2$	$\frac{k_M}{\Omega}$
2	$\mathrm{D} \xrightarrow{k^A_W} \mathrm{D^A}$	$a_2 = k^A_W n^D$	k^A_W	22	$\mathrm{D} + \mathrm{D^R_{12}} \xrightarrow{k_M} \mathrm{D^R_2} + \mathrm{D^R_{12}}$	$a_{22} = \frac{k_M}{\Omega} n^D n^R_{12}$	$\frac{k_M}{\Omega}$
3	$\mathrm{D^A} \xrightarrow{\bar{k}^A_E} \mathrm{D}$	$a_3 = \bar{k}^A_E n^A$	$\bar{k}^A_E$	23	$\mathrm{D} + \mathrm{D^R_1} \xrightarrow{\bar{k}_M} \mathrm{D^R_2} + \mathrm{D^R_1}$	$a_{23} = \frac{\bar{k}_M}{\Omega} n^D n^R_1$	$\frac{\bar{k}_M}{\Omega}$
4	$\mathrm{D^A} \xrightarrow{\delta} \mathrm{D}$	$a_4 = \delta n^A$	δ	24	$\mathrm{D} + \mathrm{D^R_{12}} \xrightarrow{\bar{k}_M} \mathrm{D^R_2} + \mathrm{D^R_{12}}$	$a_{24} = \frac{\bar{k}_M}{\Omega} n^D n^R_{12}$	$\frac{\bar{k}_M}{\Omega}$
5	$\mathrm{D} + \mathrm{D^A} \xrightarrow{k^A_M} \mathrm{D^A} + \mathrm{D^A}$	$a_5 = \frac{k^A_M}{\Omega} n^D n^A$	$\frac{k^A_M}{\Omega}$	25	$\mathrm{D^R_2} + \mathrm{D^A} \xrightarrow{k^R_E} \mathrm{D} + \mathrm{D^A}$	$a_{25} = \frac{k^R_E}{\Omega} n^R_2 n^A$	$\frac{k^R_E}{\Omega}$
6	$\mathrm{D^A} + \mathrm{D^R_1} \xrightarrow{k^A_E} \mathrm{D} + \mathrm{D^R_1}$	$a_6 = \frac{k^A_E}{\Omega} n^A n^R_1$	$\frac{k^A_E}{\Omega}$	26	$\mathrm{D^R_1} \xrightarrow{k^2_{W0}} \mathrm{D^R_{12}}$	$a_{26} = k^2_{W0} n^R_1$	k^2_{W0}
7	$\mathrm{D^A} + \mathrm{D^R_{12}} \xrightarrow{k^A_E} \mathrm{D} + \mathrm{D^R_{12}}$	$a_7 = \frac{k^A_E}{\Omega} n^A n^R_{12}$	$\frac{k^A_E}{\Omega}$	27	$\mathrm{D^R_{12}} \xrightarrow{\bar{k}^R_E} \mathrm{D^R_1}$	$a_{27} = \bar{k}^R_E n^R_{12}$	$\bar{k}^R_E$
8	$\mathrm{D^A} + \mathrm{D^R_2} \xrightarrow{k^A_E} \mathrm{D} + \mathrm{D^R_2}$	$a_8 = \frac{k^A_E}{\Omega} n^A n^R_2$	$\frac{k^A_E}{\Omega}$	28	$\mathrm{D^R_{12}} \xrightarrow{\delta} \mathrm{D^R_1}$	$a_{28} = \delta n^R_{12}$	δ
9	$\mathrm{D^A} + \mathrm{D^R_{12}} \xrightarrow{k^A_E} \mathrm{D} + \mathrm{D^R_{12}}$	$a_9 = \frac{k^A_E}{\Omega} n^A n^R_{12}$	$\frac{k^A_E}{\Omega}$	29	$\mathrm{D^R_1} + \mathrm{D^R_2} \xrightarrow{k_M} \mathrm{D^R_{12}} + \mathrm{D^R_2}$	$a_{29} = \frac{k_M}{\Omega} n^R_1 n^R_2$	$\frac{k_M}{\Omega}$
10	$\mathrm{D} \xrightarrow{k^1_{W0}} \mathrm{D^R_1}$	$a_{10} = k^1_{W0} n^D$	k^1_{W0}	30	$\mathrm{D^R_1} + \mathrm{D^R_{12}} \xrightarrow{k_M} \mathrm{D^R_{12}} + \mathrm{D^R_{12}}$	$a_{30} = \frac{k_M}{\Omega} n^R_1 n^R_{12}$	$\frac{k_M}{\Omega}$
11	$\mathrm{D} \xrightarrow{k^1_W} \mathrm{D^R_1}$	$a_{11} = k^1_W n^D$	k^1_W	31	$\mathrm{D^R_1} + \mathrm{D^R_1} \xrightarrow{\bar{k}_M} \mathrm{D^R_{12}} + \mathrm{D^R_1}$	$a_{31} = \frac{\bar{k}_M}{\Omega} \frac{n^R_1(n^R_1-1)}{2}$	$\frac{\bar{k}_M}{\Omega}$
12	$\mathrm{D^R_1} \xrightarrow{k'_T} \mathrm{D}$	$a_{12} = k'_T n^R_1$	k'_T	32	$\mathrm{D^R_1} + \mathrm{D^R_{12}} \xrightarrow{\bar{k}_M} \mathrm{D^R_{12}} + \mathrm{D^R_{12}}$	$a_{32} = \frac{\bar{k}_M}{\Omega} n^R_1 n^R_{12}$	$\frac{\bar{k}_M}{\Omega}$
13	$\mathrm{D^R_1} \xrightarrow{\delta'} \mathrm{D}$	$a_{13} = \delta' n^R_1$	δ'	33	$\mathrm{D^R_{12}} + \mathrm{D^A} \xrightarrow{k^R_E} \mathrm{D^R_1} + \mathrm{D^A}$	$a_{33} = \frac{k^R_E}{\Omega} n^R_{12} n^A$	$\frac{k^R_E}{\Omega}$
14	$\mathrm{D} + \mathrm{D^R_2} \xrightarrow{k'_M} \mathrm{D^R_1} + \mathrm{D^R_2}$	$a_{14} = \frac{k'_M}{\Omega} n^D n^R_2$	$\frac{k'_M}{\Omega}$	34	$\mathrm{D^R_2} \xrightarrow{k^1_{W0}} \mathrm{D^R_{12}}$	$a_{34} = k^1_{W0} n^R_2$	k^1_{W0}
15	$\mathrm{D} + \mathrm{D^R_{12}} \xrightarrow{k'_M} \mathrm{D^R_1} + \mathrm{D^R_{12}}$	$a_{15} = \frac{k'_M}{\Omega} n^D n^R_{12}$	$\frac{k'_M}{\Omega}$	35	$\mathrm{D^R_{12}} \xrightarrow{k'_T} \mathrm{D^R_2}$	$a_{35} = k'_T n^R_{12}$	k'_T
16	$\mathrm{D^R_1} + \mathrm{D^A} \xrightarrow{k'^*_T} \mathrm{D} + \mathrm{D^A}$	$a_{16} = \frac{k'^*_T}{\Omega} n^R_1 n^A$	$\frac{k'^*_T}{\Omega}$	36	$\mathrm{D^R_{12}} \xrightarrow{\delta'} \mathrm{D^R_2}$	$a_{36} = \delta' n^R_{12}$	δ'
17	$\mathrm{D} \xrightarrow{k^2_{W0}} \mathrm{D^R_2}$	$a_{17} = k^2_{W0} n^D$	k^2_{W0}	37	$\mathrm{D^R_2} + \mathrm{D^R_2} \xrightarrow{k'_M} \mathrm{D^R_{12}} + \mathrm{D^R_2}$	$a_{37} = \frac{k'_M}{\Omega} \frac{n^R_2(n^R_2-1)}{2}$	$\frac{k'_M}{\Omega}$
18	$\mathrm{D} \xrightarrow{k^2_W} \mathrm{D^R_2}$	$a_{18} = k^2_W n^D$	k^2_W	38	$\mathrm{D^R_2} + \mathrm{D^R_{12}} \xrightarrow{k'_M} \mathrm{D^R_{12}} + \mathrm{D^R_{12}}$	$a_{38} = \frac{k'_M}{\Omega} n^R_2 n^R_{12}$	$\frac{k'_M}{\Omega}$
19	$\mathrm{D^R_2} \xrightarrow{\bar{k}^R_E} \mathrm{D}$	$a_{19} = \bar{k}^R_E n^R_2$	$\bar{k}^R_E$	39	$\mathrm{D^R_{12}} + \mathrm{D^A} \xrightarrow{k'^*_T} \mathrm{D^R_2} + \mathrm{D^A}$	$a_{39} = \frac{k'^*_T}{\Omega} n^R_{12} n^A$	$\frac{k'^*_T}{\Omega}$
20	$\mathrm{D^R_2} \xrightarrow{\delta} \mathrm{D}$	$a_{20} = \delta n^R_2$	δ				

Table SM.1: Full chromatin modification circuit model: reactions

R_j	Reaction	Prop.Func.(a_j)	Param.	R_j	Reaction	Prop.Func.(a_j)	Param.
1	$\mathrm{D} \xrightarrow{k^A_{W0}} \mathrm{D^A}$	$a_1 = k^A_{W0} n^D$	k^A_{W0}	7	$\mathrm{D} \xrightarrow{k^2_{W0}} \mathrm{D^R_2}$	$a_7 = k^2_{W0} n^D$	k^2_{W0}
2	$\mathrm{D} \xrightarrow{k^A_W} \mathrm{D^A}$	$a_2 = k^A_W n^D$	k^A_W	8	$\mathrm{D} \xrightarrow{k^2_W} \mathrm{D^R_2}$	$a_8 = k^2_W n^D$	k^2_W
3	$\mathrm{D^A} \xrightarrow{\bar{k}^A_E} \mathrm{D}$	$a_3 = \bar{k}^A_E n^A$	$\bar{k}^A_E$	9	$\mathrm{D^R_2} \xrightarrow{\bar{k}^R_E} \mathrm{D}$	$a_9 = \bar{k}^R_E n^R_2$	$\bar{k}^R_E$
4	$\mathrm{D^A} \xrightarrow{\delta} \mathrm{D}$	$a_4 = \delta n^A$	δ	10	$\mathrm{D^R_2} \xrightarrow{\delta} \mathrm{D}$	$a_{10} = \delta n^R_2$	δ
5	$\mathrm{D} + \mathrm{D^A} \xrightarrow{k^A_M} \mathrm{D^A} + \mathrm{D^A}$	$a_5 = \frac{k^A_M}{\Omega} n^D n^A$	$\frac{k^A_M}{\Omega}$	11	$\mathrm{D} + \mathrm{D^R_2} \xrightarrow{k_M} \mathrm{D^R_2} + \mathrm{D^R_2}$	$a_{11} = \frac{k_M}{\Omega} n^D n^R_2$	$\frac{k_M}{\Omega}$
6	$\mathrm{D^A} + \mathrm{D^R_2} \xrightarrow{k^A_E} \mathrm{D} + \mathrm{D^R_2}$	$a_6 = \frac{k^A_E}{\Omega} n^A n^R_2$	$\frac{k^A_E}{\Omega}$	12	$\mathrm{D^R_2} + \mathrm{D^A} \xrightarrow{k^R_E} \mathrm{D} + \mathrm{D^A}$	$a_{12} = \frac{k^R_E}{\Omega} n^R_2 n^A$	$\frac{k^R_E}{\Omega}$

Table SM.2: Histone modification circuit model: reactions

When DNA methylation is not included in the system, the only species included in the model are D, $\mathrm{D^A}$, and $\mathrm{D^R_2}$, and the reactions included in the model become only the ones listed in SI Table SM.2.

S.6.2 Transcriptional regulation

The reactions associated with the gene expression model described in SI Section S.2 are listed in SI Table SM.3. Here, m is the mRNA, X is the gene product, γ_m is the decay rate constant of m due to dilution and degradation, δ is the decay rate constant of X due to dilution, β_m^A, β_m are the transcription rate constants, with $\beta_m < \beta_m^A$, and β is the translation rate constant.

$\mathbf{R}_j$	Reaction	Prop.Func.(a_j)	Param.	$\mathbf{R}_j$	Reaction	Prop.Func.(a_j)	Param.
1	$\mathrm{D^A} \xrightarrow{\beta_m^A} \mathrm{D^A} + \mathrm{m}$	$a_1 = \beta_m^A n^A$	β_m^A	5	$\mathrm{D_{12}^R} \xrightarrow{\beta_m} \mathrm{D_{12}^R} + \mathrm{m}$	$a_5 = \beta_m n_{12}^R$	β_m
2	$\mathrm{D} \xrightarrow{\beta_m} \mathrm{D} + \mathrm{m}$	$a_2 = \beta_m n^D$	β_m	6	$\mathrm{m} \xrightarrow{\beta} \mathrm{m} + \mathrm{X}$	$a_6 = \beta n^m$	β
3	$\mathrm{D_1^R} \xrightarrow{\beta_m} \mathrm{D_1^R} + \mathrm{m}$	$a_3 = \beta_m n_1^R$	β_m	7	$\mathrm{m} \xrightarrow{\gamma_m} \emptyset$	$a_7 = \gamma_m n^m$	γ_m
4	$\mathrm{D_2^R} \xrightarrow{\beta_m} \mathrm{D_2^R} + \mathrm{m}$	$a_4 = \beta_m n_2^R$	β_m	8	$\mathrm{X} \xrightarrow{\delta} \emptyset$	$a_8 = \delta n^X$	δ

Table SM.3: Gene expression model: reactions

When DNA methylation, and then species $\mathrm{D_1^R}$ and $\mathrm{D_{12}^R}$ are not included in the chromatin modification circuit, then the gene expression model can be simplified as in SI Table SM.4.

$\mathbf{R}_j$	Reaction	Prop.Func.(a_j)	Param.	$\mathbf{R}_j$	Reaction	Prop.Func.(a_j)	Param.
1	$\mathrm{D^A} \xrightarrow{\beta_m^A} \mathrm{D^A} + \mathrm{m}$	$a_1 = \beta_m^A n^A$	β_m^A	4	$\mathrm{m} \xrightarrow{\beta} \mathrm{m} + \mathrm{X}$	$a_4 = \beta n^m$	β
2	$\mathrm{D} \xrightarrow{\beta_m} \mathrm{D} + \mathrm{m}$	$a_2 = \beta_m n^D$	β_m	5	$\mathrm{m} \xrightarrow{\gamma_m} \emptyset$	$a_5 = \gamma_m n^m$	γ_m
3	$\mathrm{D_2^R} \xrightarrow{\beta_m} \mathrm{D_2^R} + \mathrm{m}$	$a_3 = \beta_m n_2^R$	β_m	6	$\mathrm{X} \xrightarrow{\delta} \emptyset$	$a_6 = \delta n^X$	δ

Table SM.4: Gene expression model when we remove species $\mathrm{D_1^R}$, $\mathrm{D_{12}^R}$: reactions

S.6.3 DNA methylation maintenance and refined chromatin modification circuit

To recapitulate the experimental results shown in Fig. 4F, modifications need to be made to the reaction system that models the DNA methylation maintenance process, as explained in SI Section S.5. The reaction model for the chromatin modification circuit can then be revised and expressed as detailed in SI Table SM.5.

$\mathbf{R}_j$	Reaction	Prop.Func.(a_j)	Param.	$\mathbf{R}_j$	Reaction	Prop.Func.(a_j)	Param.
1	$\mathrm{D} \xrightarrow{k^A_{W0}} \mathrm{D^A}$	$a_1 = k^A_{W0} n^D$	k^A_{W0}	21	$\mathrm{D} + \mathrm{D}^\mathrm{R}_2 \xrightarrow{k_M} \mathrm{D}^\mathrm{R}_2 + \mathrm{D}^\mathrm{R}_2$	$a_{21} = \frac{k_M}{\Omega} n^D n^R_2$	$\frac{k_M}{\Omega}$
2	$\mathrm{D} \xrightarrow{k^A_W} \mathrm{D^A}$	$a_2 = k^A_W n^D$	k^A_W	22	$\mathrm{D} + \mathrm{D}^\mathrm{R}_{12} \xrightarrow{k_M} \mathrm{D}^\mathrm{R}_2 + \mathrm{D}^\mathrm{R}_{12}$	$a_{22} = \frac{k_M}{\Omega} n^D n^R_{12}$	$\frac{k_M}{\Omega}$
3	$\mathrm{D^A} \xrightarrow{\bar{k}^A_E} \mathrm{D}$	$a_3 = \bar{k}^A_E n^A$	$\bar{k}^A_E$	23	$\mathrm{D} + \mathrm{D}^\mathrm{R}_1 \xrightarrow{\bar{k}_M} \mathrm{D}^\mathrm{R}_2 + \mathrm{D}^\mathrm{R}_1$	$a_{23} = \frac{\bar{k}_M}{\Omega} n^D n^R_1$	$\frac{\bar{k}_M}{\Omega}$
4	$\mathrm{D^A} \xrightarrow{\delta} \mathrm{D}$	$a_4 = \delta n^A$	δ	24	$\mathrm{D} + \mathrm{D}^\mathrm{R}_{12} \xrightarrow{\bar{k}_M} \mathrm{D}^\mathrm{R}_2 + \mathrm{D}^\mathrm{R}_{12}$	$a_{24} = \frac{\bar{k}_M}{\Omega} n^D n^R_{12}$	$\frac{\bar{k}_M}{\Omega}$
5	$\mathrm{D} + \mathrm{D^A} \xrightarrow{k^A_M} \mathrm{D^A} + \mathrm{D^A}$	$a_5 = \frac{k^A_M}{\Omega} n^D n^A$	$\frac{k^A_M}{\Omega}$	25	$\mathrm{D}^\mathrm{R}_2 + \mathrm{D^A} \xrightarrow{k^R_E} \mathrm{D} + \mathrm{D^A}$	$a_{25} = \frac{k^R_E}{\Omega} n^R_2 n^A$	$\frac{k^R_E}{\Omega}$
6	$\mathrm{D^A} + \mathrm{D}^\mathrm{R}_1 \xrightarrow{k^A_E} \mathrm{D} + \mathrm{D}^\mathrm{R}_1$	$a_6 = \frac{k^A_E}{\Omega} n^A n^R_1$	$\frac{k^A_E}{\Omega}$	26	$\mathrm{D}^\mathrm{R}_1 \xrightarrow{k^2_{W0}} \mathrm{D}^\mathrm{R}_{12}$	$a_{26} = k^2_{W0} n^R_1$	k^2_{W0}
7	$\mathrm{D^A} + \mathrm{D}^\mathrm{R}_{12} \xrightarrow{k^A_E} \mathrm{D} + \mathrm{D}^\mathrm{R}_{12}$	$a_7 = \frac{k^A_E}{\Omega} n^A n^R_{12}$	$\frac{k^A_E}{\Omega}$	27	$\mathrm{D}^\mathrm{R}_{12} \xrightarrow{\bar{k}^R_E} \mathrm{D}^\mathrm{R}_1$	$a_{27} = \bar{k}^R_E n^R_{12}$	$\bar{k}^R_E$
8	$\mathrm{D^A} + \mathrm{D}^\mathrm{R}_2 \xrightarrow{k^A_E} \mathrm{D} + \mathrm{D}^\mathrm{R}_2$	$a_8 = \frac{k^A_E}{\Omega} n^A n^R_2$	$\frac{k^A_E}{\Omega}$	28	$\mathrm{D}^\mathrm{R}_{12} \xrightarrow{\delta} \mathrm{D}^\mathrm{R}_1$	$a_{28} = \delta n^R_{12}$	δ
9	$\mathrm{D^A} + \mathrm{D}^\mathrm{R}_{12} \xrightarrow{k^A_E} \mathrm{D} + \mathrm{D}^\mathrm{R}_{12}$	$a_9 = \frac{k^A_E}{\Omega} n^A n^R_{12}$	$\frac{k^A_E}{\Omega}$	29	$\mathrm{D}^\mathrm{R}_1 + \mathrm{D}^\mathrm{R}_2 \xrightarrow{k_M} \mathrm{D}^\mathrm{R}_{12} + \mathrm{D}^\mathrm{R}_2$	$a_{29} = \frac{k_M}{\Omega} n^R_1 n^R_2$	$\frac{k_M}{\Omega}$
10	$\mathrm{D} \xrightarrow{k^1_{W0}} \mathrm{D}^\mathrm{R}_1$	$a_{10} = k^1_{W0} n^D$	k^1_{W0}	30	$\mathrm{D}^\mathrm{R}_1 + \mathrm{D}^\mathrm{R}_{12} \xrightarrow{k_M} \mathrm{D}^\mathrm{R}_{12} + \mathrm{D}^\mathrm{R}_{12}$	$a_{30} = \frac{k_M}{\Omega} n^R_1 n^R_{12}$	$\frac{k_M}{\Omega}$
11	$\mathrm{D} \xrightarrow{k^1_W} \mathrm{D}^\mathrm{R}_1$	$a_{11} = k^1_W n^D$	k^1_W	31	$\mathrm{D}^\mathrm{R}_1 + \mathrm{D}^\mathrm{R}_1 \xrightarrow{\bar{k}_M} \mathrm{D}^\mathrm{R}_{12} + \mathrm{D}^\mathrm{R}_1$	$a_{31} = \frac{\bar{k}_M}{\Omega} \frac{n^R_1(n^R_1-1)}{2}$	$\frac{\bar{k}_M}{\Omega}$
12	$\mathrm{D}^\mathrm{R}_1 \xrightarrow{k'_T} \mathrm{D}$	$a_{12} = k'_T n^R_1$	k'_T	32	$\mathrm{D}^\mathrm{R}_1 + \mathrm{D}^\mathrm{R}_{12} \xrightarrow{\bar{k}_M} \mathrm{D}^\mathrm{R}_{12} + \mathrm{D}^\mathrm{R}_{12}$	$a_{32} = \frac{\bar{k}_M}{\Omega} n^R_1 n^R_{12}$	$\frac{\bar{k}_M}{\Omega}$
13	$\mathrm{D}^\mathrm{R}_1 \xrightarrow{\delta'} \mathrm{D}$	$a_{13} = \delta' n^R_1$	δ'	33	$\mathrm{D}^\mathrm{R}_{12} + \mathrm{D^A} \xrightarrow{k^R_E} \mathrm{D}^\mathrm{R}_1 + \mathrm{D^A}$	$a_{33} = \frac{k^R_E}{\Omega} n^R_{12} n^A$	$\frac{k^R_E}{\Omega}$
14	$\mathrm{D}^\mathrm{R}_1 \xrightarrow{\frac{\tilde{\delta}'}{1+(D^R_2+D^R_{12})/K}} \mathrm{D}$	$a_{14} = \frac{\tilde{\delta}'}{1+(D^R_2+D^R_{12})/K} n^R_1$	$\tilde{\delta}'$	34	$\mathrm{D}^\mathrm{R}_2 \xrightarrow{k^1_{W0}} \mathrm{D}^\mathrm{R}_{12}$	$a_{34} = k^1_{W0} n^R_2$	k^1_{W0}
15	$\mathrm{D} \xrightarrow{c_0} \mathrm{D}^\mathrm{R}_1$	$a_{15} = c_0 n^D$	c_0	35	$\mathrm{D}^\mathrm{R}_{12} \xrightarrow{k'_T} \mathrm{D}^\mathrm{R}_2$	$a_{35} = k'_T n^R_{12}$	k'_T
16	$\mathrm{D} + \mathrm{D}^\mathrm{R}_2 \xrightarrow{c} \mathrm{D}^\mathrm{R}_1 + \mathrm{D}^\mathrm{R}_2$	$a_{16} = \frac{c}{\Omega} n^D n^R_2$	$\frac{c}{\Omega}$	36	$\mathrm{D}^\mathrm{R}_{12} \xrightarrow{\delta'} \mathrm{D}^\mathrm{R}_2$	$a_{36} = \delta' n^R_{12}$	δ'
17	$\mathrm{D} + \mathrm{D}^\mathrm{R}_{12} \xrightarrow{c} \mathrm{D}^\mathrm{R}_1 + \mathrm{D}^\mathrm{R}_{12}$	$a_{17} = \frac{c}{\Omega} n^D n^R_{12}$	$\frac{c}{\Omega}$	37	$\mathrm{D}^\mathrm{R}_{12} \xrightarrow{\frac{\tilde{\delta}'}{1+(D^R_2+D^R_{12})/K}} \mathrm{D}^\mathrm{R}_2$	$a_{14} = \frac{\tilde{\delta}'}{1+(D^R_2+D^R_{12})/K} n^R_{12}$	$\tilde{\delta}'$
18	$\mathrm{D} + \mathrm{D}^\mathrm{R}_2 \xrightarrow{k'_M} \mathrm{D}^\mathrm{R}_1 + \mathrm{D}^\mathrm{R}_2$	$a_{18} = \frac{k'_M}{\Omega} n^D n^R_2$	$\frac{k'_M}{\Omega}$	38	$\mathrm{D}^\mathrm{R}_2 \xrightarrow{c_0} \mathrm{D}^\mathrm{R}_{12}$	$a_{38} = c_0 n^R_2$	c_0
19	$\mathrm{D} + \mathrm{D}^\mathrm{R}_{12} \xrightarrow{k'_M} \mathrm{D}^\mathrm{R}_1 + \mathrm{D}^\mathrm{R}_{12}$	$a_{19} = \frac{k'_M}{\Omega} n^D n^R_{12}$	$\frac{k'_M}{\Omega}$	39	$\mathrm{D}^\mathrm{R}_2 + \mathrm{D}^\mathrm{R}_2 \xrightarrow{c} \mathrm{D}^\mathrm{R}_{12} + \mathrm{D}^\mathrm{R}_2$	$a_{39} = \frac{c}{\Omega} \frac{n^R_2(n^R_2-1)}{2}$	$\frac{c}{\Omega}$
20	$\mathrm{D}^\mathrm{R}_1 + \mathrm{D^A} \xrightarrow{k'^*_T} \mathrm{D} + \mathrm{D^A}$	$a_{20} = \frac{k'^*_T}{\Omega} n^R_1 n^A$	$\frac{k'^*_T}{\Omega}$	40	$\mathrm{D}^\mathrm{R}_2 + \mathrm{D}^\mathrm{R}_{12} \xrightarrow{c} \mathrm{D}^\mathrm{R}_{12} + \mathrm{D}^\mathrm{R}_{12}$	$a_{40} = \frac{c}{\Omega} n^R_2 n^R_{12}$	$\frac{c}{\Omega}$
21	$\mathrm{D} \xrightarrow{k^2_{W0}} \mathrm{D}^\mathrm{R}_2$	$a_{21} = k^2_{W0} n^D$	k^2_{W0}	41	$\mathrm{D}^\mathrm{R}_2 + \mathrm{D}^\mathrm{R}_2 \xrightarrow{k'_M} \mathrm{D}^\mathrm{R}_{12} + \mathrm{D}^\mathrm{R}_2$	$a_{41} = \frac{k'_M}{\Omega} \frac{n^R_2(n^R_2-1)}{2}$	$\frac{k'_M}{\Omega}$
22	$\mathrm{D} \xrightarrow{k^2_W} \mathrm{D}^\mathrm{R}_2$	$a_{22} = k^2_W n^D$	k^2_W	42	$\mathrm{D}^\mathrm{R}_2 + \mathrm{D}^\mathrm{R}_{12} \xrightarrow{k'_M} \mathrm{D}^\mathrm{R}_{12} + \mathrm{D}^\mathrm{R}_{12}$	$a_{42} = \frac{k'_M}{\Omega} n^R_2 n^R_{12}$	$\frac{k'_M}{\Omega}$
23	$\mathrm{D}^\mathrm{R}_2 \xrightarrow{\bar{k}^R_E} \mathrm{D}$	$a_{23} = \bar{k}^R_E n^R_2$	$\bar{k}^R_E$	43	$\mathrm{D}^\mathrm{R}_{12} + \mathrm{D^A} \xrightarrow{k'^*_T} \mathrm{D}^\mathrm{R}_2 + \mathrm{D^A}$	$a_{43} = \frac{k'^*_T}{\Omega} n^R_{12} n^A$	$\frac{k'^*_T}{\Omega}$
24	$\mathrm{D}^\mathrm{R}_2 \xrightarrow{\delta} \mathrm{D}$	$a_{24} = \delta n^R_2$	δ				

Table SM.5: Full chromatin modification circuit model incorporating the refined DNA methylation maintenance model described in SI Section S.5: reactions

S.7 Modification to the chromatin modification circuit model to include more than one CpG per nucleosome

In the original model of the chromatin modification circuit, it is assumed that the basic unit, that is a nucleosome with DNA wrapped around, can have only one modifiable CpG [27]. There are cases in which this assumption is not verified. However, it is possible to show that this assumption does not affect the qualitative results related to the effect of the parameters α' (normalized rate of DNA methylation establishment through repressive histone modifications) and μ' (ratio between the DNA demethylation rate and the activating histone modification erasure rate) on the probability distribution of gene expression levels.

To this end, let us assume that the basic unit of the model, D, is the nucleosome with DNA wrapped around it with two modifiable CpGs. The conclusion obtained in this section would not change if we consider the DNA wrapped around the nucleosome having $n \in \mathbb{Z}^+$ modifiable CpGs. The basic unit of the model can then be modified with H3K4me3, $\mathrm{D^A}$, one DNA methylation, $\mathrm{D^R_1}$, H3K9me3, $\mathrm{D^R_2}$, one DNA methylation and H3K9me3, $\mathrm{D^R_{12}}$, two DNA methylations, $\mathrm{D^R_{11}}$, and two DNA methylation and H3K9me3, $\mathrm{D^R_{112}}$. Now, defining the number of $\mathrm{D^A}, \mathrm{D^R_1}, \mathrm{D^R_2}, \mathrm{D^R_{12}}, \mathrm{D^R_{11}}, \mathrm{D^R_{112}}, \mathrm{D}$ as n^A, n^R_1, n^R_2, n^R_{12}, $n_{D^R_{11}}$, n^R_{112} and n^D, let us derive the related ordinary differential equation (ODE) model in terms of the fractions $\bar{D}^A = n^A/\mathrm{D_{tot}}$, $\bar{D}^R_1 = n_{D^R_1}/\mathrm{D_{tot}}$, $\bar{D}^R_2 = n_{D^R_2}/\mathrm{D_{tot}}$, $\bar{D}^R_{12} = n_{D^R_{12}}/\mathrm{D_{tot}}$, $\bar{D}^R_{11} = n_{D^R_{11}}/\mathrm{D_{tot}}$, $\bar{D}^R_{112} = n_{D^R_{112}}/\mathrm{D_{tot}}$ and $\bar{D} = n_D/\mathrm{D_{tot}}$, with $\mathrm{D_{tot}}$ the total number of nucleosomes on a gene of interest. This can be done by assuming that $\mathrm{D_{tot}}$ is sufficiently large so that $\bar{D}^A$, $\bar{D}^R_1$, $\bar{D}^R_2$, $\bar{D}^R_{12}$ and $\bar{D}$ can be treated as real number. Now, considering the dimensionless parameters and normalized inputs introduced SI Section S.1 and the normalized time $\tau = tk^A_M D_{tot}$, the ODEs associated with the chromatin modification circuit are

$$
\begin{aligned}
\frac{d\bar{D}^R_1}{d\tau} &= (u^R_{10} + u^R_1 + \alpha'(\bar{D}^R_2 + \bar{D}^R_{12} + \bar{D}^R_{112}))\bar{D} + \mu(b\varepsilon + \varepsilon'\bar{D}^A)\bar{D}^R_{12} + \mu'(\beta\varepsilon + \varepsilon'\bar{D}^A)\bar{D}^R_{11} \\
&\quad - (u^R_{20} + \alpha(\bar{D}^R_2 + \bar{D}^R_{12} + \bar{D}^R_{112}) + \bar{\alpha}(\bar{D}^R_1 + \bar{D}^R_{12} + 2\bar{D}^R_{11} + 2\bar{D}^R_{112}))\bar{D}^R_1 \\
&\quad - (u^R_{10} + u^R_1 + \alpha'(\bar{D}^R_2 + \bar{D}^R_{12} + \bar{D}^R_{112}) + \mu'(\beta\varepsilon + \varepsilon'\bar{D}^A))\bar{D}^R_1 \\
\frac{d\bar{D}^R_{12}}{d\tau} &= (u^R_{10} + \alpha'(\bar{D}^R_2 + \bar{D}^R_{12} + \bar{D}^R_{112}))\bar{D}^R_2 \\
&\quad + (u^R_{20} + \alpha(\bar{D}^R_2 + \bar{D}^R_{12} + \bar{D}^R_{112}) + \bar{\alpha}(\bar{D}^R_1 + \bar{D}^R_{12} + 2\bar{D}^R_{11} + 2\bar{D}^R_{112}))\bar{D}^R_1 + \mu'(\beta\varepsilon + \varepsilon'\bar{D}^A)\bar{D}^R_{112} \\
&\quad - (\mu'(\beta\varepsilon + \varepsilon'\bar{D}^A) + \mu(b\varepsilon + \varepsilon'\bar{D}^A) + u^R_{10} + u^R_1 + \alpha'(\bar{D}^R_2 + \bar{D}^R_{12} + \bar{D}^R_{112}))\bar{D}^R_{12}
\end{aligned}
$$

$$
\begin{aligned}
\frac{d\bar{D}_{11}^R}{d\tau} &= (u_{10}^R + u_1^R + \alpha'(\bar{D}_2^R + \bar{D}_{12}^R + \bar{D}_{112}^R))\bar{D}_1^R + \mu(b\varepsilon + \varepsilon'\bar{D}^A)\bar{D}_{112}^R \\
&- (u_{20}^R + \alpha(\bar{D}_2^R + \bar{D}_{12}^R + \bar{D}_{112}^R) + \bar{\alpha}(\bar{D}_1^R + \bar{D}_{12}^R + 2\bar{D}_{11}^R + 2\bar{D}_{112}^R) + \mu'(\beta\varepsilon + \varepsilon'\bar{D}^A))\bar{D}_1^R \\
\frac{d\bar{D}_{112}^R}{d\tau} &= (u_{20}^R + \alpha(\bar{D}_2^R + \bar{D}_{12}^R + \bar{D}_{112}^R) + \bar{\alpha}(\bar{D}_1^R + \bar{D}_{12}^R + 2\bar{D}_{11}^R + 2\bar{D}_{112}^R))\bar{D}_{11}^R \\
&+ (u_{10}^R + \alpha'(\bar{D}_2^R + \bar{D}_{12}^R + \bar{D}_{112}^R))\bar{D}_{12}^R \\
&- (\mu'(\beta\varepsilon + \varepsilon'\bar{D}^A) + \mu(b\varepsilon + \varepsilon'\bar{D}^A))\bar{D}_{112}^R \\
\frac{d\bar{D}_2^R}{d\tau} &= (u_{20}^R + u_2^R + \alpha(\bar{D}_2^R + \bar{D}_{12}^R + \bar{D}_{112}^R) + \bar{\alpha}(\bar{D}_1^R + \bar{D}_{12}^R + 2\bar{D}_{11}^R + 2\bar{D}_{112}^R))\bar{D} + \mu'(\beta\varepsilon + \varepsilon'\bar{D}^A)\bar{D}_{12}^R \\
&- (u_{10}^R + \alpha'(\bar{D}_2^R + \bar{D}_{12}^R + \bar{D}_{112}^R) + \mu(b\varepsilon + \varepsilon'\bar{D}^A))\bar{D}_2^R \\
\frac{d\bar{D}^A}{d\tau} &= (u_0^A + u^A + \bar{D}^A)\bar{D} - (\varepsilon + \varepsilon'(\bar{D}_2^R + \bar{D}_{12}^R + \bar{D}_{112}^R) + \varepsilon'(\bar{D}_1^R + \bar{D}_{12}^R + 2\bar{D}_{11}^R + 2\bar{D}_{112}^R))\bar{D}^A,
\end{aligned}
\tag{SM.20}
$$

with $\bar{D} = 1 - \bar{D}_1^R - \bar{D}_{12}^R - \bar{D}_{11}^R - \bar{D}_{112}^R - \bar{D}_2^R - \bar{D}^A$.

As we did for the original ODE system (SM.3), let us merge the rates linked to the enhancement of H3K9me3 establishment by $\bar{D}_{12}^R$, $\bar{D}_{11}^R$, and $\bar{D}_{112}^R$ into a single rate. We will assume that this rate is identical to the one associated with the enhancement of H3K9me3 establishment by $\bar{D}_1^R$. Similarly, let us merge the rates linked to the recruited erasure of H3K4me3 by $\bar{D}_{12}^R$, $\bar{D}_{11}^R$, and $\bar{D}_{112}^R$ into a single rate and assume that this rate is identical to the one associated with the recruited erasure of H3K4me3 by $\bar{D}_1^R$. The ODE system (SM.20) can then be rewritten as

$$
\begin{aligned}
\frac{d\bar{D}_1^R}{d\tau} &= (u_{10}^R + u_1^R + \alpha'(\bar{D}_2^R + \bar{D}_{12}^R + \bar{D}_{112}^R))\bar{D} + \mu(b\varepsilon + \varepsilon'\bar{D}^A)\bar{D}_{12}^R + \mu'(\beta\varepsilon + \varepsilon'\bar{D}^A)\bar{D}_{11}^R \\
&- (u_{20}^R + \alpha\bar{D}_2^R + \bar{\alpha}(\bar{D}_1^R + \bar{D}_{12}^R + \bar{D}_{11}^R + \bar{D}_{112}^R))\bar{D}_1^R \\
&- (u_{10}^R + u_1^R + \alpha'(\bar{D}_2^R + \bar{D}_{12}^R + \bar{D}_{112}^R) + \mu'(\beta\varepsilon + \varepsilon'\bar{D}^A))\bar{D}_1^R \\
\frac{d\bar{D}_{12}^R}{d\tau} &= (u_{10}^R + \alpha'(\bar{D}_2^R + \bar{D}_{12}^R + \bar{D}_{112}^R))\bar{D}_2^R \\
&+ (u_{20}^R + \alpha\bar{D}_2^R + \bar{\alpha}(\bar{D}_1^R + \bar{D}_{12}^R + \bar{D}_{11}^R + \bar{D}_{112}^R))\bar{D}_1^R + \mu'(\beta\varepsilon + \varepsilon'\bar{D}^A)\bar{D}_{112}^R \\
&- (\mu'(\beta\varepsilon + \varepsilon'\bar{D}^A) + \mu(b\varepsilon + \varepsilon'\bar{D}^A) + u_{10}^R + u_1^R + \alpha'(\bar{D}_2^R + \bar{D}_{12}^R + \bar{D}_{112}^R))\bar{D}_{12}^R \\
\frac{d\bar{D}_{11}^R}{d\tau} &= (u_{10}^R + u_1^R + \alpha'(\bar{D}_2^R + \bar{D}_{12}^R + \bar{D}_{112}^R))\bar{D}_1^R + \mu(b\varepsilon + \varepsilon'\bar{D}^A)\bar{D}_{112}^R \\
&- (u_{20}^R + \alpha\bar{D}_2^R + \bar{\alpha}(\bar{D}_1^R + \bar{D}_{12}^R + \bar{D}_{11}^R + \bar{D}_{112}^R) + \mu'(\beta\varepsilon + \varepsilon'\bar{D}^A))\bar{D}_1^R \\
\frac{d\bar{D}_{112}^R}{d\tau} &= (u_{20}^R + \alpha\bar{D}_2^R + \bar{\alpha}(\bar{D}_1^R + \bar{D}_{12}^R + \bar{D}_{11}^R + \bar{D}_{112}^R))\bar{D}_{11}^R \\
&+ (u_{10}^R + \alpha'(\bar{D}_2^R + \bar{D}_{12}^R + \bar{D}_{112}^R))\bar{D}_{12}^R - (\mu'(\beta\varepsilon + \varepsilon'\bar{D}^A) + \mu(b\varepsilon + \varepsilon'\bar{D}^A))\bar{D}_{112}^R
\end{aligned}
\tag{SM.21}
$$

$$
\begin{aligned}
\frac{d\bar{D}_2^R}{d\tau} &= (u_{20}^R + u_2^R + \alpha\bar{D}_2^R + \bar{\alpha}(\bar{D}_1^R + \bar{D}_{12}^R + \bar{D}_{11}^R + \bar{D}_{112}^R))\bar{D} + \mu'(\beta\varepsilon + \varepsilon'\bar{D}^A)\bar{D}_{12}^R \\
&\quad - (u_{10}^R + \alpha'(\bar{D}_2^R + \bar{D}_{12}^R + \bar{D}_{112}^R) + \mu(b\varepsilon + \varepsilon'\bar{D}^A))\bar{D}_2^R \\
\frac{d\bar{D}^A}{d\tau} &= (u_0^A + u^A + \bar{D}^A)\bar{D} - (\varepsilon + \varepsilon'(\bar{D}_2^R + \bar{D}_1^R + \bar{D}_{12}^R + \bar{D}_{11}^R + \bar{D}_{112}^R))\bar{D}^A,
\end{aligned}
$$

Now, let us rewrite system (SM.21) by assuming negligible basal establishment ($u_{10}^R = u_{20}^R = u_0^A = 0$) and introducing the variable $\bar{Y}_1 = \bar{D}_1^R + \bar{D}_{12}^R$, which corresponds to the fraction of nucleosomes with one methylated CpG, and the variable $\bar{Y}_{1tot} = \bar{D}_1^R + \bar{D}_{12}^R + \bar{D}_{11}^R + \bar{D}_{112}^R$, which corresponds to the fraction of nucleosomes with at least one methylated CpG. We then obtain

$$
\begin{aligned}
\frac{d\bar{D}_1^R}{d\tau} &= (u_1^R + \alpha'(\bar{D}_2^R + \bar{Y}_{1tot} - \bar{D}_1^R - \bar{D}_{11}^R))\bar{D} + \mu(b\varepsilon + \varepsilon'\bar{D}^A)(\bar{Y}_1 - \bar{D}_1^R) + \mu'(\beta\varepsilon + \varepsilon'\bar{D}^A)\bar{D}_{11}^R \\
&\quad - (\alpha\bar{D}_2^R + \bar{\alpha}\bar{Y}_{tot} + u_1^R + \alpha'(\bar{D}_2^R + \bar{Y}_{1tot} - \bar{D}_1^R - \bar{D}_{11}^R) + \mu'(\beta\varepsilon + \varepsilon'\bar{D}^A))\bar{D}_1^R \\
\frac{d\bar{D}_{11}^R}{d\tau} &= (u_1^R + \alpha'(\bar{D}_2^R + \bar{Y}_{1tot} - \bar{D}_1^R - \bar{D}_{11}^R))\bar{D}_1^R + \mu(b\varepsilon + \varepsilon'\bar{D}^A)(\bar{Y}_{1tot} - \bar{Y}_1 - \bar{D}_{11}^R)) \\
&\quad - (\alpha\bar{D}_2^R + \bar{\alpha}\bar{Y}_{1tot} + \mu'(\beta\varepsilon + \varepsilon'\bar{D}^A))\bar{D}_1^R \\
\frac{d\bar{Y}_1}{d\tau} &= u_1^R(\bar{D} - \bar{D}_1^R) + (\alpha'(\bar{D}_2^R + \bar{Y}_{1tot} - \bar{D}_1^R - \bar{D}_{11}^R))(\bar{D} + \bar{D}_2^R) \\
&\quad + \mu'(\beta\varepsilon + \varepsilon'\bar{D}^A)(\bar{Y}_{1tot} - \bar{Y}_1) - (\mu'(\beta\varepsilon + \varepsilon'\bar{D}^A) + \alpha'(\bar{D}_2^R + \bar{Y}_{1tot} - \bar{D}_1^R - \bar{D}_{11}^R))\bar{Y}_1 \\
\frac{d\bar{Y}_{1tot}}{d\tau} &= u_1^R\bar{D} + (\alpha'(\bar{D}_2^R + \bar{Y}_{1tot} - \bar{D}_1^R - \bar{D}_{11}^R))(\bar{D} + \bar{D}_2^R) - \mu'(\beta\varepsilon + \varepsilon'\bar{D}^A))\bar{Y}_1 \\
\frac{d\bar{D}_2^R}{d\tau} &= (u_2^R + \alpha\bar{D}_2^R + \bar{\alpha}\bar{Y}_{1tot})\bar{D} + \mu'(\beta\varepsilon + \varepsilon'\bar{D}^A)\bar{D}_{12}^R - (\alpha'(\bar{D}_2^R + \bar{D}_{12}^R + \bar{D}_{112}^R) + \mu(b\varepsilon + \varepsilon'\bar{D}^A))\bar{D}_2^R \\
\frac{d\bar{D}^A}{d\tau} &= (u^A + \bar{D}^A)\bar{D} - (\varepsilon + \varepsilon'(\bar{D}_2^R + \bar{Y}_{1tot}))\bar{D}^A,
\end{aligned}
\tag{SM.22}
$$

with $\bar{D} = 1 - \bar{Y}_{1tot} - \bar{D}_2^R - \bar{D}^A$. As we did for the ODE system associated with our original chromatin modification circuit in SI Section S.1, we can further simplify our model by assuming that the enhancement of DNA methylation establishment by H3K9me3 is negligible, i.e., $\alpha' = 0$. The ODE system (SM.22) can then be rewritten as

$$
\begin{aligned}
\frac{d\bar{D}_1^R}{d\tau} &= (u_1^R)\bar{D} + \mu(b\varepsilon + \varepsilon'\bar{D}^A)(\bar{Y}_1 - \bar{D}_1^R) + \mu'(\beta\varepsilon + \varepsilon'\bar{D}^A)\bar{D}_{11}^R - (\alpha\bar{D}_2^R + \bar{\alpha}\bar{Y}_{tot} + u_1^R + \mu'(\beta\varepsilon + \varepsilon'\bar{D}^A))\bar{D}_1^R \\
\frac{d\bar{D}_{11}^R}{d\tau} &= (u_1^R)\bar{D}_1^R + \mu(b\varepsilon + \varepsilon'\bar{D}^A)(\bar{Y}_{1tot} - \bar{Y}_1 - \bar{D}_{11}^R)) - (\alpha\bar{D}_2^R + \bar{\alpha}\bar{Y}_{1tot} + \mu'(\beta\varepsilon + \varepsilon'\bar{D}^A))\bar{D}_1^R \\
\frac{d\bar{Y}_1}{d\tau} &= u_1^R(\bar{D} - \bar{D}_1^R) + \mu'(\beta\varepsilon + \varepsilon'\bar{D}^A)(\bar{Y}_{1tot} - \bar{Y}_1) - \mu'(\beta\varepsilon + \varepsilon'\bar{D}^A)\bar{Y}_1 \\
\frac{d\bar{Y}_{1tot}}{d\tau} &= u_1^R\bar{D} - \mu'(\beta\varepsilon + \varepsilon'\bar{D}^A))\bar{Y}_1 \\
\frac{d\bar{D}_2^R}{d\tau} &= (u_2^R + \alpha\bar{D}_2^R + \bar{\alpha}\bar{Y}_{1tot})\bar{D} + \mu'(\beta\varepsilon + \varepsilon'\bar{D}^A)\bar{D}_{12}^R - \mu(b\varepsilon + \varepsilon'\bar{D}^A)\bar{D}_2^R \\
\frac{d\bar{D}^A}{d\tau} &= (u^A + \bar{D}^A)\bar{D} - (\varepsilon + \varepsilon'(\bar{D}_2^R + \bar{Y}_{1tot}))\bar{D}^A,
\end{aligned}
\tag{SM.23}
$$

with $\bar{D} = 1 - \bar{Y}_{1tot} - \bar{D}_2^R - \bar{D}^A$. Now, introducing in (SM.23) the expressions for u_2^R, u_1^R, and μ' derived in SI Section S.1.1 (Expressions (SM.5), (SM.7), and (SM.9)), we obtain:

$$
\begin{aligned}
\frac{d\bar{D}_1^R}{d\tau} &= \tilde{u}_1^R \bar{W}_1 e^{-\varepsilon\tau}\bar{D} + \mu(b\varepsilon + \varepsilon'\bar{D}^A)(\bar{Y}_1 - \bar{D}_1^R) + (\mu_1' + \tilde{\mu}'\frac{\frac{Dox}{K_1}}{1+\frac{Dox}{K_1}}\bar{T}e^{-\varepsilon\tau})(\beta\varepsilon + \varepsilon'\bar{D}^A)\bar{D}_{11}^R \\
&\quad - (\alpha\bar{D}_2^R + \bar{\alpha}\bar{Y}_{tot} + \tilde{u}_1^R\bar{W}_1 e^{-\varepsilon\tau} + (\mu_1' + \tilde{\mu}'\frac{\frac{Dox}{K_1}}{1+\frac{Dox}{K_1}}\bar{T}e^{-\varepsilon\tau})(\beta\varepsilon + \varepsilon'\bar{D}^A))\bar{D}_1^R \\
\frac{d\bar{D}_{11}^R}{d\tau} &= \tilde{u}_1^R \bar{W}_1 e^{-\varepsilon\tau}\bar{D}_1^R + \mu(b\varepsilon + \varepsilon'\bar{D}^A)(\bar{Y}_{1tot} - \bar{Y}_1 - \bar{D}_{11}^R)) \\
&\quad - (\alpha\bar{D}_2^R + \bar{\alpha}\bar{Y}_{1tot} + (\mu_1' + \tilde{\mu}'\frac{\frac{Dox}{K_1}}{1+\frac{Dox}{K_1}}\bar{T}e^{-\varepsilon\tau})(\beta\varepsilon + \varepsilon'\bar{D}^A))\bar{D}_1^R \\
\frac{d\bar{Y}_1}{d\tau} &= \tilde{u}_1^R \bar{W}_1 e^{-\varepsilon\tau}(\bar{D} - \bar{D}_1^R) + (\mu_1' + \tilde{\mu}'\frac{\frac{Dox}{K_1}}{1+\frac{Dox}{K_1}}\bar{T}e^{-\varepsilon\tau})(\beta\varepsilon + \varepsilon'\bar{D}^A)(\bar{Y}_{1tot} - \bar{Y}_1) \\
&\quad - (\mu_1' + \tilde{\mu}'\frac{\frac{Dox}{K_1}}{1+\frac{Dox}{K_1}}\bar{T}e^{-\varepsilon\tau})(\beta\varepsilon + \varepsilon'\bar{D}^A)\bar{Y}_1 \\
\frac{d\bar{Y}_{1tot}}{d\tau} &= \tilde{u}_1^R \bar{W}_1 e^{-\varepsilon\tau}\bar{D} - (\mu_1' + \tilde{\mu}'\frac{\frac{Dox}{K_1}}{1+\frac{Dox}{K_1}}\bar{T}e^{-\varepsilon\tau})(\beta\varepsilon + \varepsilon'\bar{D}^A))\bar{Y}_1 \\
\frac{d\bar{D}_2^R}{d\tau} &= (\tilde{u}_2^R\frac{1}{1+\frac{DAPG}{K_2}}\bar{W}_2 e^{-\varepsilon\tau} + \alpha\bar{D}_2^R + \bar{\alpha}\bar{Y}_{1tot})\bar{D} + \mu'(\beta\varepsilon + \varepsilon'\bar{D}^A)\bar{D}_{12}^R - \mu(b\varepsilon + \varepsilon'\bar{D}^A)\bar{D}_2^R \\
\frac{d\bar{D}^A}{d\tau} &= (u^A + \bar{D}^A)\bar{D} - (\varepsilon + \varepsilon'(\bar{D}_2^R + \bar{Y}_{1tot}))\bar{D}^A,
\end{aligned}
\tag{SM.24}
$$

with $\bar{D} = 1 - \bar{Y}_{1tot} - \bar{D}_2^R - \bar{D}^A$. Furthermore, if we consider the parameter regime in which the rate of DNA demethylation, without transfection of rTetR-TET1, is sufficiently low compared to histone modification dynamics,i.e., $\mu_1' \to 0$, the system (SM.24) can then be rewritten as follows:

$$
\begin{aligned}
\frac{d\bar{D}_1^R}{d\tau} &= \tilde{u}_1^R \bar{W}_1 e^{-\varepsilon\tau}\bar{D} + \mu(b\varepsilon + \varepsilon'\bar{D}^A)(\bar{Y}_1 - \bar{D}_1^R) + \tilde{\mu}'\frac{\frac{Dox}{K_1}}{1+\frac{Dox}{K_1}}\bar{T}e^{-\varepsilon\tau}(\beta\varepsilon + \varepsilon'\bar{D}^A)\bar{D}_{11}^R \\
&\quad - (\alpha\bar{D}_2^R + \bar{\alpha}\bar{Y}_{tot} + \tilde{u}_1^R\bar{W}_1 e^{-\varepsilon\tau} + \tilde{\mu}'\frac{\frac{Dox}{K_1}}{1+\frac{Dox}{K_1}}\bar{T}e^{-\varepsilon\tau}(\beta\varepsilon + \varepsilon'\bar{D}^A))\bar{D}_1^R \\
\frac{d\bar{D}_{11}^R}{d\tau} &= \tilde{u}_1^R \bar{W}_1 e^{-\varepsilon\tau}\bar{D}_1^R + \mu(b\varepsilon + \varepsilon'\bar{D}^A)(\bar{Y}_{1tot} - \bar{Y}_1 - \bar{D}_{11}^R)) \\
&\quad - (\alpha\bar{D}_2^R + \bar{\alpha}\bar{Y}_{1tot} + \tilde{\mu}'\frac{\frac{Dox}{K_1}}{1+\frac{Dox}{K_1}}\bar{T}e^{-\varepsilon\tau}(\beta\varepsilon + \varepsilon'\bar{D}^A))\bar{D}_1^R \\
\frac{d\bar{Y}_1}{d\tau} &= \tilde{u}_1^R \bar{W}_1 e^{-\varepsilon\tau}(\bar{D} - \bar{D}_1^R) + \tilde{\mu}'\frac{\frac{Dox}{K_1}}{1+\frac{Dox}{K_1}}\bar{T}e^{-\varepsilon\tau}(\beta\varepsilon + \varepsilon'\bar{D}^A)(\bar{Y}_{1tot} - \bar{Y}_1) \\
&\quad - \tilde{\mu}'\frac{\frac{Dox}{K_1}}{1+\frac{Dox}{K_1}}\bar{T}e^{-\varepsilon\tau}(\beta\varepsilon + \varepsilon'\bar{D}^A)\bar{Y}_1 \\
\frac{d\bar{Y}_{1tot}}{d\tau} &= \tilde{u}_1^R \bar{W}_1 e^{-\varepsilon\tau}\bar{D} - \tilde{\mu}'\frac{\frac{Dox}{K_1}}{1+\frac{Dox}{K_1}}\bar{T}e^{-\varepsilon\tau}(\beta\varepsilon + \varepsilon'\bar{D}^A))\bar{Y}_1
\end{aligned}
\tag{SM.25}
$$

$$\frac{d\bar{D}_2^R}{d\tau} = (\tilde{u}_2^R \frac{1}{1+\frac{DAPG}{K_2}} \bar{W}_2 e^{-\varepsilon\tau} + \alpha\bar{D}_2^R + \bar{\alpha}\bar{Y}_{1tot})\bar{D} + \mu'(\beta\varepsilon + \varepsilon'\bar{D}^A)\bar{D}_{12}^R - \mu(b\varepsilon + \varepsilon'\bar{D}^A)\bar{D}_2^R$$
$$\frac{d\bar{D}^A}{d\tau} = (u^A + \bar{D}^A)\bar{D} - (\varepsilon + \varepsilon'(\bar{D}_2^R + \bar{Y}_{1tot}))\bar{D}^A,$$

with $\bar{D} = 1 - \bar{Y}_1 - \bar{D}_2^R - \bar{D}^A$. From the fourth equation in (SM.25), it is possible to notice that, following a temporary phase during which the externally transfected inputs decrease, $e^{-\varepsilon\tau} \approx 0$, and then $d\bar{Y}_{1tot}/d\tau \approx 0$. This implies that, once the transient phase concludes, $\bar{Y}_{1tot}$ stabilizes at a constant value and the behavior of the original model can be captured by a reduced 2D model described by the subsequent ODEs:

$$\frac{d\bar{D}_2^R}{d\tau} = (\alpha\bar{D}_2^R + \bar{\alpha}\bar{Y}_{1tot})\bar{D} - \mu(b\varepsilon + \varepsilon'\bar{D}^A)\bar{D}_2^R, \quad \frac{d\bar{D}^A}{d\tau} = (u^A + \bar{D}^A)\bar{D} - (\varepsilon + \varepsilon'(\bar{D}_2^R + \bar{Y}_{1tot}))\bar{D}^A, \quad \text{(SM.26)}$$

with $\bar{D} = 1 - \bar{D}^A - \bar{D}_2^R - \bar{Y}_{1tot}$ and $\bar{Y}_{1tot} = constant$. It is evident that the ODE model (SM.26) closely resembles the original model, in which we assume to have one CpG per nucleosome, i.e., (SM.11), with the only distinction being the presence of $\bar{Y}_{1tot}$ instead of $\bar{Y}_1$. That is, in this revised model, the representation of the fraction of the number of methylated CpGs in the gene is denoted by $\bar{Y}_{1tot}$. Then, the introduction of the simplifying assumption, having one CpG per nucleosome, does not affect the qualitative results of the analysis that focuses on identifying the impact of the parameters α' (normalized rate of DNA methylation establishment through repressive histone modifications) and μ' (ratio between the DNA demethylation rate and the activating histone modification erasure rate) on the probability distribution of gene expression levels.

S.8 Supplementary Modeling Figures

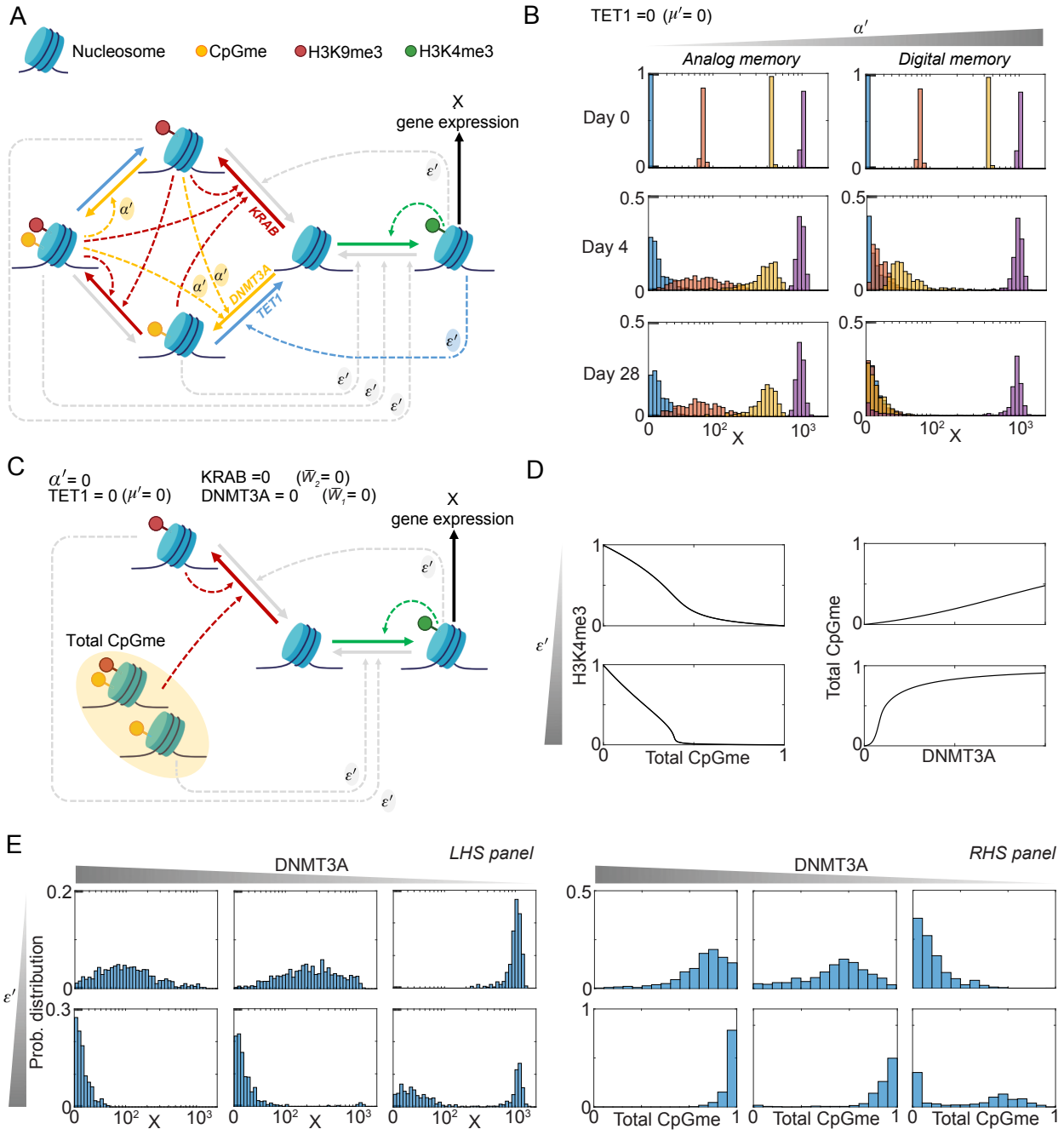

Fig. SM.1. Continued on the following page.

Fig. SM.1. The dynamics of the chromatin modification circuit can be captured by a reduced model, under specific parameter regimes. **A** Full chromatin modification circuit diagram. The species involved are unmodified nucleosome, nucleosome with H3K4me3, nucleosome with H3K9me3, nucleosome with CpGme, and nucleosome with both H3K9me3 and CpGme. We use solid arrows to represent the nucleosome modifications and gene expression. We use dashed arrows to represent the recruitment process and the consequent effect on establishment or erasure. For each arrow, we use red for processes involved in H3K9me3 establishment, orange for processes involved in DNA methylation establishment, green for processes involved in H3K4me3 establishment, light blue for processes involved in DNA demethylation, gray for processes involved in the erasure of histone modifications, and black for gene expression. In particular, $\alpha' = 0$ when H3K9me3 does not recruit writers of DNA methylation. In order to simplify the diagram without compromising the essential interactions among modifications, we removed some non-critical dashed arrows (refer to Fig. 1 in [27] for the complete diagram). **B** Probability distributions of the system represented by reactions listed in SI Tables SM.1 and SM.3. The distributions are obtained computationally using SSA [56] and we indicate with X the gene expression level (logicle scale). In particular, we determine how α' affects the probability distribution of the system when $\mu' = 0$. The parameter values used for these simulations are listed in SI Section S.9. In particular, we consider $\alpha' = 0, 0.1$ and four initial conditions (H3K9me3 and CpGme, CpGme only, H3K9me3 only, H3K4me3)= (n_{12}^R,n_1^R,n_2^R,n^A): (14,0,1,0) (blue), (6,0,8,1) (red), (4,0,5,6) (yellow), and (1,0,1,13) (purple). For each case, the initial value of X at time $t = 0$ was set to its steady state. For all the simulations we set $\alpha = \bar{\alpha} = 1$, $\varepsilon = 0.08$, $\varepsilon' = 25$, $\mu = 0.1$, $b = \beta = 1$. See SI Fig. SM.2 for how different values of α' and μ' influence the probability distribution of the system. **C** Simplified chromatin modification circuit diagram obtained when $\alpha' = 0$, TET1 = 0 (i.e., $\mu' = 0$), DNMT3A = 0 (i.e., $\bar{W}_1 = 0$), KRAB = 0 (i.e., $\bar{W}_2 = 0$). **D** Left-hand side plots: dose-response curve for the (Total CpGme,H3K4me3) pair, i.e, $(\bar{Y}_1, \bar{D}^A)$, for different values of ε' obtained from simulations of system (SM.11) with (Total CpGme,H3K9me3,H3K4me3) $= (\bar{Y}_1, \bar{D}_2^R, \bar{D}^A) = (k, 0, 1-k)$ as initial conditions, with $0 \leq k \leq 1$. Right hand-side plots: dose-response curve for the (DNMT3A,Total CpGme) pair, i.e, $(\bar{W}_1, \bar{Y}_1)$, for different values of ε' obtained from simulations of system (SM.16) with (Total CpGme,H3K9me3,H3K4me3) $= (\bar{Y}_1, \bar{D}_2^R, \bar{D}^A) = (0, 0, 1)$ as initial conditions. The parameter values used for these simulations are listed in SI Section S.9. In particular, we consider $\varepsilon = 0.1$ and $\varepsilon' = 1, 25$ (See SI Fig. SM.3 for how different values of ε and ε' influence the deterministic behavior of the system). Here, the DNMT3A dynamics is modeled as a pulse that exponentially decreases over time. The value on the x-axis corresponds to the DNMT3A value at time 0. **E** Probability distributions of the system, represented by reactions listed in SI Tables SM.1 and SM.3, after t = 28 days. The distributions are obtained computationally using SSA [56]. In the left-hand side panel we show the probability distributions of the gene expression level X (logicle scale) and in the right-hand side panel we show the probability distributions of the total CpGme level. The parameter values used for these simulations are listed in SI Section S.9. In particular, we consider $\varepsilon = 0.13$, $\varepsilon' = 1.5, 25$, DNMT3A $= \bar{W}_1 = [0, 0.4], [2.4, 2.8], [3.4, 3.8]$ and (H3K9me3 and CpGme, CpGme only, H3K9me3 only, H3K4me3) = (n_{12}^R,n_1^R,n_2^R,n^A) = $(0, 0, 0, \mathrm{D_{tot}})$ as initial condition (see SI Fig. SM.3 for how different values of ε and ε' influence the probability distribution of the system). In our model, α' is the normalized rate of DNA methylation establishment through repressive histone modifications, μ' is the ratio between the DNA demethylation rate and the activating histone modification erasure rate, and ε (ε') is the parameter that scales the ratio between the basal (recruited) erasure rate and the auto-catalysis rate of each modification. For panels B and E, we consider $\mathrm{D_{tot}} = 15$ and we consider $N = 1000$ samples to realize each distribution and, for each simulation, the value of $\bar{W}_1$ was randomly selected from a uniformly distributed range, whose extremes are listed above.

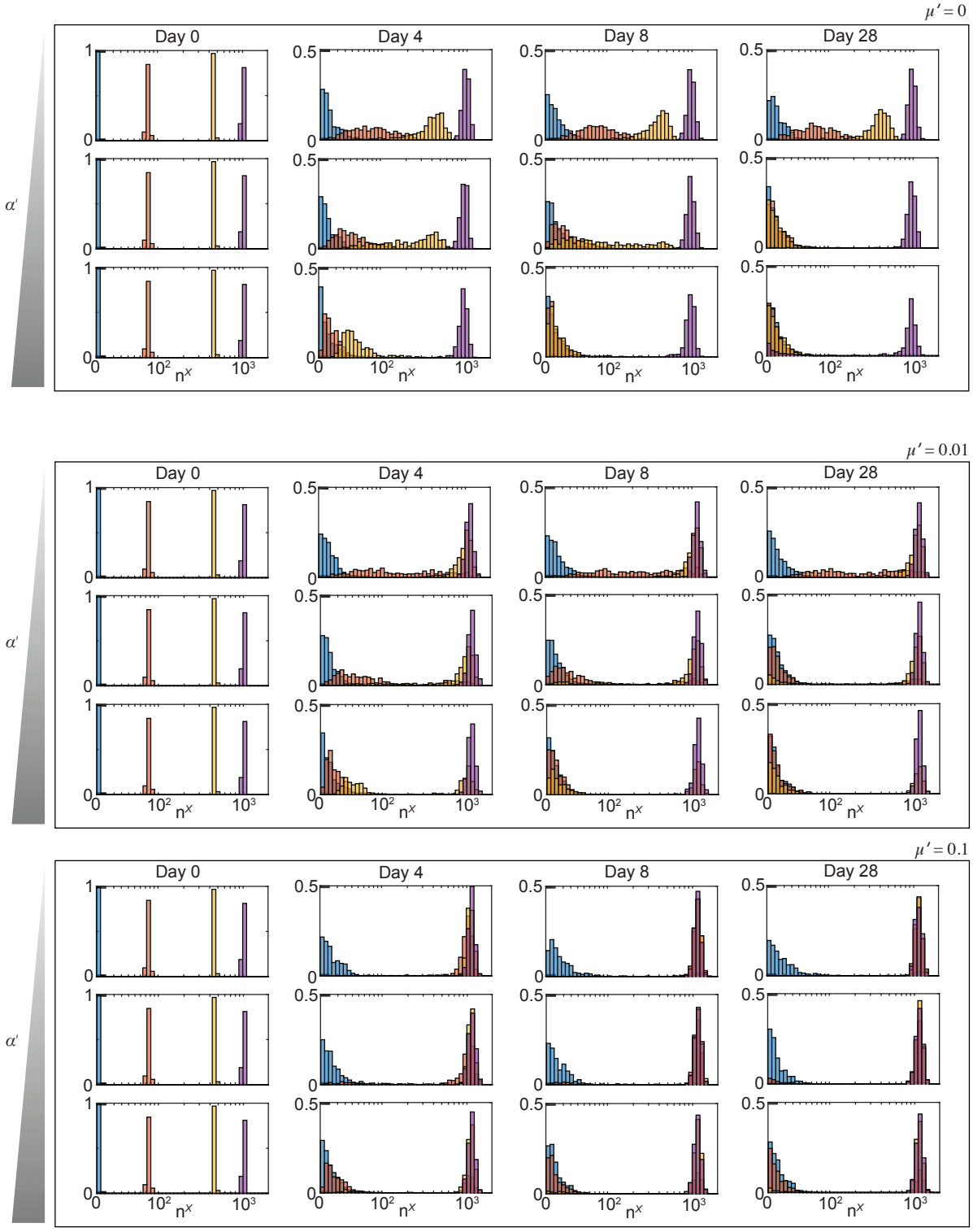

Fig. SM.2. Continued on the following page.

Fig. SM.2. Achieving analog memory is only possible when $\alpha' = 0$ and $\mu' = 0$. Probability distributions of the system represented by reactions listed in SI Tables SM.1 and SM.3. The distributions are obtained computationally using SSA [56] and we indicate with n^X the gene expression level (logicle scale). In particular, we determine how α' and μ' affect the probability distribution of the system. The parameter values used for these simulations are listed in SI Section S.9. In particular, we consider $\alpha' = 0, 0.01, 0.1$ and $\mu' = 0, 0.01, 0.1$ and four initial conditions: (n_{12}^R,n_1^R,n_2^R,n^A) = (14,0,1,0) (blue), (n_{12}^R,n_1^R,n_2^R,n^A) = (6,0,8,1) (red), (n_{12}^R,n_1^R,n_2^R,n^A) = (4,0,5,6) (yellow), (n_{12}^R,n_1^R,n_2^R,n^A) = (1,0,1,13) (purple). For each case, the initial values of n^X of n^m at time $t = 0$ were set to their steady states. For all the simulations we set $\alpha = \bar{\alpha} = 1$, $\varepsilon = 0.08$, $\varepsilon' = 25$, $\mu = 0.1$, $b = \beta = 1$. In our model, α' is the normalized rate of DNA methylation establishment through repressive histone modifications and μ' is the ratio between the DNA demethylation rate and the activating histone modification erasure rate. For all simulations, we consider $\mathrm{D_{tot}} = 15$ and we consider $N = 1000$ samples to realize each distribution.

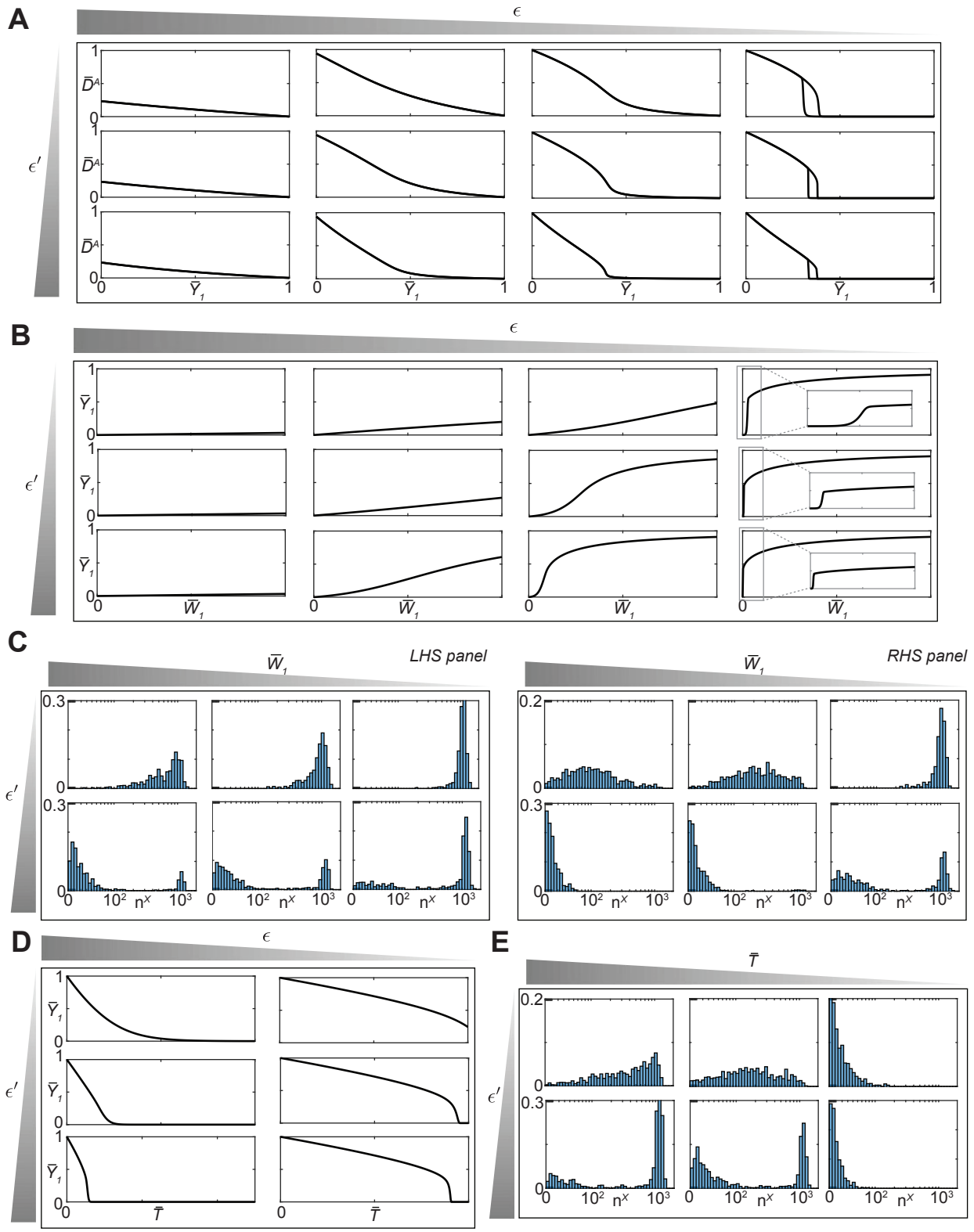

Fig. SM.3. Continued on the following page.

Fig. SM.3. The parameters ε and ε' affect the shape of the probability distribution for gene expression levels. A Input/output steady state characteristics for the $(\bar{Y}_1, \bar{D}^A)$ pair for different values of ε and ε' obtained from simulations of system (SM.11) with $(\bar{Y}_1, \bar{D}_2^R, \bar{D}^A) = (k, 0, 1-k)$ as initial conditions, with $0 \leq k \leq 1$. The parameter values used for these simulations are listed in SI Section S.9. In particular, $\varepsilon = 0.0001, 0.1, 1, 50$ and $\varepsilon' = 1, 5, 25$. **B** dose-response curve for the $(\bar{W}_1, \bar{Y}_1)$ pair for different values of ε and ε' obtained from simulations of system (SM.16) with $(\bar{Y}_1, \bar{D}_2^R, \bar{D}^A) = (0, 0, 1)$ as initial conditions. The parameter values used for these simulations are listed in SI Section S.9. In particular, $\varepsilon = 0.0001, 0.1, 1, 50$ and $\varepsilon' = 1, 5, 25$. **C** Probability distributions of the system represented by reactions listed in SI Tables SM.1 and SM.3 after t = 28 days. The distributions are obtained computationally using SSA [56] and we indicate with n^X the gene expression level (logicle scale). The parameter values used for these simulations are listed in SI Section S.9. In particular, in the left-hand side panel we consider $\varepsilon' = 1.5, 25$, $\bar{W}_1 = [0, 0.7], [0.5, 1.2], [1, 1.7]$ and (n_{12}^R,n_1^R,n_2^R,n^A) = $(0, 0, 0, \mathrm{D_{tot}})$ as initial conditions. The initial values of n^X of n^m at time $t = 0$ were set to their steady states of the ODEs. In the right-hand side panel, we consider $\bar{W}_1 = [0, 0.4], [2.4, 2.8], [3.4, 3.8]$ and all the other parameter values as the ones used for the simulations in the left-hand side panel. For all the simulations we set $\alpha = \bar{\alpha} = 1$, $\varepsilon = 0.13$, $\mu = 0.1$, $b = \beta = 1$, and we consider $\mathrm{D_{tot}} = 15$ and $N = 1000$ samples to realize each distribution. For each simulation, the value of $\bar{W}_1$ was randomly selected from a uniformly distributed range, whose extremes are listed above. **D** Dose-response curve for the $(\bar{Y}_1, \bar{T})$ pair for different values of ε and ε' obtained from simulations of system (SM.16) with $(\bar{Y}_1, \bar{D}_2^R, \bar{D}^A) = (1, 0, 0)$ as initial conditions. The parameter values used for these simulations are listed in SI Section S.9. In particular, $\varepsilon = 0.0001, 0.1$ and $\varepsilon' = 1, 5, 25$. **E** Probability distributions of the system represented by reactions listed in SI Tables SM.1 and SM.3 after t = 28 days. The distributions are obtained computationally using SSA [56] and we indicate with n^X the gene expression level (logicle scale). The parameter values used for these simulations are listed in SI Section S.9. In particular, we consider $\varepsilon' = 1.5, 25$, $\bar{T} = [0, 0.05], [0.24, 0.28], [0.36, 0.4]$ and (n_{12}^R,n_1^R,n_2^R,n^A) = $(\mathrm{D_{tot}}, 0, 0, 0)$ as initial conditions. The initial values of n^X of n^m at time $t = 0$ were set to their steady states of the ODEs. For all the simulations we set $\alpha = \bar{\alpha} = 1$, $\varepsilon = 0.13$, $\mu = 0.1$, $b = \beta = 1$, and we consider $\mathrm{D_{tot}} = 15$ and $N = 1000$ samples to realize each distribution. For each simulation, the value of $\bar{T}$ was randomly selected from a uniformly distributed range, whose extremes are listed above. In our model, ε (ε') is the parameter that scales the ratio between the basal (recruited) erasure rate and the auto-catalysis rate of each modification and $\bar{W}_1$ and $\bar{T}$ represent the normalized amounts of DNMT3A and TET1 at time 0, which exponentially decrease over time.

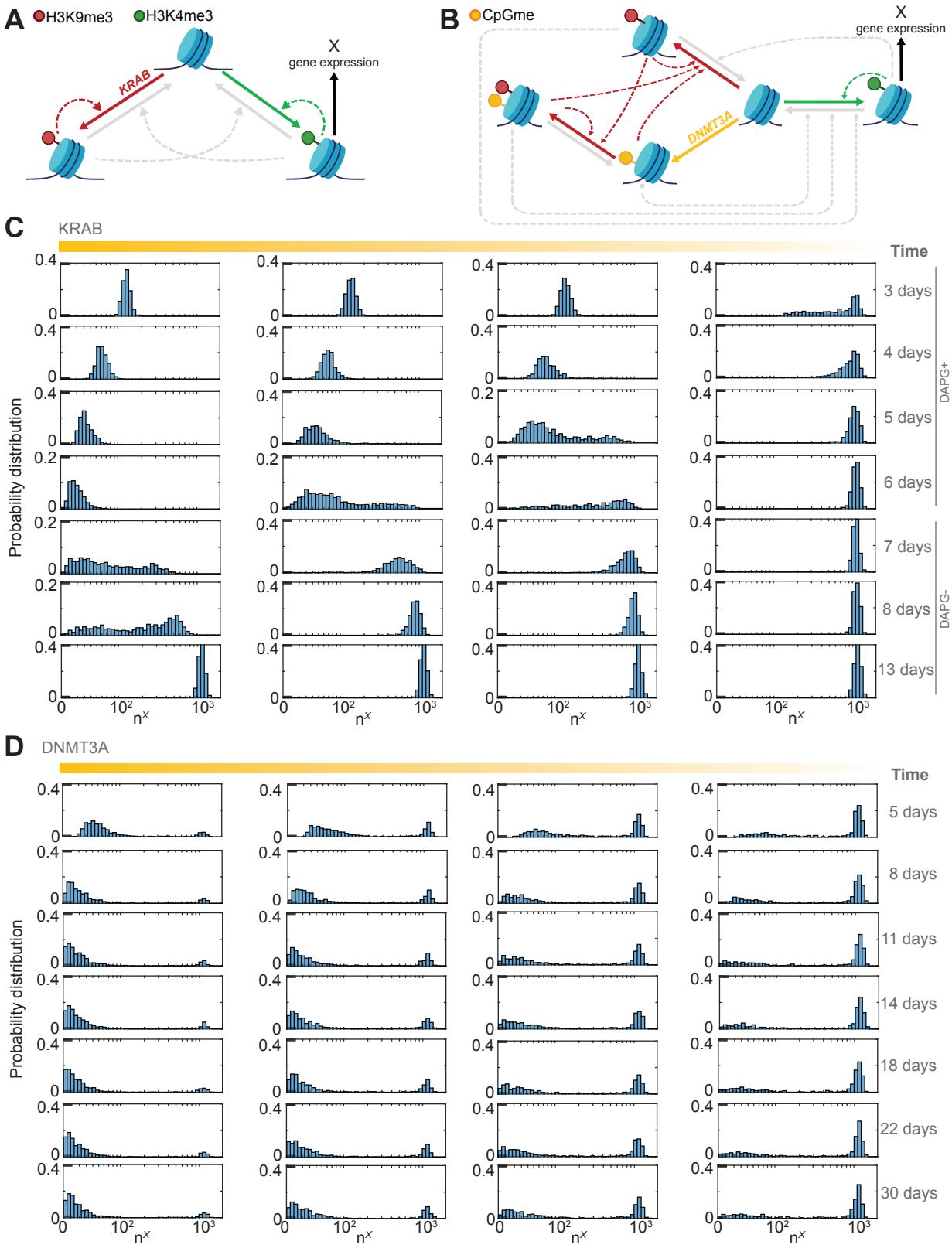

Fig. SM.4. Continued on the following page.

Fig. SM.4. Simulations recapitulating the effect of transient transfection of KRAB and DNMT3A on the gene expression probability distribution. A Diagram of the simplified chromatin modification circuit, including H3K9me3 and H3K4me3 only. We use solid arrows to represent the nucleosome modifications and gene expression. We use dashed arrows to represent the recruitment process and the consequent effect on establishment or erasure. For each arrow, we use red for processes involved in H3K9me3 establishment, green for processes involved in H3K4me3 establishment, gray for processes involved in the erasure of histone modifications, and black for gene expression. **B** Diagram of the chromatin modification circuit including H3K9me3, H3K4me3, and CpGme. We use solid arrows to represent the nucleosome modifications and gene expression. We use dashed arrows to represent the recruitment process and the consequent effect on establishment or erasure. For each arrow, we use red for processes involved in the H3K9me3 establishment, green for processes involved in H3K4me3 establishment, orange for processes involved in DNA methylation establishment, gray for processes involved in the erasure of histone modifications, and black for gene expression. **C** Probability distributions of the system represented in panel A, whose reactions are listed in SI Tables SM.2 and SM.4. The distributions are obtained computationally using SSA [56] and we indicate with n^X the gene expression level (logicle scale). The parameter values used for these simulations are listed in SI Section S.9. In particular, we consider $KRAB = \bar{W}_2 = [1.5, 7.5], [20, 100], [45, 225], [4000, 20000]$, and ($n_2^R$,$n^A$) = $(0, \mathrm{D_{tot}})$ as initial conditions. The initial values of n^X of n^m at time $t = 0$ were set to their steady states of the ODEs. **D** Probability distributions of the system represented in panel B, whose reactions are listed in SI Tables SM.1 and SM.3. The distributions are obtained computationally using SSA [56] and we indicate with n^X the gene expression level (logicle scale). The parameter values used for these simulations are listed in SI Section S.9. In particular, we consider $DNMT3A = \bar{W}_1 = [0.2, 0.7]$, $[0.35, 1.23]$, $[0.6, 2.1]$, $[0.9, 3.1]$, $KRAB = 0$, and (n_{12}^R,n_1^R,n_2^R,n^A) = $(0, 0, 0, \mathrm{D_{tot}})$ as initial conditions. The initial values of n^X of n^m at time $t = 0$ were set to their steady states of the ODEs. For all the simulations we set $\alpha = 1$, $\varepsilon = 0.13$, $\varepsilon' = 25$, $\mu = 0.1$, $b = 1$, we model the dynamics of KRAB and DNMT3A as pulses that exponentially decrease over time, and we consider $\mathrm{D_{tot}} = 15$ and $N = 1000$ samples to realize each distribution. For each simulation, the value of $\bar{W}_1$ (or $\bar{W}_2$) was randomly selected from a uniformly distributed range, whose extremes are listed above.

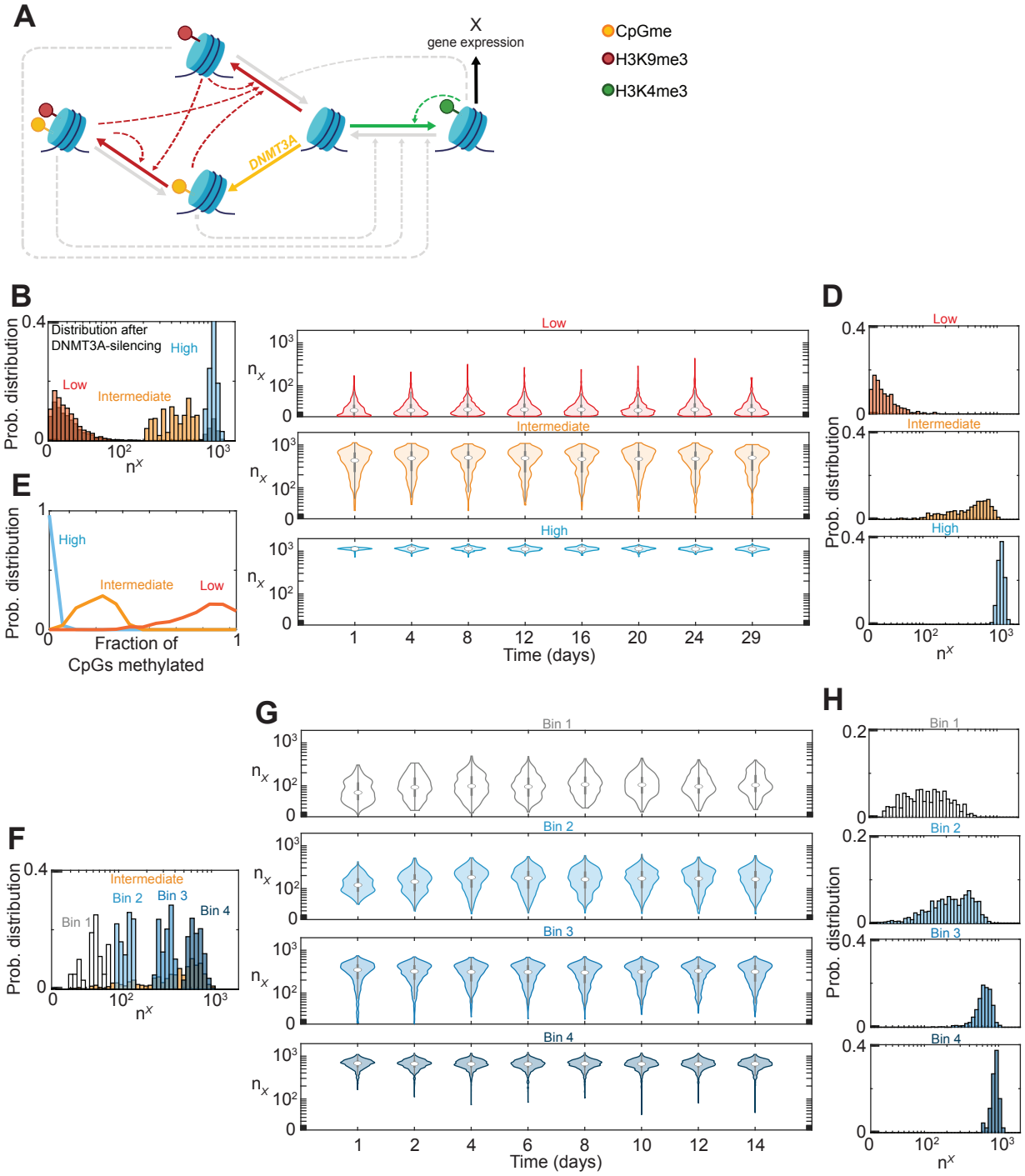

Fig. SM.5. Continued on the following page.

Fig. SM.5. Simulations recapitulating the experimental results shown in Fig. 3, showing that intermediate gene expression levels are stable and exhibit intermediate DNA methylation levels. A Diagram of the chromatin modification circuit including H3K9me3, H3K4me3, and CpGme. We use solid arrows to represent the nucleosome modifications and gene expression. We use dashed arrows to represent the recruitment process and the consequent effect on establishment or erasure. For each arrow, we use red for processes involved in H3K9me3 establishment, green for processes involved in H3K4me3 establishment, orange for processes involved in DNA methylation establishment, gray for processes involved in the erasure of histone modifications, and black for gene expression. **B** Probability distributions of the system represented in panel A, whose reactions are listed in SI Tables SM.1 and SM.3. The distributions are obtained computationally using SSA [56] and we indicate with n^X the gene expression level (logicle scale). The black distribution represents the probability distribution of the system at day 30 after DNMT3A-silencing. The parameter values used for these simulations are listed in SI Section S.9. In particular, we consider $DNMT3A = \bar{W}_1 = [0.6, 2.1]$, $KRAB = 0$, and (n^R_{12},n^R_1,n^R_2,n^A) = $(0, 0, 0, \mathrm{D_{tot}})$ as initial conditions. The initial values of n^X of n^m at time $t = 0$ were set to their steady states of the ODEs. The low (red), intermediate (orange), and high (blue) distributions are obtained by subdividing the black distribution with respect to the following intervals of n^X:[0,100], [200,800], [900,10000]. **C** Probability distributions of the system represented in panel A obtained as described in panel B. The parameter values used for these simulations are listed in SI Section S.9. In particular, for each case, we consider $DNMT3A = 0$, $KRAB = 0$, and, as initial conditions, points from the red, orange, and blue distributions shown in panel B, respectively. **D** Probability distributions of the system at day 29 from panel C. **E** Probability distribution of the fraction of CpGs methylated, i.e., $(n^R_1 + n^R_{12})/\mathrm{D_{tot}}$, at day 29 obtained from the simulations conducted to obtain panel C. **F** Probability distributions of the system represented in panel A, whose reactions are listed in SI Tables SM.1 and SM.3. The distributions are obtained computationally using SSA [56] and we indicate with n^X the gene expression level (logicle scale). The orange distribution is the one obtained and described in panel D. The other ones are obtained by subdividing the orange distribution with respect to the following intervals of n^X: [0,80] (Bin 1), [90,150] (Bin 2), [250,400] Bin 3, [500,10000] (Bin 4). **G** Probability distributions of the system represented in panel A, obtained as described in panel F. The parameter values used for these simulations are listed in SI Section S.9. In particular, for each case, we consider $DNMT3A = 0$, $KRAB = 0$, and, as initial conditions, points from the "Bin 1", "Bin 2", "Bin 3", and "Bin 4" distributions shown in panel F, respectively. **H** Probability distributions of the system at day 14 from panel G.

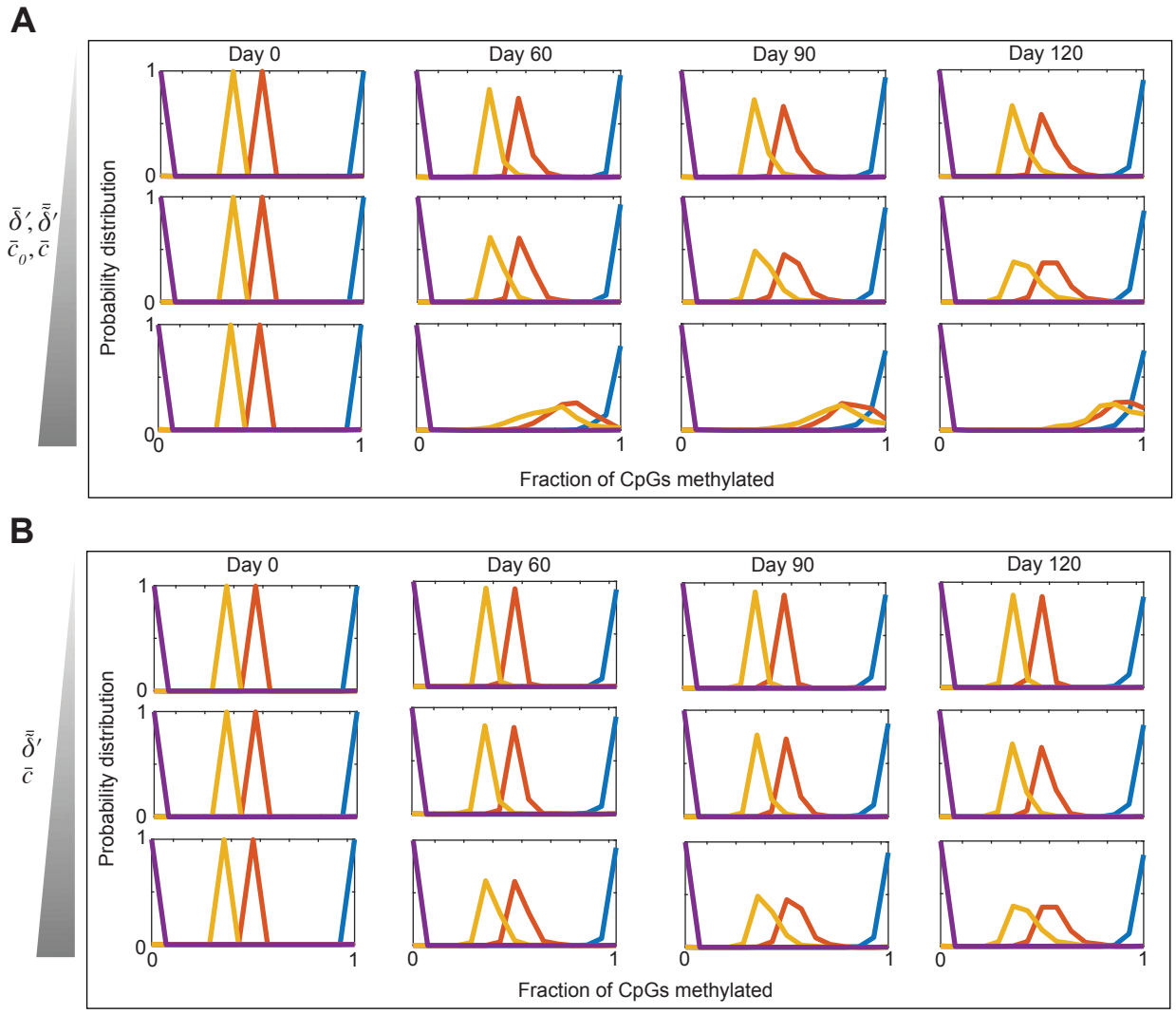

Fig. SM.6. Continued on the following page.

Fig. SM.6. Stochastic analysis of the full chromatin modification circuit model including the refined DNA methylation maintenance model. A Probability distributions of the system represented by reactions listed in SI Tables SM.5 and SM.3. The distributions are obtained computationally using SSA [56] and, on the x we have the fraction of CpGs methylated. In particular, we determine how lower parameter values affect the probability distribution of the system. The parameter values used for these simulations are listed in SI Section S.9. In particular, we consider $\bar{c}_0 = 3.3 \cdot 10^{-6}, 6.6 \cdot 10^{-6}, 6.6 \cdot 10^{-5}$, $\bar{\delta}' = 3.3 \cdot 10^{-6}, 6.6 \cdot 10^{-6}, 6.6 \cdot 10^{-5}$, $\bar{c} = 5 \cdot 10^{-5}, 1 \cdot 10^{-4}, 1 \cdot 10^{-3}$, $\bar{\bar{\delta}}' = 3.3 \cdot 10^{-6}, 6.6 \cdot 10^{-6}, 6.6 \cdot 10^{-5}$, and four initial fractions of CpGs methylated, i.e., (0.93,0.4,0.27,0). Specifically, as initial conditions, we set (n_{12}^R,n_1^R,n_2^R,n^A) = (14,0,0,1) (blue), (n_{12}^R,n_1^R,n_2^R,n^A) = (6,0,0,9) (red), (n_{12}^R,n_1^R,n_2^R,n^A) = (4,0,0,11) (yellow), (n_{12}^R,n_1^R,n_2^R,n^A) = (0,0,0,15) (purple). For each case, The initial values of n^X of n^m at time $t = 0$ were set to their steady states of the ODEs. For all the simulations we set $\alpha = \bar{\alpha} = 1$, $\varepsilon = 0.13$, $\varepsilon' = 25$, $\mu = 0.1$, $b = \beta = 1$. **B** Probability distributions of the system represented by reactions listed in SI Tables SM.5 and SM.3. The distributions are obtained computationally using SSA [56] and, on the x we have the fraction of CpGs methylated. In particular, we determine how $\bar{c}$ and $\bar{\bar{\delta}}'$, i.e., normalized rate constants associated with the reactions representing the effect of DNMT1 recruitment by H3K9me3 on the maintenance process, affect the probability distribution of the system. The parameter values used for these simulations are listed in SI Section S.9. In particular, we consider $\bar{c}_0 = 6.6 \cdot 10^{-6}$, $\bar{\delta}' = 6.6 \cdot 10^{-6}$, $\bar{c} = 3.47 \cdot 10^{-5}$, $3 \cdot 10^{-5}$, $3.47 \cdot 10^{-4}$, $\bar{\bar{\delta}}' = 6.6 \cdot 10^{-7}, 1.94 \cdot 10^{-6}, 6.6 \cdot 10^{-6}$.The values of the other parameters and the initial conditions are the same as those used for panel A. For all simulations, we consider $\mathrm{D_{tot}} = 15$ and we consider $N = 1000$ samples to realize each distribution.

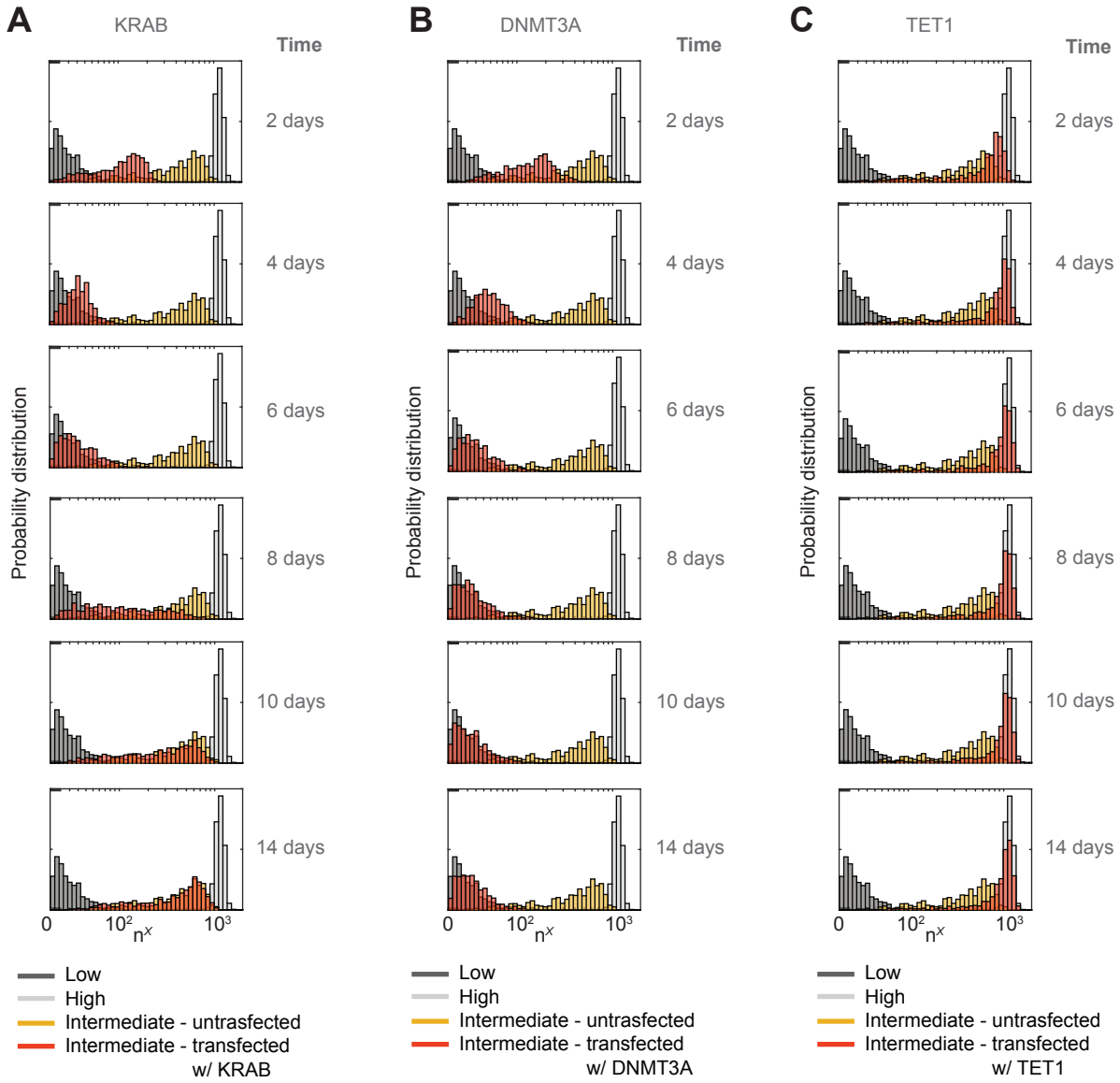

Fig. SM.7. Continued on the following page.

Fig. SM.7. Simulations recapitulating the effect of KRAB, DNMT3A, and TET1 on the gene expression probability distribution, starting from an intermediate level of gene expression. A Probability distributions of the system represented in Fig. SM.4A, whose reactions are listed in SI Tables SM.2 and SM.4. The distributions are obtained computationally using SSA [56] and we indicate with n^X the gene expression level (logicle scale). The parameter values used for these simulations are listed in SI Section S.9. In particular, we consider $KRAB = \bar{W}_2 = [50, 250]$, $DNMT3A = \bar{W}_1 = 0, TET1 = \bar{T} = 0$. As initial conditions, we consider values of (n^R_{12},n^R_1,n^R_2,n^A,n^X,n^m) from the simulations associated with the orange distribution in SI Fig. SM.5D. **B** Probability distributions of the system represented in Fig. SM.4B, whose reactions are listed in SI Tables SM.1 and SM.3. The distributions are obtained computationally using SSA [56]. The parameter values used for these simulations are listed in SI Section S.9. In particular, we consider $DNMT3A = \bar{W}_1 = [0.2, 0.7]$, $KRAB = \bar{W}_2 = 0$, and $TET1 = \bar{T} = 0$. **C** Probability distributions of the system represented in Fig. SM.4B, whose reactions are listed in SI Tables SM.1 and SM.3. The parameter values used for these simulations are listed in SI Section S.9. In particular, we consider $DNMT3A = \bar{W}_1 = 0$, $KRAB = \bar{W}_2 = 0$, and $TET1 = \bar{T} = [0.004, 0.014]$. For all the simulations we set $\alpha = \bar{\alpha} = 1$, $\varepsilon = 0.13$, $\varepsilon' = 25$, $\mu = 0.1$, $b = 1$, we model the dynamics of KRAB, DNMT3A, and TET1 as pulses that exponentially decrease over time, and we consider $\mathrm{D_{tot}} = 15$ and $N = 1000$ samples to realize each distribution. For each simulation, the value of $\bar{W}_1$, $\bar{W}_2$, or $\bar{T}$ was randomly selected from a uniformly distributed range, whose extremes are listed above.

S.9 Values of parameters and rationale for parameter selections used in generating figures in the main paper and SI

In our model, we defined the total number of nucleosomes within a gene of interest as $\mathrm{D_{tot}}$. Assuming approximately one nucleosome per 200 bp [79] and given that the length of our gene is ≈ 3000bp, then in our computational study we set the value of $\mathrm{D_{tot}}$ to 15.

With regard to the effect of dilution due to cell growth, we use a standard approach by modeling it as a first-order decay reaction [80]. The decay rate constant can then be expressed as $\delta = ln(2)/T$, where T corresponds to the cell cycle length. Given that in our experiments we use CHO cells, whose cycle length has been estimated to be $\approx$ 20 hr [32], in the simulations aimed at replicating our experimental data, we set $\delta = 0.035$ (corresponding to $T = 19.8$ h).

Additionally, our mathematical study in SI Section S.4 suggests that our 4D+X model can replicate the experimental data related to the transfection of KRAB and DNMT3A (Fig. 2) only within a parameter regime characterized by small ε and large ε'. The expressions defining these parameters are given in (SM.2). Therefore, we set $k_M^A/\Omega = 0.0347$ h^{-1}, $\bar{k}_E^A = 0.0176$ h^{-1}, and $k_E^A/\Omega = 0.8675$ h^{-1}, since these parameter values, along with the previously listed values of δ and $\mathrm{D_{tot}}$, allow us to be within the desired parameter regime and accurately replicate our experimental results.

Regarding the other parameters, we considered multiple values and selected those that allow us to accurately replicate all experimental results presented in this paper.

S.9.1 Parameter values used to realize the plots in Fig. 2K - top panel

$\alpha = 1$, $\bar{\alpha} = 1$, $\mu = 0.1$, $b = 1$, $\varepsilon = 0.1$, $\varepsilon' = 25$, $u^A = 15$. As initial conditions, we set $(\bar{Y}_1, \bar{D}_2^R, \bar{D}^A) = (k, 0, 1-k)$, with $0 \leq k \leq 1$.

S.9.2 Parameter values used to realize the plots in Fig. 2K - bottom panel

$\tilde{u}_2^R = 0$, $\tilde{\mu}' = 0$, $\beta = 1$, $\tilde{u}_1^R = 1$, $\bar{W}_1 = [0, 4]$ $\alpha = 1$, $\bar{\alpha} = 1$, $\mu = 0.1$, $b = 1$, $\varepsilon = 0.1$, $\varepsilon' = 25$, $u^A = 15$. As initial conditions, we set $(\bar{Y}_1, \bar{D}_2^R, \bar{D}^A) = (0, 0, 1)$.

S.9.3 Parameter values used to realize the plots in Fig. 2L

$k^A_{W0} = 0$, $k^A_W = 7.8075$ h^{-1}, $\bar{k}^A_E = 0.0118$ h^{-1}, $\delta = 0.0291$ h^{-1}, $\frac{k^A_M}{\Omega} = 0.0347$ h^{-1}, $\frac{k^A_E}{\Omega} = 0.8675$ h^{-1}, $k^1_{W0} = 0$, $k^1_W = 0$, $k'_T = 0$, $\delta' = 0$, $\frac{k'_M}{\Omega} = 0$, $\frac{k'^*_T}{\Omega} = 0$, $k^2_{W0} = 0$, $k^2_W = 0$, $\bar{k}^R_E = 0.0012$ h^{-1}, $\frac{k_M}{\Omega} = 0.0347$ h^{-1}, $\frac{\bar{k}_M}{\Omega} = 0.0347$ h^{-1}, $\frac{k^R_E}{\Omega} = 0.0868$ h^{-1}, $\beta_m = 0.2556$ h^{-1}, $\beta^A_m = 0.0021$ h^{-1}, $\beta = 2.52$ h^{-1}, $\gamma_m = 0.24$ h^{-1}. We consider four initial conditions: (n^R_{12},n^R_1,n^R_2,n^A) = (14,0,1,0) (blue), (n^R_{12},n^R_1,n^R_2,n^A) = (6,0,8,1) (red), (n^R_{12},n^R_1,n^R_2,n^A) = (4,0,5,6) (yellow), (n^R_{12},n^R_1,n^R_2,n^A) = (1,0,1,13) (purple). For each case, the initial values of n^X of n^m at time $t = 0$ were set to their steady states of the ODEs.

S.9.4 Parameter values used to realize the plots in Fig. 2M

$k^A_{W0} = 0$, $k^A_W = 7.8075$ h^{-1}, $\bar{k}^A_E = 0.0315$ h^{-1}, $\delta = 0.035$ h^{-1}, $\frac{k^A_M}{\Omega} = 0.0347$ h^{-1}, $\frac{k^A_E}{\Omega} = 0.8675$ h^{-1}, $k^1_{W0} = 0$, $k^1_W \in [0, 0.3643]e^{-\delta t}, [0.2602, 0.6246]e^{-\delta t}, [0.5205, 0.8848]e^{-\delta t}$ h^{-1}, $k'_T = 0$, $\delta' = 0$, $\frac{k'_M}{\Omega} = 0$, $\frac{k'^*_T}{\Omega} = 0$, $k^2_{W0} = 0$, $k^2_W = 0$, $\bar{k}^R_E = 0.0032$ h^{-1}, $\frac{k_M}{\Omega} = 0.0347$ h^{-1}, $\frac{\bar{k}_M}{\Omega} = 0.0347$ h^{-1}, $\frac{k^R_E}{\Omega} = 0.0868$ h^{-1}, $\beta_m = 0.2556$ h^{-1}, $\beta^A_m = 0.0021$ h^{-1}, $\beta = 2.52$ h^{-1}, $\gamma_m = 0.24$ h^{-1}. As initial condition, we consider (n^R_{12},n^R_1,n^R_2,n^A) = (0,0,0,15) and the initial values of n^X of n^m at time $t = 0$ were set to their steady states of the ODEs.

S.9.5 Parameter values used to realize the plots in Fig. 4G and I

$k^A_{W0} = 0$, $k^A_W = 7.8075$ h^{-1}, $\bar{k}^A_E = 0.0176$ h^{-1}, $\delta = 0.035$ h^{-1}, $\frac{k^A_M}{\Omega} = 0.0347$ h^{-1}, $\frac{k^A_E}{\Omega} = 0.8675$ h^{-1}, $k^1_{W0} = 0$, $k^1_W = 0$, $c = 1.11 \cdot 10^{-6}$ h^{-1}, $c_0 = 8.37 \cdot 10^{-5}$ h^{-1}, $\delta' = 2.09 \cdot 10^{-5}$ h^{-1}, $\tilde{\delta}' = 4.15 \cdot 10^{-5}$ h^{-1}, $K = 1$, $\frac{k'_M}{\Omega} = 0$, $\frac{k'^*_T}{\Omega} =$ h^{-1}, $k^2_{W0} = 0$, $k^2_W = 0$, $\bar{k}^R_E = 0.0018$ h^{-1}, $\frac{k_M}{\Omega} = 0.0347$ h^{-1}, $\frac{\bar{k}_M}{\Omega} = 0.0347$ h^{-1}, $\frac{k^R_E}{\Omega} = 0.0868$ h^{-1}, $\beta_m = 0.2556$ h^{-1}, $\beta^A_m = 0.0021$ h^{-1}, $\beta = 2.52$ h^{-1}, $\gamma_m = 0.24$ h^{-1}. We consider eight initial conditions: (n^R_{12},n^R_1,n^R_2,n^A) = (13,0,0,2) (Bin 1), (12,0,0,3) (Bin 2), (8,0,0,7) (Bin 3), (6,0,0,9) (Bin 4), (5,0,0,10) (Bin 5), (4,0,0,11) (Bin 6), (1,0,0,14) (Bin 7), (0,0,0,15) (Bin 8). For each case, the initial values of n^X of n^m at time $t = 0$ were set to their steady states of the ODEs.

S.9.6 Parameter values used to realize the plots in SI Fig. SM.1B

$k^A_{W0} = 0$, $k^A_W = 7.8075$ h^{-1}, $\bar{k}^A_E = 0.0118$ h^{-1}, $\delta = 0.0291$ h^{-1}, $\frac{k^A_M}{\Omega} = 0.0347$ h^{-1}, $\frac{k^A_E}{\Omega} = 0.8675$ h^{-1}, $k^1_{W0} = 0$, $k^1_W = 0$, $k'_T = 0$, $\delta' = 0$, $\frac{k'_M}{\Omega} = 0, 0.00347$ h^{-1}, $\frac{k'^*_T}{\Omega} = 0$, $k^2_{W0} = 0$, $k^2_W = 0$, $\bar{k}^R_E = 0.0012$ h^{-1}, $\frac{k_M}{\Omega} = 0.0347$ h^{-1}, $\frac{\bar{k}_M}{\Omega} = 0.0347$ h^{-1}, $\frac{k^R_E}{\Omega} = 0.0868$ h^{-1}, $\beta_m = 0.2556$ h^{-1}, $\beta^A_m = 0.0021$ h^{-1}, $\beta = 2.52$ h^{-1}, $\gamma_m = 0.24$ h^{-1}. We consider four initial conditions: (n^R_{12},n^R_1,n^R_2,n^A) = (14,0,1,0) (blue), (n^R_{12},n^R_1,n^R_2,n^A) = (6,0,8,1) (red),

(n_{12}^R,n_1^R,n_2^R,n^A) = (4,0,5,6) (yellow), (n_{12}^R,n_1^R,n_2^R,n^A) = (1,0,1,13) (purple). For each case, the initial values of n^X of n^m at time $t = 0$ were set to their steady states of the ODEs.

S.9.7 Parameter values used to realize the plots in SI Fig. SM.1D - left hand-side panel

$\alpha = 1$, $\bar{\alpha} = 1$, $\mu = 0.1$, $b = 1$, $\varepsilon = 0.1$, $\varepsilon' = 1,25$, $u^A = 15$. As initial conditions, we set $(\bar{Y}_1, \bar{D}_2^R, \bar{D}^A) = (k, 0, 1-k)$, with $0 \leq k \leq 1$.

S.9.8 Parameter values used to realize the plots in SI Fig. SM.1D - right hand-side panel

$\tilde{u}_2^R = 0$, $\tilde{\mu}' = 0$, $\beta = 1$, $\tilde{u}_1^R = 1$, $\bar{W}_1 = [0, 4]$ $\alpha = 1$, $\bar{\alpha} = 1$, $\mu = 0.1$, $b = 1$, $\varepsilon = 0.1$, $\varepsilon' = 1,25$, $u^A = 15$. As initial conditions, we set $(\bar{Y}_1, \bar{D}_2^R, \bar{D}^A) = (0, 0, 1)$.

S.9.9 Parameter values used to realize the plots in SI Fig. SM.1E

$k_{W0}^A = 0$, $k_W^A = 7.8075$ h^{-1}, $\bar{k}_E^A = 0.0315$ h^{-1}, $\delta = 0.035$ h^{-1}, $\frac{k_M^A}{\Omega} = 0.0347$ h^{-1}, $\frac{k_E^A}{\Omega} = 0.0520, 0.8675$ h^{-1}, $k_{W0}^1 = 0$, $k_W^1 \in [0, 0.3643]e^{-\delta t}, [0.2602, 0.6246]e^{-\delta t}, [0.5205, 0.8848]e^{-\delta t}$ h^{-1}, $k_T' = 0$, $\delta' = 0$, $\frac{k_M'}{\Omega} = 0$, $\frac{k_T'^*}{\Omega} = 0$, $k_{W0}^2 = 0$, $k_W^2 = 0$, $\bar{k}_E^R = 0.0032$ h^{-1}, $\frac{k_M}{\Omega} = 0.0347$ h^{-1}, $\frac{\bar{k}_M}{\Omega} = 0.0347$ h^{-1}, $\frac{k_E^R}{\Omega} = 0.0052, 0.0868$ h^{-1}, $\beta_m = 0.2556$ h^{-1}, $\beta_m^A = 0.0021$ h^{-1}, $\beta = 2.52$ h^{-1}, $\gamma_m = 0.24$ h^{-1}. As initial condition, we consider (n_{12}^R,n_1^R,n_2^R,n^A) = (0,0,0,15) and the initial values of n^X of n^m at time $t = 0$ were set to their steady states of the ODEs.

S.9.10 Parameter values used to realize the plots in SI Fig. SM.2

$k_{W0}^A = 0$, $k_W^A = 7.8075$ h^{-1}, $\bar{k}_E^A = 0.0118$ h^{-1}, $\delta = 0.0291$ h^{-1}, $\frac{k_M^A}{\Omega} = 0.0347$ h^{-1}, $\frac{k_E^A}{\Omega} = 0.8675$ h^{-1}, $k_{W0}^1 = 0$, $k_W^1 = 0$, $k_T' = 0, 0.00012, 0.0012$ h^{-1}, $\delta' = 0$, $\frac{k_M'}{\Omega} = 0, 3.47 \cdot 10^{-4}, 3.47 \cdot 10^{-3}$ h^{-1}, $\frac{k_T'^*}{\Omega} = 0, 0.0087, 0.087$ h^{-1}, $k_{W0}^2 = 0$, $k_W^2 = 0$, $\bar{k}_E^R = 0.0012$ h^{-1}, $\frac{k_M}{\Omega} = 0.0347$ h^{-1}, $\frac{\bar{k}_M}{\Omega} = 0.0347$ h^{-1}, $\frac{k_E^R}{\Omega} = 0.0868$ h^{-1}, $\beta_m = 0.2556$ h^{-1}, $\beta_m^A = 0.0021$ h^{-1}, $\beta = 2.52$ h^{-1}, $\gamma_m = 0.24$ h^{-1}. We consider four initial conditions: (n_{12}^R,n_1^R,n_2^R,n^A) = (14,0,1,0) (blue), (n_{12}^R,n_1^R,n_2^R,n^A) = (6,0,8,1) (red), (n_{12}^R,n_1^R,n_2^R,n^A) = (4,0,5,6) (yellow), (n_{12}^R,n_1^R,n_2^R,n^A) = (1,0,1,13) (purple). For each case, the initial values of n^X of n^m at time $t = 0$ were set to their steady states of the ODEs.

S.9.11 Parameter values used to realize the plots in SI Fig. SM.3A

$\alpha = 1$, $\bar{\alpha} = 1$, $\mu = 0.1$, $b = 1$, $\varepsilon = 0.0001, 0.1, 1, 50$, $\varepsilon' = 1, 5, 25$, $u^A = 15$. As initial conditions, we set $(\bar{Y}_1, \bar{D}_2^R, \bar{D}^A) = (k, 0, 1-k)$, with $0 \leq k \leq 1$.

S.9.12 Parameter values used to realize the plots in SI Fig. SM.3B

$\tilde{u}_2^R = 0$, $\tilde{\mu}' = 0$, $\beta = 1$, $\tilde{u}_1^R = 1$, $\bar{W}_1 = [0, 4]$ $\alpha = 1$, $\bar{\alpha} = 1$, $\mu = 0.1$, $b = 1$, $\varepsilon = 0.0001, 0.1, 1, 50$, $\varepsilon' = 1, 5, 25$, $u^A = 15$. As initial conditions, we set $(\bar{Y}_1, \bar{D}_2^R, \bar{D}^A) = (0, 0, 1)$.

S.9.13 Parameter values used to realize the plots in SI Fig. SM.3C

$k_{W0}^A = 0$, $k_W^A = 7.8075$ h^{-1}, $\bar{k}_E^A = 0.0315$ h^{-1}, $\delta = 0.035$ h^{-1}, $\frac{k_M^A}{\Omega} = 0.0347$ h^{-1}, $\frac{k_E^A}{\Omega} = 0.0520, 0.8675$ h^{-1}, $k_{W0}^1 = 0$, $k_W^1 \in [0, 0.3643]e^{-\delta t}, [0.2602, 0.6246]e^{-\delta t}, [0.5205, 0.8848]e^{-\delta t}$ h^{-1} (left hand-side panel) and $k_W^1 \in [0, 0.2082]e^{-\delta t}, [1.2492, 1.4574]e^{-\delta t}, [1.7697, 1.9779]e^{-\delta t}$ h^{-1} (right hand-side panel), $k_T' = 0$, $\delta' = 0$, $\frac{k_M'}{\Omega} = 0$, $\frac{k_T'^*}{\Omega} = 0$, $k_{W0}^2 = 0$, $k_W^2 = 0$, $\bar{k}_E^R = 0.0032$ h^{-1}, $\frac{k_M}{\Omega} = 0.0347$ h^{-1}, $\frac{\bar{k}_M}{\Omega} = 0.0347$ h^{-1}, $\frac{k_E^R}{\Omega} = 0.0052, 0.0868$ h^{-1}, $\beta_m = 0.2556$ h^{-1}, $\beta_m^A = 0.0021$ h^{-1}, $\beta = 2.52$ h^{-1}, $\gamma_m = 0.24$ h^{-1}. As initial condition, we consider (n_{12}^R,n_1^R,n_2^R,n^A) = (0,0,0,15) and the initial values of n^X of n^m at time $t = 0$ were set to their steady states of the ODEs.

S.9.14 Parameter values used to realize the plots in SI Fig. SM.3D

$\tilde{u}_2^R = 0$, $\tilde{\mu}' = 1$, $\beta = 1$, $\tilde{u}_1^R = 0$, $\bar{T} = [0, 4]$ $\alpha = 1$, $\bar{\alpha} = 1$, $\mu = 0.1$, $b = 1$, $\varepsilon = 0.0001, 0.1, 1, 50$, $\varepsilon' = 1, 5, 25$, $u^A = 15$. As initial conditions, we set $(\bar{Y}_1, \bar{D}_2^R, \bar{D}^A) = (1, 0, 0)$.

S.9.15 Parameter values used to realize the plots in SI Fig. SM.3E

$k_{W0}^A = 0$, $k_W^A = 7.8075$ h^{-1}, $\bar{k}_E^A = 0.0315$ h^{-1}, $\delta = 0.035$ h^{-1}, $\frac{k_M^A}{\Omega} = 0.0347$ h^{-1}, $\frac{k_E^A}{\Omega} = 0.0520, 0.8675$ h^{-1}, $k_{W0}^1 = 0$, $k_W^1 = 0$, $k_T' \in [0, 0.0016]e^{-\delta t}, [0.0076, 0.0088]e^{-\delta t}, [0.0113, 0.0126]e^{-\delta t}$ h^{-1}, $\delta' = 0$, $\frac{k_M'}{\Omega} = 0$, $\frac{k_T'^*}{\Omega} \in [0, 0.0434]e^{-\delta t}, [0.2082, 0.2429]e^{-\delta t}, [0.3123, 0.3470]e^{-\delta t}$ h^{-1}, $k_{W0}^2 = 0$, $k_W^2 = 0$, $\bar{k}_E^R = 0.0032$ h^{-1}, $\frac{k_M}{\Omega} = 0.0347$ h^{-1}, $\frac{\bar{k}_M}{\Omega} = 0.0347$ h^{-1}, $\frac{k_E^R}{\Omega} = 0.0052, 0.0868$ h^{-1}, $\beta_m = 0.2556$ h^{-1}, $\beta_m^A = 0.0021$ h^{-1}, $\beta = 2.52$ h^{-1}, $\gamma_m = 0.24$ h^{-1}. As initial condition, we consider (n_{12}^R,n_1^R,n_2^R,n^A) = (15,0,0,0) and the initial values of n^X of n^m at time $t = 0$ were set to their steady states of the ODEs.

S.9.16 Parameter values used to realize the plots in SI Fig. SM.4C

$k^A_{W0} = 0$, $k^A_W = 7.8075$ h^{-1}, $\bar{k}^A_E = 0.0176$ h^{-1}, $\delta = 0.035$ h^{-1}, $\frac{k^A_M}{\Omega} = 0.0347$ h^{-1}, $\frac{k^A_E}{\Omega} = 0.8675$ h^{-1}, $k^2_{W0} = 0$, $k^2_W \in [0.78, 3.90]e^{-\delta t}, [10.41, 52.05]e^{-\delta t}, [23.42, 117.11]e^{-\delta t}, [2082, 10410]e^{-\delta t}$ h^{-1}, $\bar{k}^R_E = 0.0018$ h^{-1}, $\frac{k_M}{\Omega} = 0.0347$ h^{-1}, $\frac{\bar{k}_M}{\Omega} = 0.0347$ h^{-1}, $\frac{k^R_E}{\Omega} = 0.0868$ h^{-1}, $\beta_m = 0.2556$ h^{-1}, $\beta^A_m = 0.0021$ h^{-1}, $\beta = 2.52$ h^{-1}, $\gamma_m = 0.24$ h^{-1}. As initial condition, we consider (n^R_2,n^A) = (0,15) and the initial values of n^X of n^m at time $t = 0$ were set to their steady states of the ODEs.

S.9.17 Parameter values used to realize the plots in SI Fig. SM.4D

$k^A_{W0} = 0$, $k^A_W = 7.8075$ h^{-1}, $\bar{k}^A_E = 0.0176$ h^{-1}, $\delta = 0.035$ h^{-1}, $\frac{k^A_M}{\Omega} = 0.0347$ h^{-1}, $\frac{k^A_E}{\Omega} = 0.8675$ h^{-1}, $k^1_{W0} = 0$, $k^1_W \in [0.10, 0.36]e^{-\delta t}, [0.18, 0.64]e^{-\delta t}, [0.31, 1.09]e^{-\delta t}, [0.47, 1.61]e^{-\delta t}$ h^{-1}, $k'_T = 0$, $\delta' = 0$, $\frac{k'_M}{\Omega} = 0$, $\frac{k'^*_T}{\Omega} = 0$, $k^2_{W0} = 0$, $k^2_W = 0$ $\bar{k}^R_E = 0.0018$ h^{-1}, $\frac{k_M}{\Omega} = 0.0347$ h^{-1}, $\frac{\bar{k}_M}{\Omega} = 0.0347$ h^{-1}, $\frac{k^R_E}{\Omega} = 0.0868$ h^{-1}, $\beta_m = 0.2556$ h^{-1}, $\beta^A_m = 0.0021$ h^{-1}, $\beta = 2.52$ h^{-1}, $\gamma_m = 0.24$ h^{-1}. As initial condition, we consider (n^R_{12},n^R_1,n^R_2,n^A) = (0,0,0,15) and the initial values of n^X of n^m at time $t = 0$ were set to their steady states of the ODEs.

S.9.18 Parameter values used to realize the plots in SI Fig. SM.5B

$k^A_{W0} = 0$, $k^A_W = 7.8075$ h^{-1}, $\bar{k}^A_E = 0.0176$ h^{-1}, $\delta = 0.035$ h^{-1}, $\frac{k^A_M}{\Omega} = 0.0347$ h^{-1}, $\frac{k^A_E}{\Omega} = 0.8675$ h^{-1}, $k^1_{W0} = 0$, $k^1_W \in [0.31, 1.09]e^{-\delta t}$ h^{-1}, $k'_T = 0$, $\delta' = 0$, $\frac{k'_M}{\Omega} = 0$, $\frac{k'^*_T}{\Omega} = 0$, $k^2_{W0} = 0$, $k^2_W = 0$ $\bar{k}^R_E = 0.0018$ h^{-1}, $\frac{k_M}{\Omega} = 0.0347$ h^{-1}, $\frac{\bar{k}_M}{\Omega} = 0.0347$ h^{-1}, $\frac{k^R_E}{\Omega} = 0.0868$ h^{-1}, $\beta_m = 0.2556$ h^{-1}, $\beta^A_m = 0.0021$ h^{-1}, $\beta = 2.52$ h^{-1}, $\gamma_m = 0.24$ h^{-1}. As initial condition, we consider (n^R_{12},n^R_1,n^R_2,n^A) = (0,0,0,15) and the initial values of n^X of n^m at time $t = 0$ were set to their steady states of the ODEs. The distribution shown is after 30 days.

S.9.19 Parameter values used to realize the plots in SI Fig. SM.5C

$k^A_{W0} = 0$, $k^A_W = 7.8075$ h^{-1}, $\bar{k}^A_E = 0.0176$ h^{-1}, $\delta = 0.035$ h^{-1}, $\frac{k^A_M}{\Omega} = 0.0347$ h^{-1}, $\frac{k^A_E}{\Omega} = 0.8675$ h^{-1}, $k^1_{W0} = 0$, $k^1_W 0$, $k'_T = 0$, $\delta' = 0$, $\frac{k'_M}{\Omega} = 0$, $\frac{k'^*_T}{\Omega} = 0$, $k^2_{W0} = 0$, $k^2_W = 0$ $\bar{k}^R_E = 0.0018$ h^{-1}, $\frac{k_M}{\Omega} = 0.0347$ h^{-1}, $\frac{\bar{k}_M}{\Omega} = 0.0347$ h^{-1}, $\frac{k^R_E}{\Omega} = 0.0868$ h^{-1}, $\beta_m = 0.2556$ h^{-1}, $\beta^A_m = 0.0021$ h^{-1}, $\beta = 2.52$ h^{-1}, $\gamma_m = 0.24$ h^{-1}. As initial condition, we consider values of (n^R_{12},n^R_1,n^R_2,n^A,n^X,n^m) from the simulations shown in SI Fig. SM.5B and divide them with respect to their value of n^X, following the following intervals: $[0, 100]$ (red), $[200, 800]$ (orange), $[900, 10000]$ (blue).

S.9.20 Parameter values used to realize the plots in SI Fig. SM.5G

$k^A_{W0} = 0$, $k^A_W = 7.8075$ h^{-1}, $\bar{k}^A_E = 0.0176$ h^{-1}, $\delta = 0.035$ h^{-1}, $\frac{k^A_M}{\Omega} = 0.0347$ h^{-1}, $\frac{k^A_E}{\Omega} = 0.8675$ h^{-1}, $k^1_{W0} = 0$, $k^1_W 0$, $k'_T = 0$, $\delta' = 0$, $\frac{k'_M}{\Omega} = 0$, $\frac{k'^*_T}{\Omega} = 0$, $k^2_{W0} = 0$, $k^2_W = 0$ $\bar{k}^R_E = 0.0018$ h^{-1}, $\frac{k_M}{\Omega} = 0.0347$ h^{-1}, $\frac{\bar{k}_M}{\Omega} = 0.0347$ h^{-1}, $\frac{k^R_E}{\Omega} = 0.0868$ h^{-1}, $\beta_m = 0.2556$ h^{-1}, $\beta^A_m = 0.0021$ h^{-1}, $\beta = 2.52$ h^{-1}, $\gamma_m = 0.24$ h^{-1}. As initial condition, we consider values of (n^R_{12},n^R_1,n^R_2,n^A,n^X,n^m) from the simulations associated with the orange distribution in SI Fig. SM.5D and divide them with respect to their value of n^X, following the following intervals: $[0, 80]$ (Bin 1), $[90, 150]$ (Bin 2), $[250, 400]$ Bin 3, $[500, 10000]$ (Bin 4).

S.9.21 Parameter values used to realize the plots in SI Fig. SM.6A

$k^A_{W0} = 0$, $k^A_W = 7.8075$ h^{-1}, $\bar{k}^A_E = 0.0176$ h^{-1}, $\delta = 0.035$ h^{-1}, $\frac{k^A_M}{\Omega} = 0.0347$ h^{-1}, $\frac{k^A_E}{\Omega} = 0.8675$ h^{-1}, $k^1_{W0} = 0$, $k^1_W = 0$, $c = 1.74 \cdot 10^{-6}$, $3.47 \cdot 10^{-6}$, $3.47 \cdot 10^{-5}$ h^{-1}, $c_0 = 1.74 \cdot 10^{-6}$, $3.47 \cdot 10^{-6}$, $3.47 \cdot 10^{-5}$ h^{-1}, $\delta' = 1.74 \cdot 10^{-6}$, $3.47 \cdot 10^{-6}$, $3.47 \cdot 10^{-5}$ h^{-1}, $\tilde{\delta}' = 1.74 \cdot 10^{-6}$, $3.47 \cdot 10^{-6}$, $3.47 \cdot 10^{-5}$ h^{-1}, $K = 1$, $\frac{k'_M}{\Omega} = 0$, $\frac{k'^*_T}{\Omega} =$ h^{-1}, $k^2_{W0} = 0$, $k^2_W = 0$, $\bar{k}^R_E = 0.0018$ h^{-1}, $\frac{k_M}{\Omega} = 0.0347$ h^{-1}, $\frac{\bar{k}_M}{\Omega} = 0.0347$ h^{-1}, $\frac{k^R_E}{\Omega} = 0.0868$ h^{-1}, $\beta_m = 0.2556$ h^{-1}, $\beta^A_m = 0.0021$ h^{-1}, $\beta = 2.52$ h^{-1}, $\gamma_m = 0.24$ h^{-1}. We consider four initial conditions: (n^R_{12},n^R_1,n^R_2,n^A) = (14,0,0,1) (blue), (n^R_{12},n^R_1,n^R_2,n^A) = (6,0,0,9) (red), (n^R_{12},n^R_1,n^R_2,n^A) = (4,0,0,11) (yellow), (n^R_{12},n^R_1,n^R_2,n^A) = (0,0,0,15) (purple). For each case, the initial values of n^X of n^m at time $t = 0$ were set to their steady states.

S.9.22 Parameter values used to realize the plots in SI Fig. SM.6B

$k^A_{W0} = 0$, $k^A_W = 7.8075$ h^{-1}, $\bar{k}^A_E = 0.0176$ h^{-1}, $\delta = 0.035$ h^{-1}, $\frac{k^A_M}{\Omega} = 0.0347$ h^{-1}, $\frac{k^A_E}{\Omega} = 0.8675$ h^{-1}, $k^1_{W0} = 0$, $k^1_W = 0$, $c = 3.47 \cdot 10^{-7}$, $1.04 \cdot 10^{-6}$, $3.47 \cdot 10^{-6}$ h^{-1}, $c_0 = 3.47 \cdot 10^{-6}$ h^{-1}, $\delta' = 3.47 \cdot 10^{-6}$ h^{-1}, $\tilde{\delta}' = 3.47 \cdot 10^{-7}$, $1.04 \cdot 10^{-6}$, $3.47 \cdot 10^{-6}$ h^{-1}, $K = 1$, $\frac{k'_M}{\Omega} = 0$, $\frac{k'^*_T}{\Omega} =$ h^{-1}, $k^2_{W0} = 0$, $k^2_W = 0$, $\bar{k}^R_E = 0.0018$ h^{-1}, $\frac{k_M}{\Omega} = 0.0347$ h^{-1}, $\frac{\bar{k}_M}{\Omega} = 0.0347$ h^{-1}, $\frac{k^R_E}{\Omega} = 0.0868$ h^{-1}, $\beta_m = 0.2556$ h^{-1}, $\beta^A_m = 0.0021$ h^{-1}, $\beta = 2.52$ h^{-1}, $\gamma_m = 0.24$ h^{-1}. We consider four initial conditions: (n^R_{12},n^R_1,n^R_2,n^A) = (14,0,0,1) (blue), (n^R_{12},n^R_1,n^R_2,n^A) = (6,0,0,9) (red), (n^R_{12},n^R_1,n^R_2,n^A) = (4,0,0,11) (yellow), (n^R_{12},n^R_1,n^R_2,n^A) = (0,0,0,15) (purple). For each case, the initial values of n^X of n^m at time $t = 0$ were set to their steady states of the ODEs.

S.9.23 Parameter values used to realize the plots in SI Fig. SM.7A

$k^A_{W0} = 0$, $k^A_W = 7.8075$ h^{-1}, $\bar{k}^A_E = 0.0176$ h^{-1}, $\delta = 0.035$ h^{-1}, $\frac{k^A_M}{\Omega} = 0.0347$ h^{-1}, $\frac{k^A_E}{\Omega} = 0.8675$ h^{-1}, $k^1_{W0} = 0$, $k^1_W = 0$, $k'_T = 0$, $\delta' = 0$, $\frac{k'_M}{\Omega} = 0$, $\frac{k'^*_T}{\Omega} = 0$, $k^2_{W0} = 0$, $k^2_W \in [26.02130.13]e^{-\delta t}$ h^{-1}, $\bar{k}^R_E = 0.0018$

h^{-1}, $\frac{k_M}{\Omega} = 0.0347$ h^{-1}, $\frac{\bar{k}_M}{\Omega} = 0.0347$ h^{-1}, $\frac{k_E^R}{\Omega} = 0.0868$ h^{-1}, $\beta_m = 0.2556$ h^{-1}, $\beta_m^A = 0.0021$ h^{-1}, $\beta = 2.52$ h^{-1}, $\gamma_m = 0.24$ h^{-1}. As initial condition, we consider values of (n_{12}^R,n_1^R,n_2^R,n^A,n^X,n^m) from the simulations associated with the orange distribution in SI Fig. SM.5C.

S.9.24 Parameter values used to realize the plots in SI Fig. SM.7B

$k_{W0}^A = 0$, $k_W^A = 7.8075$ h^{-1}, $\bar{k}_E^A = 0.0176$ h^{-1}, $\delta = 0.035$ h^{-1}, $\frac{k_M^A}{\Omega} = 0.0347$ h^{-1}, $\frac{k_E^A}{\Omega} = 0.8675$ h^{-1}, $k_{W0}^1 = 0$, $k_W^1 \in [0.1041, 0.36]e^{-\delta t}$ h^{-1}, $k_T' = 0$, $\delta' = 0$, $\frac{k_M'}{\Omega} = 0$, $\frac{k_T'^*}{\Omega} = 0$, $k_{W0}^2 = 0$, $k_W^2 = 0$, $\bar{k}_E^R = 0.0018$ h^{-1}, $\frac{k_M}{\Omega} = 0.0347$ h^{-1}, $\frac{\bar{k}_M}{\Omega} = 0.0347$ h^{-1}, $\frac{k_E^R}{\Omega} = 0.0868$ h^{-1}, $\beta_m = 0.2556$ h^{-1}, $\beta_m^A = 0.0021$ h^{-1}, $\beta = 2.52$ h^{-1}, $\gamma_m = 0.24$ h^{-1}. As initial condition, we consider values of (n_{12}^R,n_1^R,n_2^R,n^A,n^X,n^m) from the simulations associated with the orange distribution in SI Fig. SM.5C.

S.9.25 Parameter values used to realize the plots in SI Fig. SM.7C

$k_{W0}^A = 0$, $k_W^A = 7.8075$ h^{-1}, $\bar{k}_E^A = 0.0176$ h^{-1}, $\delta = 0.035$ h^{-1}, $\frac{k_M^A}{\Omega} = 0.0347$ h^{-1}, $\frac{k_E^A}{\Omega} = 0.8675$ h^{-1}, $k_{W0}^1 = 0$, $k_W^1 = 0$, $k_T' \in [0.7 \cdot 10^{-4}, 0.24 \cdot 10^{-3}]e^{-\delta t}$ h^{-1}, $\delta' = 0$, $\frac{k_M'}{\Omega} = 0$, $\frac{k_T'^*}{\Omega} in[3.5 \cdot 10^{-3}, 1.2 \cdot 10^{-2}]e^{-\delta t}$ h^{-1}, $k_{W0}^2 = 0$, $k_W^2 = 0$, $\bar{k}_E^R = 0.0018$ h^{-1}, $\frac{k_M}{\Omega} = 0.0347$ h^{-1}, $\frac{\bar{k}_M}{\Omega} = 0.0347$ h^{-1}, $\frac{k_E^R}{\Omega} = 0.0868$ h^{-1}, $\beta_m = 0.2556$ h^{-1}, $\beta_m^A = 0.0021$ h^{-1}, $\beta = 2.52$ h^{-1}, $\gamma_m = 0.24$ h^{-1}. As initial condition, we consider values of (n_{12}^R,n_1^R,n_2^R,n^A,n^X,n^m) from the simulations associated with the orange distribution in SI Fig. SM.5C.

S.10 Supplementary Experimental Figures

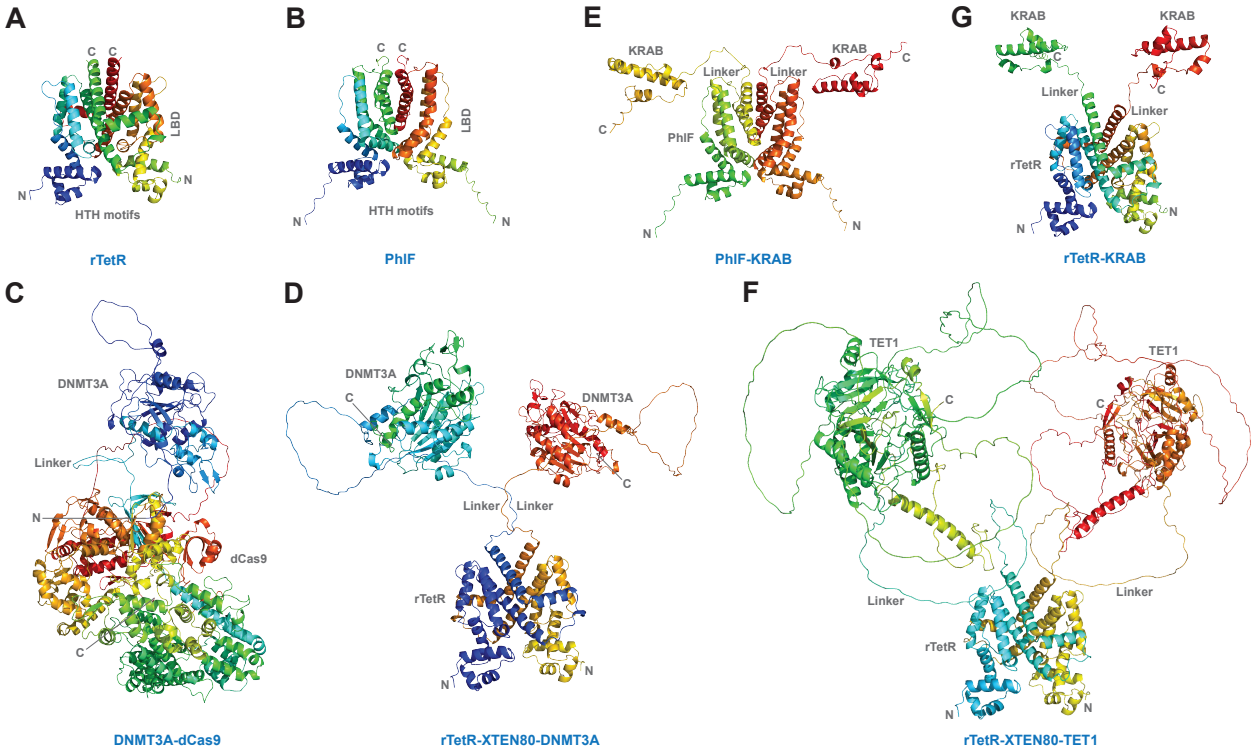

Fig. SE.1. Continued on the following page.

Fig. ES.1. Protein structures of epigenetic regulators used in the genetic reporter system. **A** Homodimer structure of DNA-binding protein rTetR. **B** Homodimer structure DNA-binding protein PhlF. **C** DNMT3A, writer of DNA methylation, fused to programmable DNA-binding protein dCas9. **D** DNMT3A fused to DNA-binding protein rTetR. **E** KRAB, a regulator of H3K9me3, fused to DNA-binding protein PhlF. **F** TET1, an an eraser of DNA methylation, fused to rTetR. **G** KRAB fused to rTeR. Predictions performed using AlphaFold2 and PyMol (Methods). For rTetR and PhlF TetR-family proteins, the epigenetic effectors KRAB, DNMT3A, and TET1 are fused proximal to alpha helix 9 at the C-terminus using a flexible linker. Helix-turn-helix (HTH) motifs bind DNA. The ligand binding domain (LBD) binds dox in the case or rTetR and DAPG in the case of PhlF. For dCas9, DNMT3A is fused at the N terminus using a flexible linker.

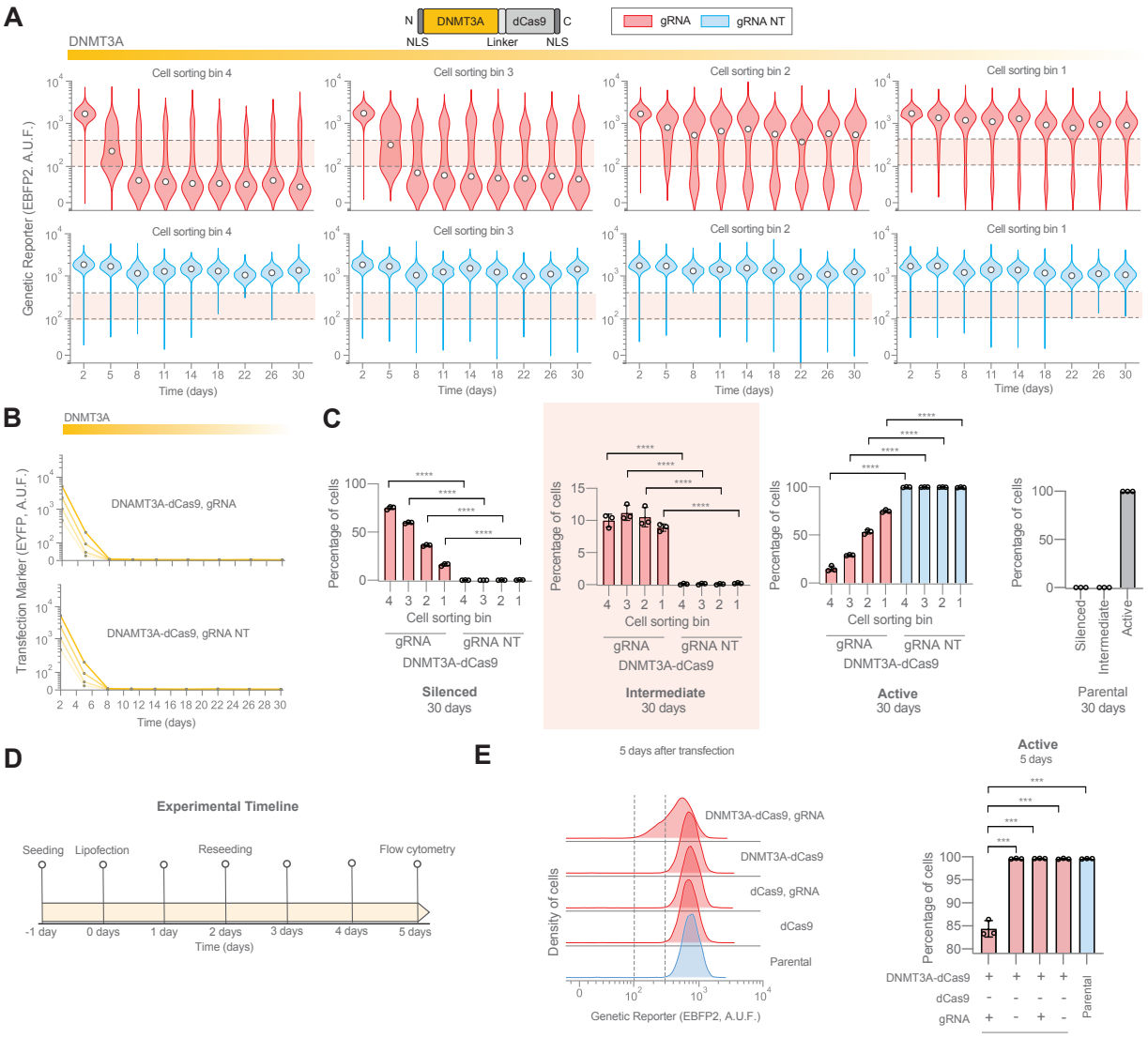

Fig. SE.2. Continued on the following page.

Fig. ES.2. Stationary distributions of DNMT3A-treated cells exhibit intermediate levels of gene expression. A Gene expression dynamics after epigenetic modulation using DNMT3A-dCas9 corresponding to the cells shown in Fig.2D, E. Highlighted region corresponds to intermediate levels of gene expression. Data shown are from a representative replicate from 3 independent replicates. **B** Transfection markers after epigenetic modulation using DNMT3A-dCas9 corresponding to the cells shown in Fig.2D, E and Panel A. Data shown are from a representative replicate from 3 independent replicates. **C** Percentage of cells 30 days after transfection of DNMT3A-dCas9 classified as shown in Panel A into silenced ($\leq$100 EBFP2 A.U.F.), intermediate (100.1$-$399.9 EBFP2 A.U.F.), and active ($\geq$400 EBFP2 A.U.F.) gene expression levels. Highlighted region corresponds to intermediate levels of expression. **D** Experimental overview of DNMT3A-dCas9 for various experimental conditions. **E** Experimental analysis of DNMT3A-dCas9 for various experimental conditions for repression of the genetic reporter. Cell densities are from a representative replicate from 3 independent replicates. Percentages and mean percentages are shown from three independent replicates. Error bars are s.d. of mean percentage.

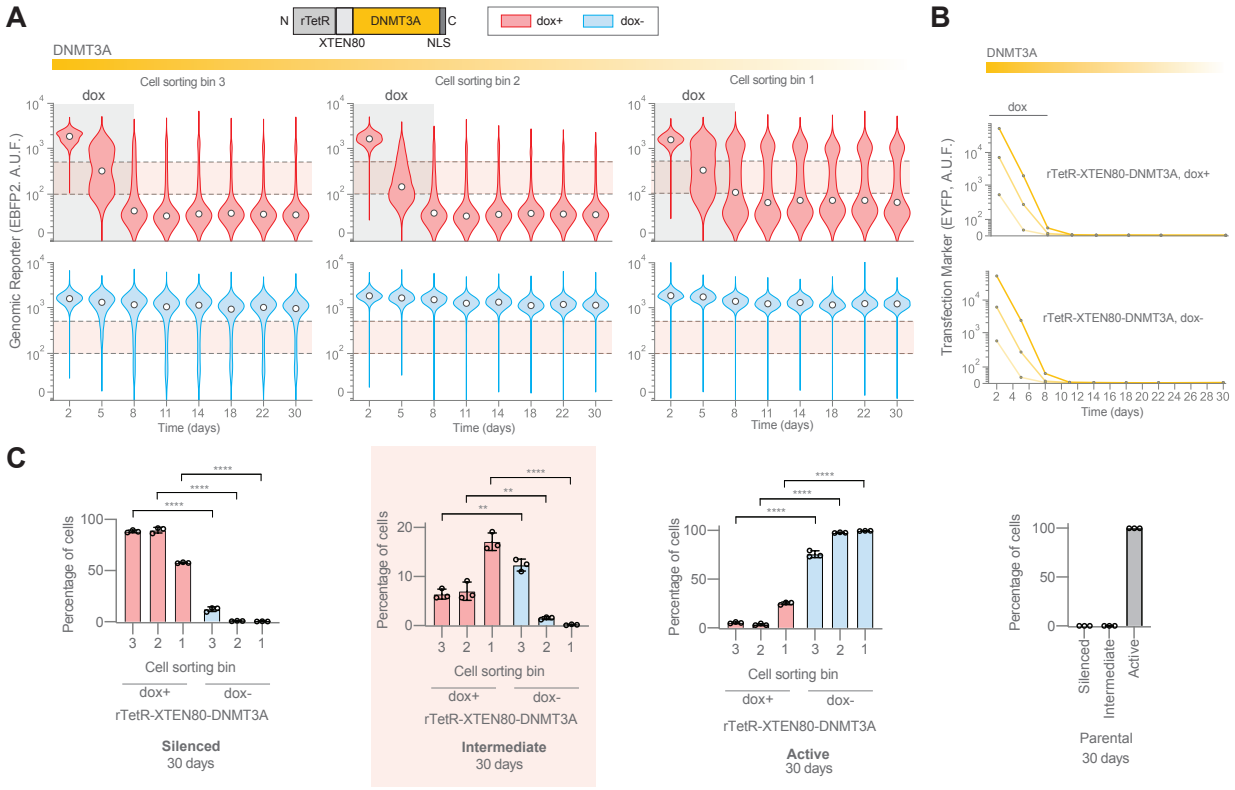

Fig. SE.3. Continued on the following page.

Fig. ES.3. Stationary distributions of cells silenced using rTetR-XTEN80-DNMT3A exhibit intermediate levels of gene expression. A Gene expression dynamics after DNMT3A-mediated silencing with rTetR-XTEN80-DNMT3A. Shown are flow cytometry measurements of the genetic reporter (EBFP2) for three different levels of transfection that were sorted using fluorescence-activated cell sorting. Dashed lines indicate the regions of silenced, intermediate, and active levels of gene expression. Data is from a representative replicate from 3 independent replicates. **B** Transfection markers after epigenetic modulation using DNMT3A-dCas9 corresponding to the cells shown in Panel A. Data shown are from a representative replicate from 3 independent replicates. **C** Percentage of cells as shown in to Panel classified into silenced ($\leq$100 EBFP2 A.U.F.), intermediate (100.1$-$499.9 EBFP2 A.U.F.), and active ($\geq$500 EBFP2 A.U.F.) gene expression levels. Shown is the mean percentage from three indepdent replicates. Error bars are the s.d. of the mean.

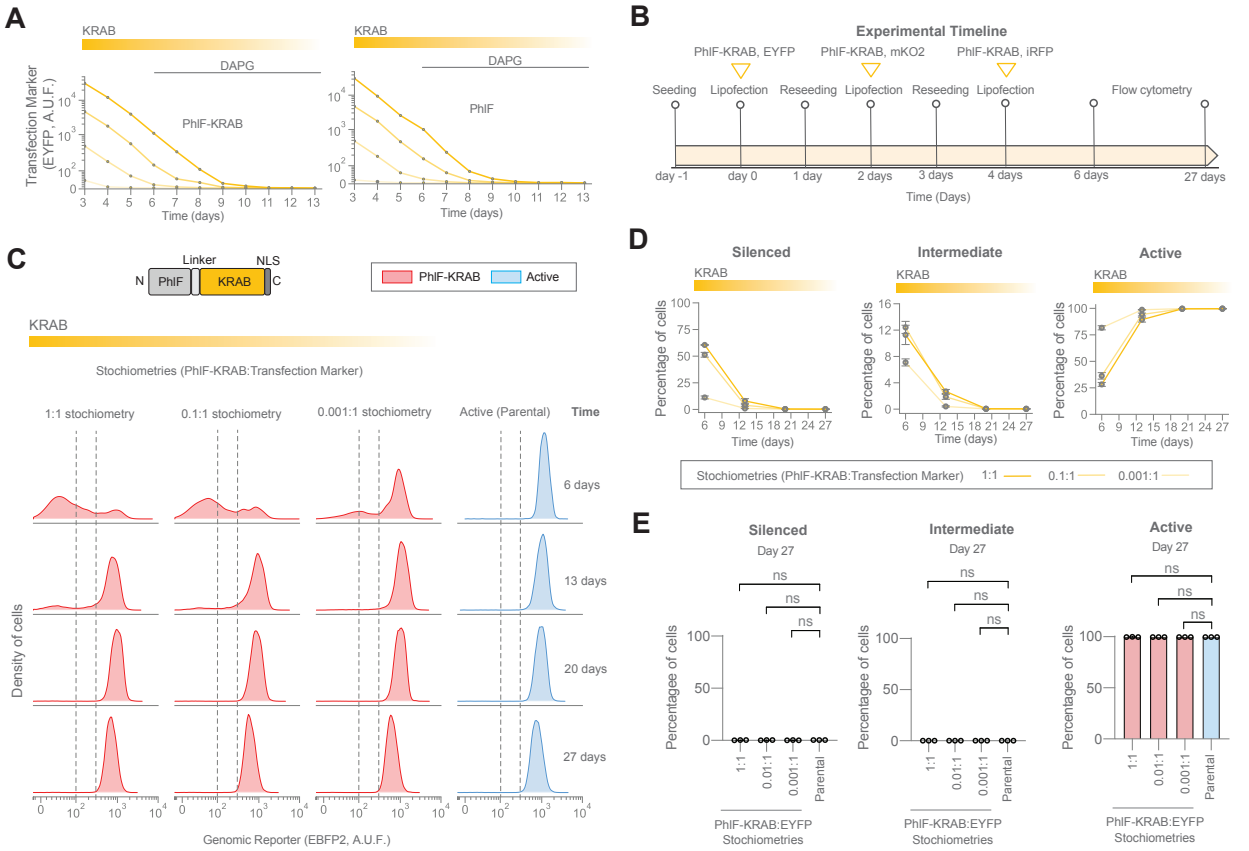

Fig. SE.4. Continued on the following page.

Fig. ES.4. KRAB-mediated silencing does to confer memory. **A** Transfection markers of epigenetic modulation using PhlF-KRAB corresponding to Fig. 2G. Data shown are from a representative replicate of three independent replicates. **B** Experimental overview of KRAB-mediated silencing using PhlF-KRAB. **C** Density of cells for KRAB-mediated silencing using PhlF-KRAB according to Panel B. Data shown is from a representative replicate from 3 independent replicates. **D** Percentage of cells shown in Panel C classified into silenced ($\leq$100 EBFP2 A.U.F.), intermediate (100.1$-$299.9 EBFP2 A.U.F.), and active ($\geq$300 EBFP2 A.U.F.) gene expression levels. Shown is the mean percentage from three independent replicates. Error bars are the s.d. of the mean. **E** Statistical analysis of percentages corresponding to Panel D, 27 days after initial transfection. Shown in the plots is the mean percentage from three independent replicates. Error bars are the s.d. of the mean.

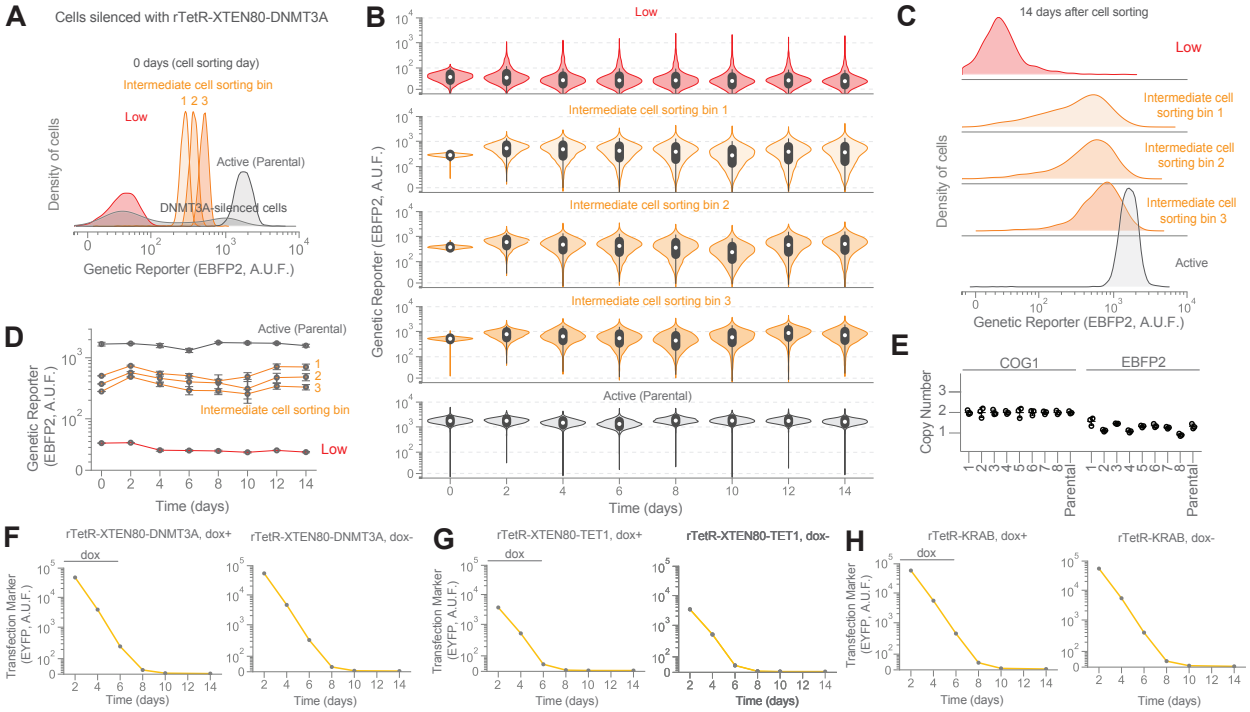

Fig. SE.5. Continued on the following page.

Fig. ES.5. Intermediate levels of gene expression are stable in cell silenced using rTetR instead of dCas9 for targeted recruitment of DNMT3A. A Density of cells from flow cytometry measurements on the day of fluorescence-activated cell sorting of cells exhibiting low, intermediate, and high levels of gene expression obtained from a DNMT3A-silenced cell population (rTetR-XTEN80-DNMT3A). Data shown is from a representative replicate from three independent replicates. **B** Time-course flow cytometry analysis of the dynamics of gene expression exhibited by cells obtained in panel A. Data is from one representative replicate from three independent replicates. **C** Density of cells from flow cytometry measurements obtained on the last time point in panel B (14 days after cell sorting). Data shown is from one representative replicate from three independent replicates. **D** Dynamics of gene expression exhibited by cells shown in panels A-C. Shown is the mean of geometric mean fluorescence from three independent replicates. Error bars are s.d. of the mean. **E** Digital PCR corresponding to the parental cell line and monoclonal populations corresponding to Fig. For each cell population, the average COG1 value was calculated (diploid). All data was then normalized to the COG1 average for each cell population separately. 4. **F** Transfection markers corresponding to Fig. 5 A. Data shown are from a representative replicate from 3 independent replicates. **G** Transfection markers corresponding to Fig. 5 B. Data shown are from a representative replicate from 3 independent replicates. **H** Transfection markers corresponding to Fig. 5 C. Data shown are from a representative replicate from 3 independent replicates.

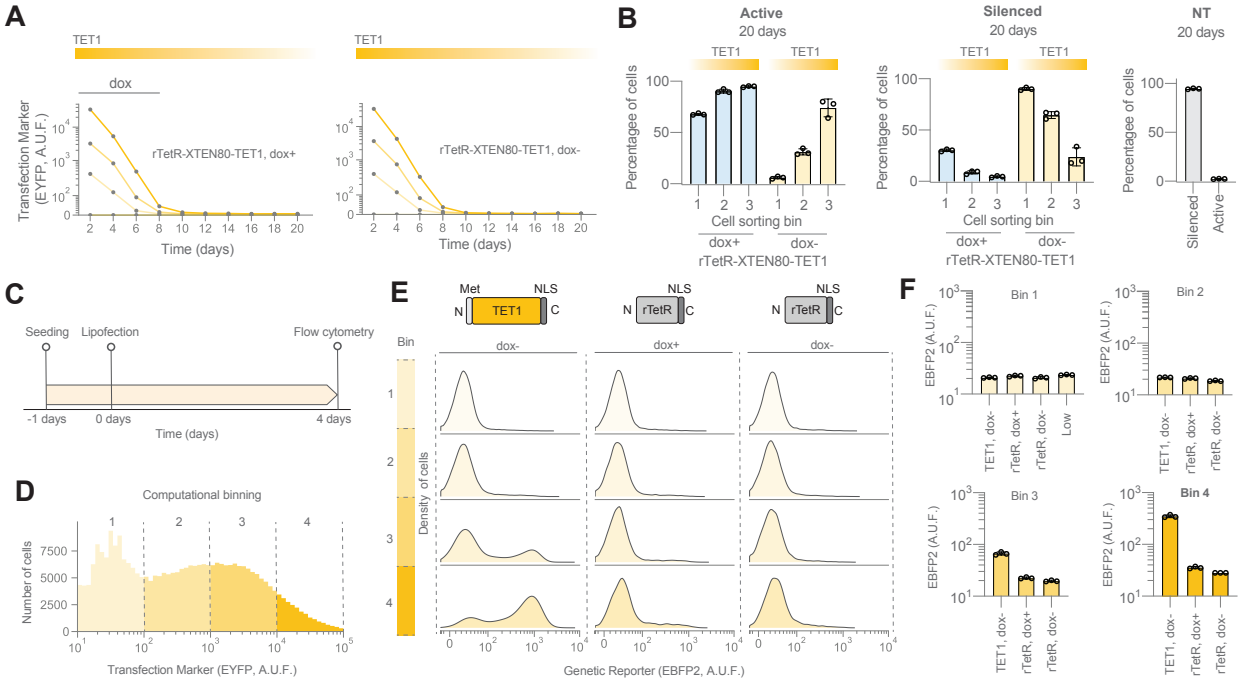

Fig. SE.6. Continued on the following page.

Fig. ES.6. TET1-mediated reactivation of cells completely silenced by DNMT3A. A Transfection markers corresponding to Fig.6A-C. Data shown are from a representative replicate from 3 independent replicates. **B** Percentages 20 days after TET1-mediated reactivation corresponding to Fig. 6 A-C. Data shown are from from 3 independent replicates. **C** Experimental overview of TET1-mediated reactivation from DNMT3A-silenced cells (DNMT3A-dCas9). **D** Computational binning performed according to the transfection marker corresponding to the experimental timeline in Panel C. **E** Cell densities for each transfection marker level as computed in Panel D for TET1 and rTetR. **F** Analysis of expression of the genetic reporter corresponding to the experimental results in Panels C-E. Shown is mean of geometric means of EBFP2 fluorescence from three independent replicates. Error bars are s.d. of the mean.

References

1. Graf, T. & Enver, T. Forcing cells to change lineages. *Nature* **462,** 587–94. https://doi.org/10.1038/nature08533 (2009).
2. Kouzarides, T. Chromatin modifications and their function. *Cell* **128,** 693–705. https://doi.org/10.1016/j.cell.2007.02.005 (2007).
3. Allis, C. D., Caparros, M.-L., Jenuwein, T. & Reinberg, D. *Epigenetics* (Cold Spring Harbor Laboratory Press, Second Edition, 2015).
4. Huang, S., Litt, M. & Blakey, C. A. *Epigenetic Gene Expression and Regulation* (Academic Press, 2015).
5. Heard, E. & Martienssen, R. A. Transgenerational epigenetic inheritance: myths and mechanisms. *Cell* **157,** 95–109. https://doi.org/10.1016/j.cell.2014.02.045 (2014).
6. Allis, C. D. & Jenuwein, T. The molecular hallmarks of epigenetic control. *Nat Rev Genet* **17,** 487–500. https://doi.org/10.1038/nrg.2016.59 (2016).
7. Li, E. & Zhang, Y. DNA methylation in mammals. *Cold Spring Harb Perspect Biol* **6.** https://doi.org/10.1101/cshperspect.a019133 (2014).
8. Cheng, X. Structural and functional coordination of DNA and histone methylation. *Cold Spring Harb Perspect Biol.* **6,** 693–705. https://doi.org/10.1101/cshperspect.a018747 (2014).
9. Bannister, A. J. *et al.* Selective recognition of methylated lysine 9 on histone H3 by the HP1 chromo domain. *Nature* **410,** 120–4. https://doi.org/10.1038/35065138 (2001).
10. Jones, P. L. *et al.* Methylated DNA and MeCP2 recruit histone deacetylase to repress transcription. *Nat Genet* **19,** 187–191. https://doi.org/10.1038/561 (1998).
11. Schneider, R. *et al.* Histone H3 lysine 4 methylation patterns in higher eukaryotic genes. *Nat Cell Biol* **6,** 73–7. https://doi.org/10.1038/ncb1076 (2003).
12. Hathaway, N. A. *et al.* Dynamics and memory of heterochromatin in living cells. *Cell* **149,** 1447–1460. https://doi.org/10.1016/j.cell.2012.03.052 (2012).
13. Zhang, T., Cooper, S. & Brockdorff, N. The interplay of histone modifications - writers that read. *EMBO Rep* **16,** 1467–1481. https://doi.org/10.15252/embr.201540945 (2015).
14. Ulm, E. A., Sleiman, S. F. & Chamberlin, H. M. Developmental functions for the Caenorhabditis elegans Sp protein SPTF-3. *Mech Dev* **128,** 428–41. https://doi.org/10.1016/j.mod.2011.08.003 (2011).

15. Dodd, I. B., Micheelsen, M. A., Sneppen, K. & Thon, G. Theoretical Analysis of Epigenetic Cell Memory by Nucleosome Modification. *Cell* **129,** 813–822. https://doi.org/10.1016/j.cell.2007.02.053 (2007).

16. Yamada, T., Fischle, W., Sugiyama, T., Allis, C. D. & Grewal, S. I. S. The nucleation and maintenance of heterochromatin by a histone deacetylase in fission yeast. *Mol Cell* **20,** 173–85. https://doi.org/10.1016/j.molcel.2005.10.002 (2005).

17. Grewal, S. I. & Klar, A. J. Chromosomal inheritance of epigenetic states in fission yeast during mitosis and meiosis. *Cell* **86,** 95–101. https://doi.org/10.1016/s0092-8674(00)80080-x (1996).

18. Stelzer, Y., Shivalila, C. S., Soldner, F., Markoulaki, S. & Jaenisch, R. Tracing dynamic changes of DNA methylation at single-cell resolution. *Cell* **163,** 218–29. https://doi.org/10.1016/j.cell.2015.08.046 (2015).

19. Mattei, A. L., Bailly, N. & Meissner, A. DNA methylation: a historical perspective. *Trends Genet* **38,** 676–707. https://doi.org/10.1016/j.tig.2022.03.010 (2022).

20. Hong, T. *et al.* TET2 modulates spatial relocalization of heterochromatin in aged hematopoietic stem and progenitor cells. *Nat Aging* **3,** 1387–1400. https://doi.org/10.1038/s43587-023-00505-y (2023).

21. Charlton, J. *et al.* TETs compete with DNMT3 activity in pluripotent cells at thousands of methylated somatic enhancers. *Nature genetics* **52,** 819–827. https://doi.org/10.1038/s41588-020-0639-9 (2020).

22. Du, J., Johnson, L. M., Jacobsen, S. E. & Patel, D. J. DNA methylation pathways and their crosstalk with histone methylation. *Nat Rev Mol Cell Biol* **16,** 519–32. https://doi.org/10.1038/nrm4043 (2015).

23. Ooi, S. K. *et al.* DNMT3L connects unmethylated lysine 4 of histone H3 to de novo methylation of DNA. *Nature* **448,** 714–717. https://doi.org/10.1038/nature05987 (2007).

24. Nan, X. *et al.* Transcriptional repression by the methyl-CpG-binding protein MeCP2 involves a histone deacetylase complex. *Nature* **393,** 383–389. https://doi.org/10.1038/30764 (1998).

25. Lopez-Serra, L. & Esteller, M. Proteins that bind methylated DNA and human cancer: reading the wrong words. *Br J Cancer* **98,** 1881–1885. https://doi.org/10.1038/sj.bjc.6604374 (2008).

26. Fuks, F. *et al.* The methyl-CpG-binding protein MeCP2 links DNA methylation to histone methylation. *J Biol Chem* **278,** 4035–4040. https://doi.org/10.1074/jbc.M210256200 (2003).

27. Bruno, S., Williams, R. J. & Del Vecchio, D. Epigenetic cell memory: The gene's inner chromatin modification circuit. *PLOS Computational Biology* **18,** 1–27. https://doi.org/10.1371/journal.pcbi.1009961 (2022).

28. Hay, A. D. *et al.* Epigenetic inheritance is unfaithful at intermediately methylated CpG sites. *Nat Commun* **14,** 5336. https://doi.org/10.1038/nrm4043 (2023).

29. Bird, A. P. & Taggart, M. H. Variable patterns of total DNA and rDNA methylation in animals. *Nucleic Acids Res* **8,** 1485–1497. https://doi.org/10.1093/nar/8.7.1485 (1980).

30. Hodges, E. *et al.* DNA methylation changes and complex intermediate states accompany lineage specificity in the adult hematopoietic compartment. *Molecular cell* **44,** 17–28. https://doi.org/10.1016/j.molcel.2011.08.026 (2011).

31. Stadler, M. B. *et al.* DNA-binding factors shape the mouse methylome at distal regulatory regions. *Nature* **480,** 490–495. https://doi.org/10.1038/nature10716 (2011).

32. Bintu, L. *et al.* Dynamics of epigenetic regulation at the single-cell level. *Science.* https://doi.org/10.1126/science.aab2956 (2016).

33. Ma, Y., Budde, M. W., Zhu, J. & Elowitz, M. B. Tuning methylation-dependent silencing dynamics by synthetic modulation of CpG density. *ACS Synthetic Biology* **12,** 2536–2545 (2023).

34. Lensch, S. *et al.* Dynamic spreading of chromatin-mediated gene silencing and reactivation between neighboring genes in single cells. *Elife* **11,** e75115 (2022).

35. Van, M. V., Fujimori, T. & Bintu, L. Nanobody-mediated control of gene expression and epigenetic memory. *Nature Communications* **12.1,** 537 (2021).

36. Liu, X. S. *et al.* Rescue of fragile X syndrome neurons by DNA methylation editing of the FMR1 gene. *Cell* **172,** 979–992 (2018).

37. Nuñez, J. K. *et al.* Genome-wide programmable transcriptional memory by CRISPR-based epigenome editing. *Cell* **184,** 2503–2519 (2021).

38. Angel, A., Song, J., Dean, C. & Howard, M. A Polycomb-based switch underlying quantitative epigenetic memory. *Nature* **476,** 105–108. https://doi.org/10.1038/nature10241 (2011).

39. Saxton, D. S. & Rine, J. Distinct silencer states generate epigenetic states of heterochromatin. *Mol Cell* **82,** 3566–3579. https://doi.org/10.1016/j.molcel.2022.08.002 (2022).

40. Yao, Z. *et al.* A taxonomy of transcriptomic cell types across the isocortex and hippocampal formation. *Cell* **184,** 3222–3241. https://doi.org/10.1016/j.cell.2021.04.021 (2021).

41. Liu, H. *et al.* DNA methylation atlas of the mouse brain at single-cell resolution. *Nature* **598,** 120–128. https://doi.org/10.1038/s41586-020-03182-8 (2021).

42. Gaidukov, L. *et al.* A multi-landing pad DNA integration platform for mammalian cell engineering. *Nucleic Acids Res.* **46,** 4072–4086 (May 2018).

43. Recillas-Targa, F. *et al.* Position-effect protection and enhancer blocking by the chicken beta-globin insulator are separable activities. *Proc. Natl. Acad. Sci. U. S. A.* **99,** 6883–6888 (May 2002).

44. Stanton, B. C. *et al.* Systematic transfer of prokaryotic sensors and circuits to mammalian cells. *ACS Synth. Biol.* **3,** 880–891 (Dec. 2014).

45. O'Geen, H. *et al.* dCas9-based epigenome editing suggests acquisition of histone methylation is not sufficient for target gene repression. *Nucleic Acids Res.* **45,** 9901–9916 (Sept. 2017).

46. Margolin, J. F. *et al.* Krüppel-associated boxes are potent transcriptional repression domains. *Proc. Natl. Acad. Sci.* **91,** 4509–4513. 10.1073/pnas.91.10.4509 (1994).

47. Schultz, D. C., Ayyanathan, K., Negorev, D., Maul, G. G. & Rauscher, F. J. SETDB1: a novel KAP-1-associated histone H3, lysine 9-specific methyltransferase that contributes to HP1-mediated silencing of euchromatic genes by KRAB zinc-finger proteins. *Annual Review of Physical Chemistry* **16,** 919–32. https://doi.org/10.1101/gad.973302 (2002).

48. Ecco, G., Imbeault, M. & Trono, D. KRAB zinc finger proteins. *Development* **144,** 2719–2729. https://doi.org/10.1242/dev.132605 (2017).

49. Hervouet, E., Peixoto, P., Delage-Mourroux, R., Boyer-Guittaut, M. & Cartron, P.-F. Specific or not specific recruitment of DNMTs for DNA methylation, an epigenetic dilemma. *Clin Epigenetics,* 17. https://doi.org/10.1186/s13148-018-0450-y (2018).

50. Trerotola, M., Relli, V., Simeone, P. & Alberti, S. Epigenetic inheritance and the missing heritability. *Hum Genomics* **9,** 17. https://doi.org/10.1186/s40246-015-0041-3 (2015).

51. Upadhyay, A. K., Horton, J. R., Zhang, X. & Cheng, X. Coordinated methyl-lysine erasure: structural and functional linkage of a Jumonji demethylase domain and a reader domain. *Curr Opin Struct Biol* **21,** 750–60. https://doi.org/10.1016/j.sbi.2011.08.003 (2011).

52. Rasmussen, K. D. & Helin, K. Role of TET enzymes in DNA methylation, development, and cancer. *Genes Dev.* **30,** 733–50. https://doi.org/10.1101/gad.276568.115 (2016).

53. Brown, D. A. *et al.* The SET1 Complex Selects Actively Transcribed Target Genes via Multivalent Interaction with CpG Island Chromatin. *Cell Rep* **20,** 2313–2327. https://doi.org/10.1016/j.celrep.2017.08.030 (2017).

54. Jackson, M. *et al.* Severe global DNA hypomethylation blocks differentiation and induces histone hyperacetylation in embryonic stem cells. *Mol Cell Biol* **24.** https://doi.org/10.1128/MCB.24.20.8862-8871 (2004).

55. Bannister, A. J. & Kouzarides, T. Regulation of chromatin by histone modifications. *Cell Res.* **21,** 381–395.

56. Gillespie, D. T. Stochastic Simulation of Chemical Kinetics. *Annual Review of Physical Chemistry* **58,** 35–55. https://doi.org/10.1146/annurev.physchem.58.032806.104637 (2007).

57. Ren, W. *et al.* Direct readout of heterochromatic H3K9me3 regulates DNMT1-mediated maintenance DNA methylation. *Proceedings of the National Academy of Sciences of the United States of America* **117,** 18439–18447. https://doi.org/10.1073/pnas.2009316117 (2020).

58. Laird, C. D. *et al.* Hairpin-bisulfite PCR: assessing epigenetic methylation patterns on complementary strands of individual DNA molecules. *Proceedings of the National Academy of Sciences of the United States of America* **101,** 204–209. https://doi.org/10.1073/pnas.2536758100 (2004).

59. Riggs, A. & Xiong, Z. Methylation and epigenetic fidelity. *Proceedings of the National Academy of Sciences of the United States of America* **101,** 4–5. https://doi.org/10.1073/pnas.2536758100 (2004).

60. Ito, S. *et al.* Tet proteins can convert 5-methylcytosine to 5-formylcytosine and 5-carboxylcytosine. *Science* **333,** 1300–3. https://doi.org/10.1126/science.1210597 (2011).

61. Liu, X. S. *et al.* Editing DNA methylation in the mammalian genome. *Cell* **167,** 233–247 (Sept. 2016).

62. Lim, Y. *et al.* A complex association between DNA methylation and gene expression in human placenta at first and third trimesters. *Nat Aging* **12,** e0181155. https://doi.org/10.1371/journal.pone.0181155 (2017).

63. Kulis, M. *et al.* Epigenomic analysis detects widespread gene-body DNA hypomethylation in chronic lymphocytic leukemia. *Nat Genet* **44,** 1236–42. https://doi.org/10.1038/ng.2443 (2012).

64. Sui, D. *et al.* Fine-tuning of iPSC derivation by an inducible reprogramming system at the protein level. *Stem Cell Reports* **2,** 721–33. https://doi.org/10.1016/j.stemcr.2014.03.013 (2014).

65. Clark, S. J. *et al.* scNMT-seq enables joint profiling of chromatin accessibility DNA methylation and transcription in single cells. *Nat Commun* **9,** 781. https://doi.org/10.1038/s41467-018-03149-4 (2018).

66. Argelaguet, R. *et al.* Multi-omics profiling of mouse gastrulation at single-cell resolution. *Nature* **576,** 487–491. https://doi.org/10.1038/s41586-019-1825-8 (2019).

67. Zeng, H. What is a cell type and how to define it? *Cell* **185,** 2739–2755. https://doi.org/10.1016/j.cell.2022.06.031 (2022).

68. Waddington, C. H. *The strategy of the genes* (Routledge, 1957).

69. Kalluri, R. & Weinberg, R. A. The basics of epithelial-mesenchymal transition. *J Clin Invest* **119,** 1420–8. https://doi.org/10.1172/JCI39104 (2009).

70. Chaffer, C. L., San Juan, B. P., Lim, E. & Weinberg, R. A. EMT, cell plasticity and metastasis. *Cancer Metastasis Rev* **35,** 645–654. https://doi.org/10.1007/s10555-016-9648-7 (2016).

71. Lin, Y.-T. & Wu, K.-J. Epigenetic regulation of epithelial-mesenchymal transition: focusing on hypoxia and TGF- signaling. *J Biomed Sci* **27,** 39. https://doi.org/10.1186/s12929-020-00632-3 (2020).

72. Matsumura, Y. *et al.* H3K4/H3K9me3 Bivalent Chromatin Domains Targeted by Lineage-Specific DNA Methylation Pauses Adipocyte Differentiation. *Mol Cell* **60,** 584–96. https://doi.org/10.1016/j.molcel.2015.10.025 (2015).

73. Jumper, J. *et al.* Highly accurate protein structure prediction with AlphaFold. *Nature* **596,** 583–589. ISSN: 1476-4687. https://doi.org/10.1038/s41586-021-03819-2 (Aug. 2021).

74. Mirdita, M. *et al.* ColabFold: making protein folding accessible to all. *Nature Methods* **19,** 679–682. ISSN: 1548-7105. https://doi.org/10.1038/s41592-022-01488-1 (June 2022).

75. Jin, C. *et al.* TET1 is a maintenance DNA demethylase that prevents methylation spreading in differentiated cells. *Nucleic Acids Research* **42,** 6956–71. https://doi.org/10.1093/nar/gku372 (2014).

76. Huisinga, K. L., Brower-Toland, B. & Elgin, S. C. The contradictory definitions of heterochromatin: transcription and silencing. *Chromosoma* **115,** 110–22. https://doi.org/10.1007/s00412-006-0052-x (2006).

77. Del Vecchio, D. & Murray, R. M. *Biomolecular Feedback Systems* (Princeton University Press, 2014).

78. Bruno, S., Williams, R. J. & Del Vecchio, D. *Model reduction and stochastic analysis of the histone modification circuit* in *2022 European Control Conference (ECC)* (2022), 264–271.

79. Felsenfeld, G. & Groudine, M. Controlling the double helix. *Nature* **421,** 448–53. https://doi.org/10.1038/nature01411 (2003).

80. Friedman, N., Cai, L. & Xie, X. S. Linking Stochastic Dynamics to Population Distribution: An Analytical Framework of Gene Expression. *Phys. Rev. Lett* **97.** https://doi.org/10.1103/PhysRevLett.97.168302 (2006).